Universidad de Santiago de Compostela
Departamento de Física Aplicada

Plasmonic response of graphene nanostructures

Memoria presentada por
Iván Silveiro Flores
para optar al grado de Doctor en Física

Director: Prof. F. Javier García de Abajo
Codirector: Dr. Sukosin Thongrattanasiri

Santiago de Compostela, diciembre de 2015

CSIC

ICFO
The Institute of Photonic Sciences

La presente memoria de tesis se realizó en el Nanophotonics Theory Group en:

- Instituto de Química-Física "Rocasolano" (CSIC), Serrano 119, 28006; Madrid, España (octubre, 2011 – septiembre, 2013).
- The Institute of Photonic Sciences (ICFO), Mediterranean Technology Park, Av. Carl Friedrich Gauss 3, 08860; Castelldefels (Barcelona), España (octubre, 2013 – diciembre, 2015).

Universidad de Santiago de Compostela
Departamento de Física Aplicada

D. **Francisco Javier García de Abajo**, Profesor de Investigación en el Institute of Photonic Sciences (ICFO), como director; y Dña. **María Teresa Flores Arias**, Profesora Titular de Universidad en el Dpto. de Física Aplicada de la Universidad de Santiago de Compostela, como tutora,

CERTIFICAN:

Que la memoria titulada "PLASMONIC RESPONSE OF GRAPHENE NANOSTRUCTURES" realizada por Iván Silveiro Flores en el Instituto de Química-Física "Rocasolano" del CSIC en Madrid y el Institute of Photonic Sciences (ICFO) en Castelldefels (Barcelona) para el departamento de Física Aplicada de esta Universidad, ha sido revisada y está en disposición de ser depositada como Tesis Doctoral para la obtección del grado de Doctor en Física.

Fdo.: F. Javier García de Abajo
Director

Fdo.: M. Teresa Flores Arias
Tutora

Fdo.: Iván Silveiro Flores
Doctorando

A mis padres y a mi hermano

If you want to find the secrets of the universe,
think in terms of energy, frequency, and vibration.
Nikola Tesla

Agradecimientos

Esta tesis, más allá de todos los resultados científicos, es el producto de una increíble experiencia vivida durante cuatro años. Desde el momento en que recibí la llamada de Javier, sabía que me embarcaba en una verdadera aventura que me haría madurar como científico y como persona, pero retrospectivamente, ha servido para que mi vida se cruzase con la de muchas personas extraordinarias.

Quiero agradecer en primer lugar la oportunidad única que me brindó Javier al unirme al Nanophotonics Theory Group y que ha permitido que disfrutase al máximo de la ciencia. Su entusiasmo por la investigación ha sido el mejor ejemplo que he podido tener para esforzarme cada día más e intentar convertirme en un mejor científico. No sería capaz de concebir esta tesis sin toda su ayuda y dedicación. Jamás podré agradecerle lo suficiente la confianza que me ha brindado todos estos años.

Secondly, I want to thank Suko for taking care of me during that tough first year of Ph.D. Despite his numerous own projects, he was always ready for sharing his knowledge and answering all the doubts of the rookie of the group.

Quisiera destacar también a Alejandro por todas esas largas discusiones científicas y sabios consejos que me ha dado, no solo durante esos dos primeros años de mi tesis en los que compartimos despacho en Madrid, sino también desde su marcha a EE. UU.

Por supuesto quiero agradecerle al resto del grupo en Madrid todo el cariño y apoyo que me mostraron desde el primer momento: Ana, mi paisano Xesús, Christin, Viktor y Johan. Además, gracias a Marien y Luis por esos divertidos ratos de asueto en el Rocasolano.

De los dos últimos años de mi tesis en ICFO, quiero destacar en primer lugar a José por todo su *scientific and technical support*. Una grandísima persona siempre dispuesta a ayudar al instante. I want to thank also Andrea for those good moments

learning from him during scientific collaborations, but also out of ICFO in Castelldefels. Gracias también al resto de miembros del grupo por su sincera amistad: Joel, Juanma, Sandra, Renwen y Jacob.

Thanks also to all the people outside the group I had the pleasure to collaborate with, and from whom I learned a lot: Marco, Andreas, Francisco, Claude, Stéphane-Olivier...

Aparte del entorno científico, quiero agradecerles a mis viejos colegas del instituto en Santiago el hacerme ver que mi regreso a casa era un motivo de celebración y reencuentro para todos ellos. También gracias a mi compañero de fatigas Brais, un gran amigo con el que siempre he podido contar, y a Eduardo, porque su amistad no entiende de océanos de distancia.

Gracias a Marta por ese año y medio increíble a su lado en Castelldefels, y a Mireia, porque aun sabiendo que me iba, quiso disfrutar al máximo estos últimos meses conmigo.

Me gustaría agradecerle también a toda mi familia de Santiago, Taboada y Padrón que, a pesar de estar muy lejos, siempre me hicieron sentir que los tenía a mi lado. Gracias a Elena por haber cuidado de mí todos estos años, y mi padre y a mi hermano, porque son lo más importante para mí. Por último, quiero darle las gracias a mi mamá por su ejemplo de esfuerzo y sacrificio por seguir adelante cada día siempre con una sonrisa. Sé que estaría muy orgullosa de todo esto.

Contents

List of Figures **xvii**

List of Tables **xix**

List of Acronyms **xxi**

Resumen **1**

Abstract **9**

1 Introduction **15**

1.1 History of graphene and other carbon allotropes 15
1.2 Synthesis of graphene 17
1.3 Optoelectronic properties 17
1.3.1 sp^2 hybridization 17
1.3.2 Graphene band structure 18
1.3.3 Density of states 23
1.3.4 High electrical mobility 24
1.4 Electromagnetic modeling of graphene 24
1.4.1 Classical description 25
1.4.2 Quantum-mechanical description: Random-phase approximation 30
1.5 Plasmons in graphene 31
1.5.1 σ and π plasmons 32
1.5.2 Dirac plasmons 32
1.5.3 Optical losses 42

1.5.4 Electrostatic scaling law 42

2 Plasmons in multiple doping configurations 47

2.1 Plasmons in interacting uniformly doped ribbons 48

2.2 Plasmons in inhomogeneously doped nanoribbons 56

2.2.1 Backgated nanoribbons 56

2.2.2 Co-planar nanoribbon pairs at opposite potentials 60

2.2.3 Individual nanoribbons under a uniform electric field 62

2.3 Plasmons in inhomogeneously doped nanodisks 65

2.3.1 Disks under uniform potential doping 65

2.3.2 Disks doped by an external point charge 70

2.4 Plasmons in periodically doped graphene 72

2.4.1 Periodic doping by point charges 74

2.4.2 Local density of optical states 78

2.5 Conclusions 81

3 Quantum nonlocal effects in nanoribbons 83

3.1 Individual nanoribbons 84

3.2 Dimers of co-planar nanoribbons 86

3.3 Arrays of co-planar nanoribbons 88

3.4 Conclusions 90

4 Nonlinear optical effects 91

4.1 Description of nonlinear optical effects 92

4.1.1 Second-harmonic generation 93

4.1.2 Third-harmonic generation and Kerr effect 94

4.2 Classical nonlinear optical conductivities 95

4.3 Classical nonlinear optical polarizabilities 97

4.4 Comparison classical-quantum nonlinear effects 99

4.5 Conclusions 102

5 Molecular sensing with graphene 103

5.1 SEIRA 104

5.2 SERS 110
5.3 Conclusions 112

6 Conclusions **115**

A Effect of the dielectric environment on graphene **117**

B LSP resonance frequency in electrostatics **121**

C Infrared absorption and Raman scattering **123**

List of publications and contributions to conferences **127**

Bibliography **131**

List of Figures

1.1 Carbon allotropes 16
1.2 Graphene lattice 19
1.3 Graphene band diagram 21
1.4 Density of states in graphene 23
1.5 Conductivity and dielectric function of graphene 28
1.6 Types of plasmons excited in graphene 33
1.7 Reflection and transmission of graphene 35
1.8 Dispersion relation of graphene 37
1.9 Localized surface plasmons (LSPs) in a graphene nanodisk 41

2.1 Plasmon wave function of graphene nanoribbons 49
2.2 LSPs in interacting pairs of graphene nanoribbons 52
2.3 LSP energy in dimers and arrays of graphene nanoribbons 53
2.4 Absorbance of a bilayer array of graphene nanoribbons 54
2.5 LSPs in backgated graphene nanoribbons 59
2.6 LSPs in pairs of co-planar parallel graphene nanoribbons of opposite polarity 61
2.7 LSPs in individual graphene nanoribbons subject to a uniform external electric field 63
2.8 Induced charge density of a graphene nanodisk under uniform doping and inhomogeneous doping by a uniform potential 69
2.9 LSPs in a neutral graphene nanodisk exposed to a neighboring external point charge 70

2.10 Graphene-disk plasmon frequencies for three different doping configurations . . . 71
2.11 Optical dispersion of periodically doped graphene . . . 73
2.12 Plasmonic bands in periodically doped graphene by point charges . . 77
2.13 Local density of optical states in periodically doped graphene by point charges . . . 80

3.1 Quantum LSPs in individual graphene nanoribbons . . . 85
3.2 Quantum LSPs in interacting co-planar graphene nanoribbon dimers 86
3.3 Evolution of the LSP energy with the separation distance in co-planar armchair-edged dimers of graphene nanoribbons . . . 87
3.4 Absorbance of a co-planar array of graphene nanoribbons with zigzag and armchair edges . . . 89

4.1 Second- and third-harmonic generation in graphene . . . 93
4.2 Linear and nonlinear plasmonic response of equilateral graphene nanotriangles . . . 101

5.1 Surface-enhanced infrared absorption (SEIRA) spectroscopy with graphene plasmons. . . . 105
5.2 Doping dependence in the absorption cross-section of molecules in SEIRA spectroscopy . . . 107
5.3 Molecular sensitivity of the doping-dependent frequency-integrated absorption in SEIRA spectroscopy . . . 109
5.4 Surface-enhanced Raman scattering (SERS) with graphene plasmons. 111

A.1 Electrostatic potential over extended graphene by an external point charge . . . 119

C.1 Energy-level diagram of infrared absorption, Rayleigh scattering, and Raman scattering . . . 125

List of Tables

1.1 Analytical approximations for the parameters ξ_j and η_j of the electrostatic scaling law 46

4.1 Polarizability unit conversion factors 92

List of Acronyms

AC Armchair

ac Alternating current

ATR Attenuated total reflection

BEM Boundary-element method

BTE Boltzmann transport equation

BZ Brillouin zone

C-C Carbon-to-carbon

CNT Carbon nanotube

CVD Chemical vapor deposition

dc Direct current

DSDA Discrete surface-dipole approximation

EELS Electron energy-loss spectroscopy

e-h Electron-hole

FWHM Full width at half maximum

H-H Hydrogen-to-hydrogen

LDOS Local density of optical states

LSP Localized surface plasmon

NIR Near infrared

PWF Plasmon wave function

RPA Random-phase approximation

SEIRA Surface-enhanced infrared absorption

SERS Surface-enhanced Raman scattering

SHG Second-harmonic generation

SM Supplementary material

SPP Surface plasmon polariton

STM Scanning tunneling microscope

TE Transverse electric

THG Third-harmonic generation

TM Transverse magnetic

UV Ultraviolet

ZZ Zigzag

Resumen

El grafeno, considerado por muchos como el material del futuro, se define como una lámina plana constituida por átomos de carbono fuertemente entrelazados en una red bidimensional con forma de panal de abeja. Desde que en 2004 los físicos rusos K. Novoselov y A. Geim de la Universidad de Manchester (ambos galardonados con el Premio Nobel de Física en 2010) sintetizaran por primera vez láminas aisladas de grafeno mediante exfoliación mecánica, este revolucionario material ha despertado un gran interés debido a sus extraordinarias propiedades optoelectrónicas muy útiles para la nanofotónica (rama de la física que estudia la interacción de la luz con la materia en el rango del nanómetro, esto es, en distancias mil millones de veces más pequeñas que el metro). La naturaleza 2D de este alótropo de carbono en combinación con su singular estructura atómica, dan lugar a una poco corriente relación de dispersión lineal muy diferente a la típica parabólica de los metales nobles.

Al producirse la interacción entre la luz y la materia (cuya longitud característica D ha de ser necesariamente más pequeña o del orden de la longitud de onda de la propia luz incidente, *i.e.*, $D \lesssim \lambda$), se genera una serie de interesantes fenómenos electromagnéticos entre los cuales se halla la excitación del objeto de estudio de esta tesis: el plasmón (*i.e.*, la oscilación colectiva de los electrones en metales nobles o grafeno). Debido al intenso confinamiento de estas oscilaciones eléctricas (en distancias por debajo del límite de difracción de la luz), los plasmones estimulan una fuerte interacción luz-materia e incrementan notablemente el campo eléctrico inducido. Es necesario destacar también que los plasmones son muy sensibles a la forma y tamaño de las nanoestructuras que los sustentan, al entorno dieléctrico y a la cantidad de electrones participando en la oscilación colectiva (relacionados éstos a su vez con la estructura de bandas electrónicas del material que los contiene). Un estricto control

de estos parámetros es indispensable para poder conocer en profundidad la respuesta de cualquier nanoestructura capaz de sustentar plasmones.

Centrémonos ahora en el elemento químico que conforma la estructura de grafeno: el carbono. Su isótopo más común, el $^{12}_{6}$C, posee 6 protones y 6 neutrones en el núcleo atómico, y 6 electrones moviéndose libremente alrededor de éste distribuidos en diferentes orbitales electrónicos. La configuración electrónica del átomo de carbono en el estado fundamental es $1s^2 2s^2 2p^2$, con dos electrones llenando por completo el orbital 1s, otros dos llenando el orbital 2s, y los dos electrones restantes ocupando distintos orbitales 2p. Sin embargo, cuando varios átomos de carbono están próximos entre sí, la interacción entre orbitales hace que sea más favorable energéticamente que un electrón del orbital 2s se excite hasta el orbital 2p desocupado, formándose de esta manera enlaces covalentes entre diferentes átomos vecinos. Por lo tanto, pasamos a tener cuatro estados cuánticos idénticos que pueden combinarse entre sí formando diferentes orbitales híbridos sp^i (con $i = 1, 2$ o 3).

La red atómica con forma de panal de abeja del grafeno es el resultado de la hibridación sp^2 entre un orbital s y dos orbitales p por cada átomo de carbono, a partir de la cual se forman enlaces covalentes σ con un ángulo característico de 120° entre átomos vecinos. Este enlace fuerte es el responsable de la extrema dureza de la red bidimensional de átomos de carbono, los cuales permanecen separados una distancia $a_0 = 1.421\,\text{Å}$. El orbital p (o también denominado π) que queda libre se orienta perpendicularmente a la lámina de átomos y puede formar un enlace débil con los orbitales de los carbonos de otras láminas mediante interacción de van der Waals. La singular estructura de bandas electrónicas del grafeno está producida por estos orbitales π y consta de dos bandas: una inferior, o también llamada banda de valencia, y una superior o de conducción. A bajas energías sus formas se asemejan a las de dos conos invertidos tocándose en un único punto. A este punto se le denomina comúnmente punto de Dirac (su posición exacta en el espacio de momentos se halla en el vértice del hexágono que conforma la primera zona de Brillouin del grafeno) y su importancia reside en que determina el nivel de Fermi del grafeno en estado neutro (también denominado grafeno pristino o grafeno sin dopar). En este estado de neutralidad, la banda de valencia está completamente llena con electrones π deslocalizados, mientras que la de conducción permanece vacía. En consecuencia, podemos tratar al grafeno en estado neutro como un semiconductor con una banda

prohibida de valor nulo, de manera que únicamente son posibles transiciones inter-banda de pares electrón-hueco.

La oscilación colectiva de los electrones deslocalizados π en grafeno da lugar a los llamados plasmones intrínsecos π cuyas energías oscilan entre los 4.5 y 7 eV, lo que los sitúa en la región ultravioleta del espectro electromagnético. Además, estos plasmones son muy poco ajustables lo que limita su relevancia en nanofotónica. Sin embargo, cuando agregamos electrones adicionales al grafeno, éstos comienzan a llenar estados desocupados en la banda de conducción hasta un cierto nivel que determina el nuevo valor del nivel de Fermi $E_{\mathrm{F}} = \hbar v_{\mathrm{F}} \sqrt{\pi n}$, donde n es la densidad por unidad de área de estos electrones adicionales y $v_{\mathrm{F}} \approx c/300$ su velocidad de desplazamiento (nótese que debido a la relación de dispersión lineal, los electrones adicionales son tratados como partículas sin masa). De este modo, una banda prohibida de anchura $2E_{\mathrm{F}}$ se abre y, además de las ya mencionadas transiciones inter-banda, ahora también son posibles transiciones intra-banda de pares electrón-hueco. El proceso de agregar nuevos electrones se conoce como dopado (más concretamente, este caso se denomina dopado tipo n) y, debido a la simetría de bandas, se produce el mismo efecto cuando electrones π son extraídos de la banda de valencia (*i.e.*, dopado tipo p, o mediante huecos en vez de electrones). El hecho de que el nivel de Fermi E_{F} (también llamado nivel de dopado) sea ajustable con n así como la peculiar relación de dispersión lineal, son propiedades únicas del grafeno que lo distinguen notablemente de los metales nobles estudiados habitualmente en nanofotónica. A diferencia del grafeno, n en los metales nobles apenas es ajustable y, además, cambios ostensibles en n apenas afectan de manera significativa a las propiedades optoelectrónicas del metal.

A las oscilaciones colectivas de los electrones adicionales en grafeno dopado se las conoce como plasmones extrínsecos o plasmones de Dirac. Sus frecuencias de resonancia abarcan desde los THz hasta el infrarrojo cercano y habitualmente se suelen dividir en dos subgrupos distintos dependiendo de sus propiedades de propagación: los *polaritones del plasmón de superficie* (SPPs, por su acrónimo en inglés) y los *plasmones de superficie localizados* (LSPs). Los primeros son modos electromagnéticos que se propagan en láminas de grafeno extendido situadas en la interfaz de separación entre dos medios dieléctricos. Paradójicamente, estos plasmones no pueden ser excitados directamente con luz externa debido a los diferentes vecto-

res de onda de la luz y del propio plasmón. En la actualidad se emplean distintas estrategias para evitar este problema: las configuraciones Otto y Kretschmann, la reflexión interna total, el dopado periódico, etc. Por otro lado, los LSPs son modos electromagnéticos confinados en nanoestructuras finitas que sí pueden ser eficientemente excitados con luz externa. Ambos subgrupos de plasmones presentan en grafeno unas propiedades interesantes si se comparan con sus homónimos en metales nobles (*e.g.*, poseen mayores tiempos de vida medios τ así como factores de calidad Q superiores, son también más propensos a sufrir efectos ópticos no lineales y permiten incrementar el campo eléctrico inducido en varios órdenes de magnitud). Asimismo, los SPPs en grafeno presentan una longitud de onda mucho más corta que λ, lo que se traduce en un mayor grado de confinamiento del campo eléctrico. El control de las anteriores propiedades ha estimulado el desarrollo de nuevos modelos teóricos capaces de predecir la respuesta plasmónica del grafeno y, por tanto, fomentar su aplicación en dispositivos para óptica no lineal, detección y modulación de luz, procesado de señales, etc.

La dispersión óptica de los plasmones de Dirac en grafeno está determinada por la dinámica de los electrones adicionales ocupando la banda de conducción. El modelo más simple capaz de proporcionar una descripción razonable es el modelo de Drude, en el cual únicamente se asumen transiciones intra-banda a temperatura nula y un posterior decaimiento de los electrones a través de múltiples canales: colisión con fonones, con defectos de red o, en menor medida, con otros electrones. A pesar de su aparente simplicidad, este modelo se puede considerar una buena aproximación cuando las energías de los fotones incidentes son bastante inferiores al nivel de dopado. Si esta condición no se cumple, un modelo más elaborado y realista conocido como la *aproximación de fase aleatoria* (RPA) nos permite incluir las transiciones inter-banda y los efectos de temperaturas finitas. En el primer capítulo de esta tesis comparamos al detalle ambos modelos para múltiples niveles de dopado.

Para describir teóricamente el comportamiento de los campos electromagnéticos asociados al grafeno en el límite clásico, es necesario hallar la solución de las ecuaciones macroscópicas de Maxwell, incluyendo el efecto del retardo temporal en la propagación de la luz. A lo largo de esta tesis, obtendremos la solución exacta de las ecuaciones de Maxwell a través del *método de elementos de frontera* (BEM). En BEM, un sistema de ecuaciones (equivalente a las ecuaciones macroscópicas de

Maxwell) que contiene integrales de superficie se evalúa en las fronteras de una determinada nanoestructura de grafeno. En cuanto a las características electromagnéticas de esta nanoestructura, asumimos las siguientes condiciones: es no magnética, local (*i.e.*, no depende de la componente paralela del vector de onda $k_{\|}$ de la luz incidente) y lineal (*i.e.*, la relación entre la polarización de la nanoestructura y el campo eléctrico externo asociado al haz incidente es lineal). Una vez determinadas las condiciones de frontera, obtenemos la solución numérica rigurosa del sistema de ecuaciones mediante una *discretización* finita en las fronteras de la muestra de grafeno con forma arbitraria. A pesar de la versatilidad de este método, hallar una solución veraz puede consumir mucho tiempo de cálculo. Sin embargo, tal y como mostramos en el primer capítulo de esta tesis, para nanoestructuras suficientemente pequeñas (*i.e.*, $D \ll \lambda$), podemos trabajar con seguridad en el límite electrostático (*i.e.*, límite sin retardo temporal en donde asumimos $c \to \infty$). En este contexto electrostático, la interacción entre la luz y el grafeno se considera instantánea y nuestro problema se reduce a encontrar la solución de la ecuación de Poisson con las condiciones de frontera apropiadas. Como también exponemos en este primer capítulo, la respuesta plasmónica del grafeno concuerda excelentemente con la solución numérica completa de las ecuaciones de Maxwell incluyendo el retardo temporal. Finalmente, en la última sección de este primer capítulo, derivamos analíticamente una *ley de escala electrostática* muy útil que nos permite obtener las frecuencias de resonancia de los LSPs para cualquier forma arbitraria, tamaño, entorno dieléctrico o nivel de dopado de la nanoestructura de grafeno. En concreto, mostramos que las frecuencias de resonancia de los LSPs evolucionan aproximadamente siguiendo la condición $\omega_{\mathrm{p}} \propto \sqrt{E_{\mathrm{F}}/D}$, la cual ilustra lo altamente ajustables que son.

El proceso de dopado experimental de grafeno generalmente se realiza a través de métodos químicos o mediante la aplicación de un potencial electrostático. En este último caso, se aplica una diferencia de potencial eléctrico sobre el grafeno con respecto a tierra, generándose un campo eléctrico uniforme $\mathbf{E}_0$ en dirección perpendicular sobre uno de los lados de la nanoestructura de grafeno. De este modo se induce una densidad de electrones adicionales $n = -E_0/4\pi e$ que se distribuye uniformemente sobre el grafeno con el fin de apantallar por completo el campo eléctrico externo. Es muy común encontrar en la literatura estudios sobre LSPs en grafeno asumiendo esta distribución uniforme de n. Sin embargo, en experimentos reales se

observa que n presenta una distribución espacial no homogénea, con un perfil que depende de la configuración geométrica específica y que, por tanto, afecta a la respuesta plasmónica del grafeno. En el segundo capítulo de esta tesis analizamos este comportamiento no homogéneo estudiando en el límite clásico diferentes configuraciones realistas de dopado en nanocintas (*nanoribbons*), nanodiscos y en láminas de grafeno extendido. En particular, para las nanocintas estudiamos tres tipos distintos de dopado: (i) nanocintas individuales a las que aplicamos un determinado potencial eléctrico, (ii) pares de nanocintas coplanarias con potenciales de signo opuesto y (iii) nanocintas individuales bajo el efecto de un campo eléctrico uniforme paralelo a su superficie. Para los nanodiscos estudiamos un dopado mediante (i) un determinado potencial eléctrico y (ii) mediante una carga puntual situada en el eje de simetría del disco y próxima a su superficie. Finalmente, para la lámina de grafeno extendido estudiamos un dopado periódico con (i) cargas puntuales de igual signo y (ii) cargas de signo alterno, en los cuales se generan distintas bandas plasmónicas de los SPPs. Como resultado global, hallamos que los plasmones de Dirac son altamente sensibles a las distribuciones no homogéneas de dopado y que, por tanto, una respuesta plasmónica particular ha de ser considerada para el correcto diseño de dispositivos ópticos que contengan grafeno.

En el caso de que la longitud característica de una nanoestructura de grafeno sea del orden de la longitud de onda de Fermi (*i.e.*, la longitud de onda de de Broglie cerca del nivel de Fermi, que en el grafeno resulta ser $\lambda_{\mathrm{F}} = \sqrt{4\pi/n} = hv_{\mathrm{F}}/E_{\mathrm{F}} \approx 10.33\,\mathrm{nm}$ cuando $E_{\mathrm{F}} = 0.4\,\mathrm{eV}$; nótese que la dependencia con n en grafeno contrasta con el valor casi constante en los metales nobles: $\lambda_{\mathrm{F}} \approx 0.52\,\mathrm{nm}$ en el caso del oro), el electromagnetismo clásico pierde su validez y es necesario un modelo mecanocuántico para poder describir la respuesta plasmónica del grafeno. En el tercer capítulo de esta tesis presentamos extensos cálculos cuánticos obtenidos mediante un *modelo de enlace fuerte* (TB) para la respuesta eléctrica, combinado con la RPA para la respuesta óptica (nótese que con el modelo de TB se incluyen también efectos no locales y de borde, en donde distinguimos dos tipos de terminaciones en la muestra de grafeno: borde tipo *brazo de silla* y borde tipo *zigzag*). En particular, observamos que para nanocintas estrechas de grafeno dopado ($D = 6\,\mathrm{nm}$), tanto en muestras individuales como en grupo produciendo interacciones electromagnéticas entre ellas, los cálculos clásicos no tienen en cuenta múltiples efectos físicos

que afectan notablemente a la respuesta plasmónica del grafeno y que, por contra, sí observamos usando el modelo mecano-cuántico. Por ejemplo, en nanocintas individuales, cuando el nivel de dopado es inferior a las frecuencias de resonancia de los LSPs (en este capítulo consideramos los modos dipolares de orden más bajo), éstos se ven fuertemente afectados por los bordes tipo *zigzag* y decaen a través de la excitación de estados de borde con energía nula. Además, en el caso del borde tipo *brazo de silla*, los LSPs también experimentan efectos no locales (aunque en menor medida), dando lugar a corrimientos al azul y a ensanchamientos de los modos. Mostramos también en este tercer capítulo que los efectos no locales juegan un papel importante en la interacción de grupos de nanocintas a distancias cortas, dando lugar a correcciones notables en las frecuencias de resonancia de los LSPs. De hecho, basándonos en estos resultados, podemos afirmar que el grafeno es un material muy apropiado para estudiar los efectos cuánticos y no locales sobre los LSPs.

El cuarto capítulo de esta tesis está dedicado al estudio de las intensas no linealidades observables en la respuesta plasmónica del grafeno dopado. En primer lugar realizamos un minucioso informe de tres de los procesos no lineales más importantes: generación del segundo armónico, generación del tercer armónico y efecto Kerr. Posteriormente, a partir de la *ecuación de transporte de Boltzmann* (BTE), en la cual únicamente se consideran transiciones intra-banda de pares electrón-hueco a $T = 0$, conseguimos extender el formalismo de la *ley de escala electrostática* a órdenes no lineales en las expresiones de la conductividad y polarizabilidad eléctricas del grafeno. Finalmente, comparamos en detalle la respuesta plasmónica (no lineal) clásica y cuántica (obtenida esta última a través de un modelo de TB similar al descrito en el tercer capítulo, el cual tiene en cuenta también las transiciones inter-banda y los efectos de temperaturas finitas) para pequeños nanotriángulos equiláteros de grafeno. Los resultados que presentamos muestran que la respuesta clásica subestima notablemente las no linealidades excepto para bajos niveles de dopado, lo que revela la importancia crucial de tener un conocimiento pormenorizado de los efectos no lineales.

Por último, en el quinto capítulo mostramos el extraordinario potencial de los LSPs en grafeno para poder identificar la estructura química de las moléculas. En la actualidad, los procesos de identificación de moléculas generalmente requieren

el uso de técnicas de detección bastante ineficientes, además de espectrómetros y haces de luz láser muy costosos. Con el fin de evitar estos inconvenientes, en esta tesis presentamos un nuevo mecanismo de detección que únicamente requiere el uso de lámparas emitiendo en el rango del infrarrojo y nanodiscos de grafeno dopado. Comprobamos semianalíticamente que los LSPs sustentados en los nanodiscos contribuyen notablemente a la capacidad de la molécula de absorber o esparcir (*scatter*) inelásticamente los fotones del haz de luz incidente, cambiando al final del proceso la energía roto-vibracional de la molécula. Estos procesos de absorción y esparcimiento son los principios elementales de ciertas técnicas de espectroscopía muy comunes: *intensificación de la absorción infrarroja en superficies* (SEIRA) e *intensificación de dispersión Raman en superficies* (SERS). En nuestro caso, hallamos incrementos de $\sim 10^3$ y $\sim 10^4$, respectivamente. Como resultado fundamental de este quinto capítulo destacamos que, mediante la integración de la señal de detección a lo largo de un amplio rango de frecuencias en función del nivel de dopado E_{F}, nos es posible identificar la naturaleza química de la molécula con una resolución en energía dada por la anchura espectral de los LSPs sustentados en los nanodiscos de grafeno.

Como corolario, consideramos que los resultados presentados en esta tesis contribuyen a ampliar el conocimiento teórico de la respuesta plasmónica del grafeno. En concreto, estudiamos la respuesta plasmónica de múltiples geometrías con el típico dopado uniforme incluyendo los efectos de no localidades y no linealidades, y también asumimos novedosas condiciones realistas de dopado no homogéneo. Por todo ello, creemos que esta tesis verdaderamente sienta las bases teóricas de futuros dispositivos experimentales basados en grafeno.

Abstract

Graphene is a planar monolayer of carbon atoms tightly packed into a 2D honeycomb lattice. Since its first experimental isolation by K. Novoselov and A. Geim in 2004, graphene has attracted an enormous interest due to its extraordinary optoelectronic properties for nanophotonics (a branch of physics that studies the interaction of light with matter over characteristic lengths in the nanometer range). Specifically, its bidimensional nature and singular atomic structure are translated into an unconventional linear dispersion relation, very different from the parabolic relation in typical noble metals.

When materials are structured over length scales that are smaller or comparable to the wavelength of the incident light, their electromagnetic interaction displays interesting phenomena, including the excitation of plasmons (*i.e.*, collective oscillations of bonded electrons in noble metals or graphene). Due to their tight confinement (below the diffraction limit of light), plasmons enable an intense light-matter interaction, in addition to large electric field enhancement. Remarkably, plasmons strongly depend on the shape and size of the supporting material, on the dielectric environment, and on the number of oscillating bounded electrons (related to the detailed electronic band structure of the material). A strict control of these properties is required to engineer the plasmonic response of the sustaining nanostructures.

The honeycomb lattice of graphene is the result of the sp^2 hybridization between one s orbital and two p orbitals per carbon atom forming σ-bonds with a characteristic angle of 120° between them. A third p (also named as π) orbital remains oriented perpendicularly to the atomic layer and can bind weakly through van der Waals interaction with additional carbon layers or other materials. The unique band structure of graphene produced by these π orbitals consists of a lower or valence band and an upper or conduction band, which at low energies resemble the

shape of two inverted cones touching at one point. This point is the so-called Dirac point and marks the Fermi level in the neutral state. In this state, the valence band is completely filled with delocalized π electrons, while the conduction band is empty. The absence of an optical gap between both bands permits one to treat graphene in this neutral state as a zero-energy bandgap semiconductor, where only electron-hole pair interband transitions can occur.

The collective oscillation of the π electrons gives rise to the so-called π intrinsic plasmons with energies $\gtrsim 4.5\,\mathrm{eV}$, confining them in the ultraviolet region of the electromagnetic spectrum. Moreover, these plasmons present a low tunability, so their relevance for nanophotonics is limited. Interestingly, when extra electrons are added to graphene, they start filling unoccupied states in the conduction band up to a certain level that corresponds to the new shifted Fermi level $E_\mathrm{F} = \hbar v_\mathrm{F}\sqrt{\pi n}$, where n is the density per unit area of these extra electrons, and $v_\mathrm{F} \approx c/300$ their velocity. Therefore, an optical gap of width $2E_\mathrm{F}$ opens, and electron-hole pair intraband transitions are enabled in addition to interband. The process of adding new electrons is known as doping, and due to the symmetry of the bands, it produces the same effect as when removing π electrons from the lower cone (*i.e.*, doping with holes instead of electrons). The tunability of the Fermi level with n, as well as the peculiar linear dispersion relation, are unique properties of graphene in comparison with typical noble metals. In contrast to graphene, noble metals do not show a salient tunability as significant changes in n barely affect their global optoelectronic properties.

The collective oscillations engaging extra electrons in doped graphene are known as Dirac plasmons, and their resonances embrace from THz to near infrared frequencies. They are commonly subdivided into two different subgroups depending on their propagating features: surface plasmon polaritons (SPPs) and localized surface plasmons (LSPs). The former are propagating electromagnetic modes sustained by extended graphene layers acting as an interface layer between two different dielectric media, and that cannot be directly excited by external light due to momentum mismatch. The latter are confined modes sustained by finite nanostructures that, in turn, can be effectively excited by light. Dirac plasmons present a bunch of appealing properties in comparison with those of noble metals (*e.g.*, they have longer lifetimes and higher quality factors, they show strong nonlinearities, and they possess the ability to boost the electric field enhancement by several orders of magnitude).

Furthermore, SPPs display a much shorter wavelength than the incident light, which translates into a larger degree of field confinement. The control of these properties has spurred the development of new theoretical models able to predict the plasmonic response of graphene, promoting its application to optical detection, sensing, nonlinear optics, and light modulation.

The optical dispersion of graphene Dirac plasmons is governed by the dynamics of the extra electrons in the conduction band. The simplest model capable of giving a fairly accurate description is the Drude model, where only intraband transitions at zero temperature are considered. Despite its simplicity, this model is considered a good approximation at photon energies well below the doping level. If this condition is not satisfied, a more elaborate and realistic model like the random-phase approximation shows up including the effects of a finite temperature and interband transitions. We present an extensive comparison between both models for different doping levels in the first chapter of this thesis.

The theoretical electromagnetic modeling of graphene in the classical limit is based on the solution of macroscopic full-retarded Maxwell's equations. Throughout this thesis, the exact solution of Maxwell's equations is obtained by the boundary-element method. Within this procedure, a system of surface-integral equations is evaluated at the boundaries of a non-magnetic, local (*i.e.*, independent of the parallel wave vector $k_{\parallel}$ of the incident light), and linear (*i.e.*, polarization responding linearly to the electric field of the incident light) graphene nanostructure with an arbitrary shape. After determining the boundary conditions, a rigorous numerical solution is accomplished through a finite discretization of the graphene boundaries, with the carbon layer modeled as a thin film, and with a denser surface grid placed near the film edges. Despite the versatility of this method, finding a solution can be a highly time-consuming process. However, for nanostructures with characteristic length D much smaller than the incident light wavelength, we can safely work in the electrostatic limit (*i.e.*, non-retarded approach). Here, the interaction between light and graphene is regarded as instantaneous, and the problem reduces to solving the Poisson equation with the appropriate boundary conditions. Under these assumptions, we observe that the plasmonic response of graphene derived from electrostatics is in excellent agreement with the full numerical solution of Maxwell's equations. Moreover, in the last section of the first chapter, we derive a useful analy-

tical electrostatic scaling law that permits obtaining the resonance frequencies of the LSPs for any arbitrary shape by just knowing the size, doping level, and dielectric environment of the graphene nanostructure. Specifically, we show that the resonance frequencies of the LSPs fulfill approximately the expression $\omega_{\rm p} \propto \sqrt{E_{\rm F}/D}$, which already illustrates their strong tunability.

In actual experiments, the doping of graphene is generally achieved via chemical methods or electrostatic gating. In the latter, a potential difference with respect to a backgate is applied to graphene, thus inducing a perpendicular electric field $\mathbf{E}_0$ that is uniformly applied to one side of graphene, so that an induced doping density of electrons $n = -E_0/4\pi e$ is distributed to screen the field completely. For simplicity, LSPs are extensively studied in the literature assuming a uniform distribution of n over the graphene nanostructure. However, we find that n is actually distributed inhomogeneously with a profile depending on the specific geometrical configuration, thus affecting the plasmonic response of the carbon film. We analyze this behavior in the second chapter of this thesis, where we classically study different realistic doping configurations in nanoribbons, nanodisks, and extended graphene layers. We find that Dirac plasmons are sensitive to inhomogeneous doping distributions, and thus, the particular plasmonic response needs to be considered for the correct design of device applications.

When the characteristic length of the nanostructure is of the order of the Fermi wavelength (*i.e.*, the de Broglie wavelength in the vicinity of the Fermi energy, which for graphene is $\lambda_{\rm F} = \sqrt{4\pi/n} = hv_{\rm F}/E_{\rm F} \approx 10.33\,{\rm nm}$ when $E_{\rm F} = 0.4\,{\rm eV}$; note that its tunability with n contrasts with the nearly constant value in noble metals: $\lambda_{\rm F} \approx 0.52\,{\rm nm}$ in gold), classical electromagnetism is no longer valid, and a quantum-mechanical approach for the description of the plasmonic response is necessary. In the third chapter of this thesis, we provide extensive quantum calculations (including nonlocal and edge effects, where we can distinguish between armchair or zigzag terminations) through a tight-binding model, in combination with the random-phase approximation. In particular, we notice that for narrow single and interacting nanoribbons, classical calculations disregard several physical effects that affect the plasmonic response of graphene. For example, when the doping level is lower than the resonance frequencies of the lowest-order dipolar LSPs, these are strongly quenched by zigzag edges and decay through the excitation of electronic zero-energy edge

states. Besides, for armchair terminations, LSPs are also affected by nonlocalities leading to slight blueshifts and broadening. Furthermore, we note that nonlocal effects play an important role in interacting islands at short separations, which give rise to remarkable corrections in the resonance frequencies of the sustained LSPs. In fact, we conclude that graphene is a suitable platform for studying the quantum effects and nonlocalities on LSPs.

The fourth chapter of this thesis is devoted to the study of the strong nonlinear plasmonic response of doped graphene. Specifically, we present a review of three of the most important nonlinear processes: second-harmonic generation, third-harmonic generation, and Kerr effect. Moreover, starting from the Boltzmann transport equation, we extend the electrostatic scaling law formalism to nonlinear orders of the graphene conductivity and electric polarizability. We also provide a detailed comparison between the classical and quantum nonlinear plasmonic response of small equilateral graphene nanotriangles. We find that the classical approach underestimates nonlinearities except for low levels of doping. Our results reveal the crucial relevance of a comprehensive knowledge of nonlinear effects in graphene.

Finally, in the fifth chapter, we show the outstanding potential of graphene LSPs to resolve the chemical identity of molecules. It is known that the identification of molecules usually involves the employment of inefficient sensing techniques including the use of costly spectrometers and laser sources. In order to avoid this, we present a new sensing mechanism that simply requires infrared lamps and doped graphene nanodisks. We prove that graphene LSPs allow the molecule to enhance greatly its capability to absorb or inelastically scatter impinging light changing its roto-vibrational energy. These absorption and scattering processes are the elementary principles of the spectroscopy techniques known as surface-enhanced infrared absorption and surface-enhanced Raman scattering, for which we obtain intensity enhancements of $\sim 10^3$ and $\sim 10^4$, respectively. We claim that by just integrating the sensing signal over a broadband spectral range as a function of the graphene doping level E_{F}, we can identify the chemical fingerprints of the molecule with an energy resolution given by the spectral width of the graphene LSPs.

In conclusion, we consider that our results contribute to broadening the theoretical understanding of the plasmonic response of graphene under the usual assumption of uniform doping including the effects of nonlocalities and nonlinearities, and also

under novel realistic inhomogeneous doping conditions. We believe that this thesis paves the way for future experimental studies of graphene-based nanodevices.

Chapter 1

Introduction

In this initial chapter, we discuss the general properties of graphene, the key material to which this thesis is devoted. In particular, we start by succinctly analyzing its history in the context of the discovery of different carbon allotropes (*i.e.*, diverse structural forms of carbon). We continue with a brief review on how to grow graphene experimentally, and then we study its singular band structure and multiple optoelectronic properties derived from its bidimensional character. For this purpose, we use a macroscopic classical approach for the electromagnetic description of graphene. Additionally, the quantum-mechanical model used in further chapters for a detailed microscopic study is also presented here. Finally, we analyze the main properties of the surface plasmons sustained by graphene.

1.1 History of graphene and other carbon allotropes

The first carbon allotrope known in history was the 3D graphite [see Fig. 1.1(c)]. It was discovered in England in the 16th century [1] and chiefly used in pencils. Although the functionality of pencils promptly spread all over the world, the ongoing term "graphite" was not conceived until 1789 by the geologist A. Werner, thus remarking its use for graphical reasons [2]. The atomic structure of graphite consists of stacked graphene layers and its utility for writing derives from the weak van der

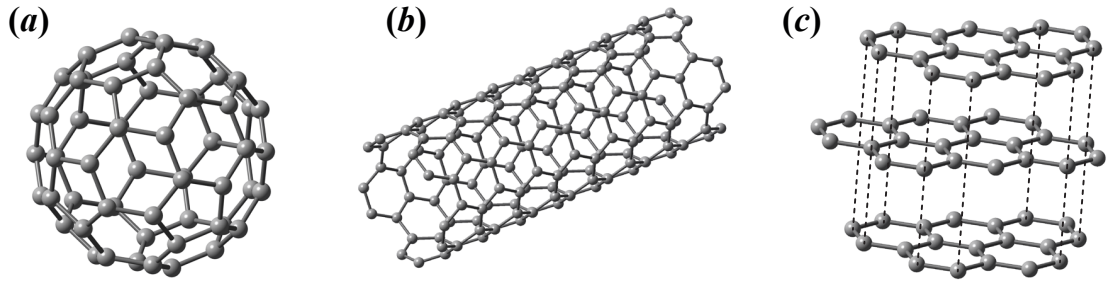

Figure 1.1: Plots of different carbon allotropes where each sphere represents a carbon atom. (a) 0D molecule of C_{60}, (b) 1D carbon nanotube, and (c) 3D graphite.

Waals forces between the different sheets. In fact, after pressing a pencil against a sheet of paper, stacks of graphene are exfoliated from the graphite, and it is actually possible to find individual graphene layers adhered to the surface.

Fullerenes are carbon molecules arranged in a spherical-like shape so that they can be considered as a 0D structure. The most representative fullerene structure is the C_{60} molecule also called "buckyball" [see Fig. 1.1(a)]. This C_{60} molecule was first detected in 1985 [3], although its existence had been predicted previously [4]. Besides, fullerenes can be directly constructed from graphene with the replacement of some hexagons by pentagons creating positive curvature defects that result in a wrapped-up structure [5].

Single-walled carbon nanotubes (CNTs) were discovered in 1991 [6]. They present only hexagons wrapped into a seamless cylinder [see Fig. 1.1(b)], so that they are regarded as 1D cylindrical molecules with a diameter in the order of the nanometer.

However, due to the lack of tools for searching carbon flakes, we had to wait until 2004 for the milestone of the experimental isolation of the 2D carbon allotrope: graphene [7]. Graphene is a one-atom-thick monolayer of carbon atoms tightly arranged in a purely bidimensional honeycomb lattice [see Fig. 1.2(a)]. The physicists K. Novoselov and A. Geim from Manchester University (both awarded the Physics Nobel Prize in 2010) showed that, by just rubbing graphite over a silica substrate in a process known as "mechanical exfoliation", graphene could be readily detected by regular microscopy techniques [8]. Soon after, simultaneously with P. Kim from Columbia [9], they found evidence of the quantum Hall effect in graphene [10].

1.2 Synthesis of graphene

In this section, we review the main techniques so far developed for the synthesis of graphene. Some of them are feasible with modest means while others require advanced experimental equipment. Furthermore, the resulting samples do not present exactly the same properties. Specifically, the main synthesis techniques are:

• *Mechanical exfoliation*: This is the most straightforward and, as mentioned in the previous section, the original technique used for the synthesis of graphene. Its principal advantages are that it is an easy way of producing graphene and that the resulting layers present high quality and great electrical properties.

However, this technique presents a serious disadvantage: the distribution of the layers over the substrate is completely random and the subsequent identification of single layers of graphene is very time-consuming and difficult to scale up.

• *Epitaxial growth*: This promising technique consists of exposing hexagonal-like silicon carbide substrates (SiC) to temperatures $\sim 1300\,^{\circ}\mathrm{C}$ so that the silicon atoms evaporate and the remaining carbon atoms form graphene [11]. Unfortunately, the charge distribution of the remaining graphene nanostructures is not always uniform.

• *Chemical vapor deposition* (CVD): This is the most popular method to produce relatively high-quality graphene on a large scale. In this technique, disassociated carbon atoms in gas phase are accumulated on a substrate at a temperature of $\sim 1000\,^{\circ}\mathrm{C}$. The main problem with this technique is the complicated separation of graphene from the substrate once the system has cooled down.

1.3 Optoelectronic properties

1.3.1 sp^2 hybridization

Carbon, the elementary basis of all the organic molecules, is the fundamental component of graphene. Its most common isotope, ${}^{12}_{6}\mathrm{C}$, possesses 6 protons and 6 neutrons in the atomic nucleus, and 6 electrons moving freely in different orbitals. Thus, the electronic configuration of a carbon atom in the ground state is $1s^2 2s^2 2p^2$, with two electrons confined in the inner orbital 1s, other two electrons in 2s, and the two remaining allocated in the orbitals 2p. The energy difference between the 2s orbital

and the three 2p orbitals (we name them as $2p_x, 2p_y$, and $2p_z$) is $\sim 4\,\text{eV}$, hence in the ground state it is more favorable in terms of energy that two electrons fill the orbital 2s and the other two stay in distinct orbitals 2p.

However, when various carbon atoms are in close proximity, it is more favorable to excite one electron from the 2s orbital to the remaining 2p empty orbital, thus forming covalent bonds between electrons of different atoms. Since the energy gain with the covalent bond is $> 4\,\text{eV}$, the system tends to stay in this excited state. Therefore, we have four identical quantum states $|2s\rangle, |2p_x\rangle, |2p_y\rangle$, and $|2p_z\rangle$ that can combine resulting in different sp^i ($i = 1, 2$, and 3) hybrid orbitals.

Graphene presents sp^2 hybridization [*i.e.*, the orbitals $2s, 2p_x$, and $2p_y$ hybridize and combine among themselves forming a trigonal planar structure with an angle of 120° between the carbon atoms as shown in Fig. 1.2(a)]. Carbon atoms in graphene are separated a distance $a_0 = 1.421\,\text{Å}$ and are strongly bonded between them by means of covalent σ bonds, which are responsible for the strength of the planar carbon structure. The remaining $2p_z$ or π orbital is oriented perpendicularly to the atomic plane and can bind covalently with other π orbitals of different atoms. Each carbon atom of graphene possesses one π orbital containing one π electron, and then, due to the spin degeneracy (*i.e.*, $g_s = 2$) the π orbitals are half populated. These π electrons are delocalized and, as we explain in the next section, they form two bands: a lower-energy one (π, valence, or bonding band that is completely filled with electrons) and an upper-energy one (π^*, conduction, or anti-bonding band that is completely empty).

1.3.2 Graphene band structure

The atomic structure of graphene is plotted in Fig. 1.2(b) and can be understood as a triangular lattice with two atoms per unit cell (see shaded area) composed by two intersecting triangular Bravais sublattices. The lattice vectors are[1]

$$\boldsymbol{a}_1 = \frac{a_0}{2}\left(3, \sqrt{3}\right), \quad \boldsymbol{a}_2 = \frac{a_0}{2}\left(3, -\sqrt{3}\right). \tag{1.1}$$

[1] Gaussian units are used in all the equations throughout this thesis.

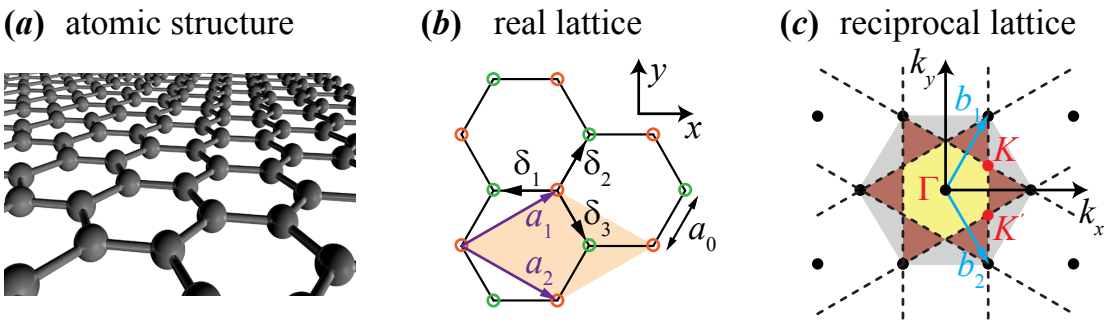

Figure 1.2: Bidimensional honeycomb lattice of graphene. (a) Sketch of the atomic structure of 2D graphene. (b) Triangular lattice of graphene formed by two intersecting triangular Bravais sublattices. The carbon atoms of each sublattice are represented by the green and orange dots, respectively. The lattice vectors are $\boldsymbol{a}_1$ and $\boldsymbol{a}_2$. The vectors $\boldsymbol{\delta}_1$, $\boldsymbol{\delta}_2$, and $\boldsymbol{\delta}_3$ connect nearest neighbor atoms. The distance between the carbon atoms is $a_0 = 1.421\,\text{Å}$. The shaded region is the area of the unit cell $A_0 = 3\sqrt{3}a_0^2/2$. (c) Reciprocal lattice of graphene. The yellow hexagonal region represents the first Brillouin zone with center at Γ while the brown and the grey represent the second and the third, respectively. The reciprocal lattice vectors (blue arrows) are $\boldsymbol{b}_1$ and $\boldsymbol{b}_2$. The Dirac points are represented by red dots in the corners of the 1BZ and named as K and K'.

The resulting reciprocal lattice is shown in Fig. 1.2(c) and presents vectors in the momentum space with coordinates

$$\boldsymbol{b}_1 = \frac{2\pi}{3a_0}\left(1, \sqrt{3}\right), \quad \boldsymbol{b}_2 = \frac{2\pi}{3a_0}\left(1, -\sqrt{3}\right), \tag{1.2}$$

that fulfill the condition $\boldsymbol{a}_i \cdot \boldsymbol{b}_j = 2\pi\delta_{ij}$, where δ_{ij} is the Kronecker delta. Furthermore, the vectors connecting the three nearest neighbor atoms in the real space are

$$\boldsymbol{\delta}_1 = -a_0(1,0), \quad \boldsymbol{\delta}_2 = \frac{a_0}{2}(1,\sqrt{3}), \quad \boldsymbol{\delta}_3 = \frac{a_0}{2}(1,-\sqrt{3}). \tag{1.3}$$

The first Brillouin zone (1BZ) of graphene corresponds to the yellow shaded hexagonal region with center at the Γ point as detailed in Fig. 1.2(c). The vertex of this 1BZ are named as K and K' points, and present the coordinates

$$K = \frac{2\pi}{3\sqrt{3}a_0}\left(\sqrt{3}, 1\right), \quad K' = \frac{2\pi}{3\sqrt{3}a_0}\left(\sqrt{3}, -1\right). \tag{1.4}$$

They are usually called Dirac points for reasons that we explain below and play a central role in the optoelectronic properties of graphene. Interestingly, the other four vertex of the 1BZ are equivalent to either K or $K^{'}$ because the former can be obtained through a translation of the reciprocal lattice vectors. So that by just considering the pair of Dirac points K and $K^{'}$, we can describe graphene in the momentum space (*i.e.*, graphene is doubly degenerate with $g_v = 2$ as the valley degeneracy).

The optoelectronic response of graphene at low energies is governed by the excitation of electrons from the π to the π^* band. A simple tight-binding model (TB) [12, 13] is sufficient to provide an excellent quantitative description of these bands. Here, π electrons can hop between nearest and next-nearest sites. The electronic states j of one π electron in the valence band are constructed as a linear combination of the states $\sum_l a_{jl} |l\rangle$ of the orbitals $2p_z$, where l runs over each carbon site. Remarkably, the influence of the σ band is not considered since it presents low energy only contributing to a nearly uniform background polarization. The TB model yields two energy bands with a form given by [12]

$$\epsilon_{\mathbf{k}}^{\pm} = \frac{\pm t\gamma_{\mathbf{k}}}{1 \mp s\gamma_{\mathbf{k}}}, \tag{1.5}$$

where $\mathbf{k}$ is the wave vector in the momentum space while the $+$ superindex in $\epsilon_{\mathbf{k}}$ refers to the upper or π^* band, and $-$ to the lower or π band. The parameter $t \sim 2.8\,\text{eV}$ is the nearest neighbor hopping energy and its value –deduced from scanning tunneling microscope (STM) measurements of graphene nanoislands [14]– agrees with *ab initio* calculations [13]. The parameter $s \sim 0.1\,\text{eV}$ corresponds to the next-nearest-neighbor hopping energy [15]. Finally, the dependence on the reciprocal vectors is enclosed in the dimensionless parameter

$$\gamma_{\mathbf{k}} = \sqrt{1 + 4\cos^2\left(\frac{\sqrt{3}k_y a_0}{2}\right) + 4\cos\left(\frac{\sqrt{3}k_y a_0}{2}\right)\cos\left(\frac{3k_x a_0}{2}\right)}. \tag{1.6}$$

We represent in Fig. 1.3(a) the full band structure of graphene resulting from this TB approach. Due to the consideration of non-zero next-nearest-neighbor hopping energy, both bands are asymmetric with respect to the level of zero energy. Each

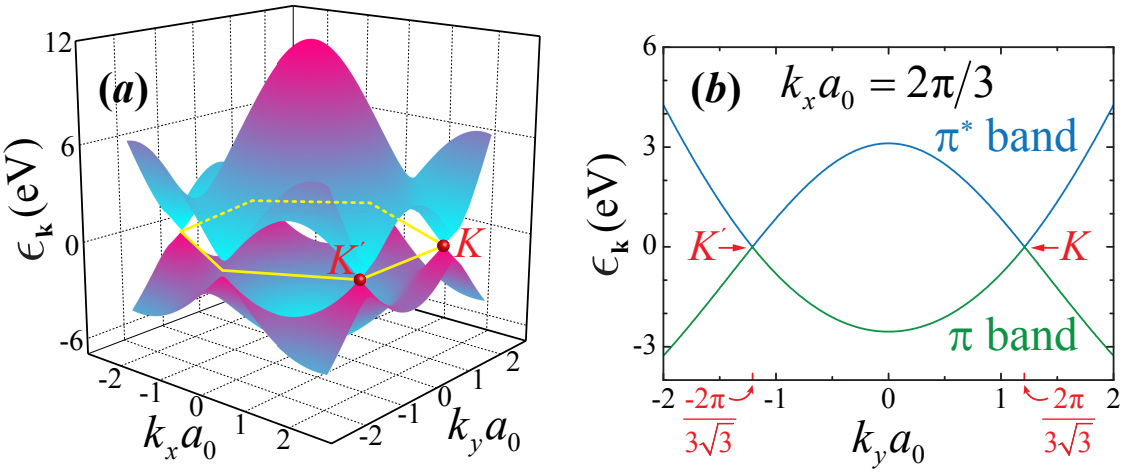

Figure 1.3: Graphene band diagram. (a) Spectrum of the electronic band structure of graphene given by Eq. (1.5), considering the nearest neighbor hopping energy $t \sim 2.8\,\text{eV}$, and the next-nearest-neighbor hopping energy $s \sim 0.1\,\text{eV}$. The yellow hexagon represents the limits of the 1BZ depicted in Fig. 1.2(c). (b) Slice of panel (a) when $k_x a_0 = 2\pi/3$, showing the linear dispersion near the Dirac points (K and K'), where both bands are degenerate and get the same null value (*i.e.*, $E_\text{F} = 0$). The upper band (blue curve) is the so-called π^* or antibonding band while the lower (green curve) is the π or bonding band.

band contains the same number of states, and since the electron of each carbon atom can occupy either a spin-up or spin-down state, the π band is completely full, while the π^* remains empty. We observe that the gap between both bands closes at the Dirac points. These points are the center around which low-energy excitations are created and also mark the Fermi level ($E_\text{F} = 0$) of pristine (undoped) graphene. Furthermore, due to the time-reversal symmetry, at low energies the bands fulfill the condition $\epsilon_{\mathbf{k}} = \epsilon_{-\mathbf{k}}$.

In Fig. 1.3(b) we plot the intersection of the band structure with the plane $k_x a_0 = 2\pi/3$. As we can observe, the bands around the Dirac points resemble two inverted cones (Dirac cones), and at energy scales $\lesssim 1\,\text{eV}$, they show an approximately linear dispersion relation. At this point, it is convenient to define the bidimensional vector $\mathbf{q} = \mathbf{k} - \boldsymbol{K}$, as the momentum measured relatively to the Dirac points which fulfills $|\mathbf{q}| \ll |\boldsymbol{K}|$. If we neglect the next-nearest-neighbor hopping energy ($s = 0$) and we

expand the expression of Eq. (1.6) around $\mathbf{q} = 0$, we obtain

$$\epsilon_{\mathbf{q}}^{\pm} \approx \pm\hbar v_{\mathrm{F}}|\mathbf{q}| + \mathcal{O}\left(\frac{q}{K}\right)^2, \tag{1.7}$$

where $v_{\mathrm{F}} = (3ta_0/2\hbar) \approx c/300$ is the Fermi velocity in graphene that is independent of the electron energy.

A linear dispersion relation is generally associated with massless particles like photons and can be quantum mechanically described by the relativistic Dirac equation [16]. Moreover, ultrarelativistic particles like neutrinos (the kinetic energies are much higher than their rest masses energy) can be also described by this equation if their small but finite masses are neglected. Note that if this approximation is dropped, neutrinos are described by coupled Dirac equations with different mass states [17]. So the reason why the vertex of the 1BZ in graphene are called Dirac points is because of the resemblance to the electron and positron bands touching at the zero momentum in the zero-mass limit of the Dirac equation, and also because the dynamics of graphene electrons can be fully described by this Dirac equation.

Therefore, due to the massless-like behavior of graphene electrons, we can directly obtain quantities like the charge carrier density n and the cyclotron mass m_e^*. The electronic density depends on the Fermi surface which separates the occupied from the unoccupied electronic states. Considering that graphene is a bidimensional material of characteristic size D, the number of electrons or charge carriers in graphene is defined as $N_e = g_s g_v \left[\pi k_{\mathrm{F}}^2 / \left(2\pi/D\right)^2\right]$. We include the valley degeneracy due to the contribution of both Dirac points in each 1BZ. Hence, the charge carrier density in graphene $n = N_e/D^2$ finally reads

$$n = \frac{k_{\mathrm{F}}^2}{\pi}. \tag{1.8}$$

Additionally, the cyclotron mass is defined in the semiclassical approximation [18] as

$$m_e^* = \frac{\hbar^2}{2\pi}\frac{\partial\left[\pi k^2(\epsilon)\right]}{\partial\epsilon}\bigg|_{\epsilon=E_{\mathrm{F}}} = \frac{\hbar k_{\mathrm{F}}}{v_{\mathrm{F}}} = \frac{\hbar\sqrt{\pi n}}{v_{\mathrm{F}}}. \tag{1.9}$$

This variable value is in contrast to the constant value in noble metals due to their parabolic dispersion relation.

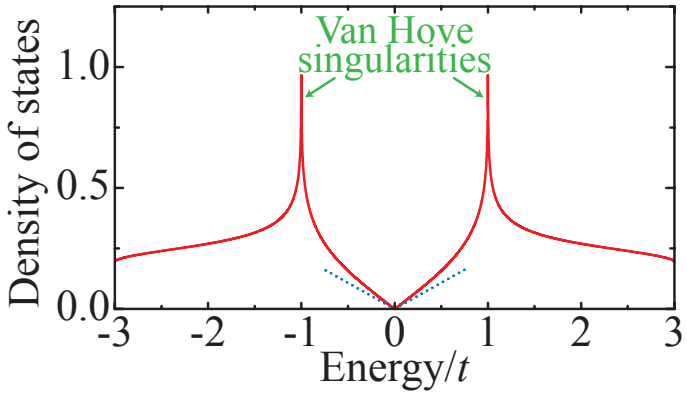

Figure 1.4: Scheme of the electronic density of states per unit cell (red solid curves) as a function of the energy normalized to the nearest neighbor hopping energy $t \sim 2.8\,\text{eV}$. We neglect the next-nearest-neighbor hopping energy. The blue dotted lines represent the linear-like evolution around the Dirac points given by Eq. (1.10). The divergences at energies equal to $\pm t$ are Van Hove singularities.

1.3.3 Density of states

Another quantity that indicates the uniqueness of graphene is the electronic density of states per unit cell $\rho(\epsilon) = \partial N_\epsilon / \partial \epsilon$. Specifically, it gives the number of electronic states N_ϵ below a fixed energy ϵ. In the absence of next-nearest-hopping energy (*i.e.*, $s = 0$), the full analytical expression of the density of states [19] can be found in Eq. (14) of Ref. [20], and it is depicted within red solid curves in Fig. 1.4. In the vicinity of the Dirac points, the expression of the density of states can be simply approximated as [20]

$$\rho(\epsilon) = \frac{2A_0|\epsilon|}{\pi\hbar^2 v_{\text{F}}^2}, \tag{1.10}$$

where $A_0 = 3\sqrt{3}a_0^2/2$ is the area of the unit cell. This approximated behavior is represented by blue dotted lines in Fig. 1.4.

The first conclusion extracted from Eq. (1.10) is that the density of states per unit cell in graphene actually evolves with the energy, which is in contrast to the usual constant response of electrons in 2D materials $\rho(\epsilon) = m_e^* A_0/\pi\hbar^2$ that possess an energy dispersion $\epsilon = \hbar^2 q^2/2m_e^*$. Moreover, both the full analytical and the approximated solution vanish at the Dirac points. Finally, we need to remark that

the divergences observable in Fig. 1.4 at $\pm t$ energies correspond to the so-called Van Hove singularities [21] which always appear at the border of the 1BZ for wave vectors situated exactly in between the Dirac points. This is because the density of states in the vicinity of the Dirac points approximately evolves with the inverse of the derivative of the energy with respect to the momentum, and from Fig. 1.3(b) we observe that at half distance between K and K', the curves are flat.

1.3.4 High electrical mobility

The electrical mobility μ –the capability of electrons to move as a response to an electric field– is mainly determined by the scattering mechanisms of electrons with phonons (vibrational modes of the atomic lattice), lattice defects, or other electrons.

The electrical mobility in graphene is remarkably higher compared to typical noble metals. At low temperatures ($\lesssim 100\,\mathrm{K}$), the graphene mobility barely changes [10]. This indicates that in this range, the scattering mechanisms are dominated by the lattice defects, which are nearly temperature independent. Interestingly, these lattice defects can be produced extrinsically or intrinsically. The former appear in different forms such as vacancies, adatoms, surrounding charges, or geometrical defects like edges and cracks. The latter are produced by topological defects and surface ripples.

At room temperature, other aspects like the method of fabrication, the high sound velocity or the suppression of backscattering effects affect directly the reachable graphene mobility. For example, experimental transport measurements estimate that the electron mobility in graphene [22] is $\mu \approx 10000\,\mathrm{cm}^2/(\mathrm{V\,s})$. For exfoliated graphene at low temperatures, it can reach up [23] to $\mu \approx 20000$. However, even higher mobilities have been observed in boron nitride supported graphene [24] ($\mu \approx 60000$), and in high-quality suspended graphene [25] ($\mu > 100000$).

1.4 Electromagnetic modeling of graphene

In this section, we present various theoretical ways of describing the interaction of graphene with external light, ranging from a classical approach to more elaborate microscopic quantum-mechanical models. The applicability of the former vanishes

when the characteristic size of the graphene nanostructure is of the order of the Fermi wavelength ($\lambda_{\mathrm{F}} = \sqrt{4\pi/n} = hv_{\mathrm{F}}/E_{\mathrm{F}}$) and then, a quantum-mechanical approach is strictly required. In classical electromagnetism, the rigorous solution is derived by fully solving the macroscopic Maxwell's equations. However, an alternative method holds when the size of the graphene nanostructure is much smaller than the wavelength of the incident light in the surrounding medium. Thus, the problem reduces to electrostatics.

1.4.1 Classical description

In classical electromagnetism, all phenomena can be described via the solution of macroscopic full-retarded Maxwell's equations in 3D space [26]

$$\begin{aligned} \nabla \times \mathbf{E}(\mathbf{r},\omega) &= \mathrm{i}k\mathbf{B}(\mathbf{r},\omega), \\ \nabla \times \mathbf{H}(\mathbf{r},\omega) &= -\mathrm{i}k\mathbf{D}(\mathbf{r},\omega) + \frac{4\pi}{c}\mathbf{J}(\mathbf{r},\omega), \\ \nabla \cdot \mathbf{D}(\mathbf{r},\omega) &= 4\pi\rho(\mathbf{r},\omega), \\ \nabla \cdot \mathbf{B}(\mathbf{r},\omega) &= 0, \end{aligned} \tag{1.11}$$

where $k = \omega/c$ is the free-space light wave vector of the incident continuous plane wave, and $\mathbf{E}(\mathbf{r},\omega)$ [$\mathbf{H}(\mathbf{r},\omega)$] is the electric (magnetic) field. We define $\mathbf{E}(\mathbf{r},\omega)$ as the sum of the external field $\mathbf{E}^{\mathrm{ext}}(\mathbf{r},\omega)$ and the induced field $\mathbf{E}^{\mathrm{ind}}(\mathbf{r},\omega)$ generated by the charge carrier density. The electric displacement is given by $\mathbf{D}(\mathbf{r},\omega)$ and the magnetic induction by $\mathbf{B}(\mathbf{r},\omega)$. The charge and the current densities, represented by $\rho(\mathbf{r},\omega)$ and $\mathbf{J}(\mathbf{r},\omega)$ respectively, are the sources that establish the shape and intensity of the fields.

In the above expressions, we consider that graphene is a linear, non-magnetic medium that presents temporal dispersion and local behavior. This is easily observable in the optical frequency regime, while the latter can be assumed since nonlocality (dependence on the parallel wave vector $k_{\parallel}$ of the incident radiation) is only relevant when the characteristic size of the material is of the order of the Fermi wavelength (*e.g.*, $\lambda_{\mathrm{F}} \approx 10.33\,\mathrm{nm}$ when $E_{\mathrm{F}} = 0.4\,\mathrm{eV}$). Furthermore, Maxwell's equations need to be supplemented with constitutive equations to get a self-consistent solution

that relates the interaction between the electromagnetic radiation and graphene:

$$\mathbf{D}\left(\mathbf{r},\omega\right)=\varepsilon\left(\mathbf{r},\omega\right)\mathbf{E}\left(\mathbf{r},\omega\right),\ \ \mathbf{B}\left(\mathbf{r},\omega\right)=\mathbf{H}\left(\mathbf{r},\omega\right), \tag{1.12}$$

where the frequency dependence of the media on the electromagnetic fields is encompassed now in the local dielectric function $\varepsilon(\mathbf{r},\omega)$ and an $\exp(-\mathrm{i}\omega t)$ temporal dependence is always assumed.

Throughout this thesis, the exact solution of full-retarded Maxwell's equations is obtained using the boundary-element method (BEM) [27]. In BEM, a system of surface-integral equations is evaluated at the boundaries of geometries with arbitrary shapes. Once we determine the boundary conditions satisfied by the surface charges and currents, the system is numerically solved by discretizing the boundaries with a finite number of points.

Nevertheless, when the graphene nanostructures present a size much smaller than the incident light wavelength (*i.e.*, $D \ll \lambda$), their response can be described in the electrostatic limit (*i.e.*, non-retarded limit where we assume $c \to \infty$). The interaction between graphene and the external light is considered instantaneous, so that the temporal phase of the electromagnetic field is practically constant, and therefore, we can reduce our problem of finding the spatial field distribution to electrostatics [28]. The electric and magnetic fields are decoupled [*i.e.*, $\nabla \times \mathbf{E}\left(\mathbf{r},\omega\right)=0$ and $\nabla \times \mathbf{H}\left(\mathbf{r},\omega\right)=0$] and the solution of Maxwell's equations, considering negligible external currents and charges, reduces to solving Poisson equation with the appropriate boundary conditions,

$$\nabla\cdot\varepsilon(\mathbf{r},\omega)\nabla\Phi(\mathbf{r},\omega)=-4\pi\rho^{\mathrm{ind}}(\mathbf{R},\omega)\delta(z), \tag{1.13}$$

where $\rho^{\mathrm{ind}}(\mathbf{R},\omega)=-en(\mathbf{R},\omega)$ is the 2D induced charge density in the graphene plane and $\delta(z)$ is the Dirac Delta function. From the previous equation we can directly get the expression of the electric field $\mathbf{E}(\mathbf{r},\omega)=-\nabla\Phi(\mathbf{r},\omega)$, where we define $\mathbf{r}=(\mathbf{R},z)$ and assume that the graphene layer lies on the $z=0$ plane. Moreover, the continuity equation relates the induced density and the surface current as

$$\rho^{\mathrm{ind}}(\mathbf{R},\omega)=\frac{-\mathrm{i}}{\omega}\,\nabla\cdot\mathbf{J}(\mathbf{R},\omega). \tag{1.14}$$

This current can be also expressed as $\mathbf{J}(\mathbf{R},\omega) = -\sigma(\mathbf{R},\omega)\nabla\Phi(\mathbf{R},\omega)$, where $\sigma(\mathbf{R},\omega)$ is the in-plane graphene conductivity. As we will show in further sections, the solution of the former electrostatic expressions gives a suitably accurate optoelectronic response of the graphene nanostructures.

In the local classical description of graphene, the dielectric function of the nanostructures is characterized by the relation

$$\varepsilon(\omega) = 1 + \frac{4\pi \mathrm{i}\sigma(\omega)}{\omega t}, \tag{1.15}$$

where, for simplicity, we assume that graphene is an isotropic and uniformly doped material (by doping we refer to the process of changing the Fermi energy of graphene). Moreover, the value used in the simulations for the graphene thickness needs to be well converged with $t \to 0$ for finding a valid solution. Note that the nominal thickness of a one-atom-thick layer of graphene is $t_{\mathrm{nom}} \approx 0.334\,\mathrm{nm}$ (*i.e.*, the interlayer separation of graphite [29]).

The shape of the conductivity is characterized by the behavior of the free conduction electrons (or holes) sustained by graphene [see section (1.5.2)]. The simplest kinetic model that approximately describes the local dynamics of these electrons and its scattering processes is the Drude model [18]. Here, only intraband electron-hole (e-h) pair transitions at temperature $T = 0$ are considered [see section (1.5.2)], and the free electrons may decay through multiple channels (*e.g.*, collision with phonons, lattice defects or, more rarely, quenching with other electrons) with a phenomenological rate per unit time γ [this magnitude, also known as damping rate, comprises all the possible graphene loss channels, see section (1.5.3)]. The resulting graphene conductivity presents the form [30]

$$\sigma^{\mathrm{Drude}}(\omega) = \frac{\mathrm{i}e^2}{\pi\hbar^2}\frac{E_{\mathrm{F}}}{\omega + \mathrm{i}\gamma}. \tag{1.16}$$

Inserting this expression into Eq. (1.15), we can rewrite the dielectric function of graphene with a more recognizable expression according to the Drude model [26]

$$\varepsilon^{\mathrm{Drude}}(\omega) = 1 - \frac{\left(\omega_{\mathrm{bulk}}^{\mathrm{Drude}}\right)^2}{\omega\left(\omega + \mathrm{i}\gamma\right)}. \tag{1.17}$$

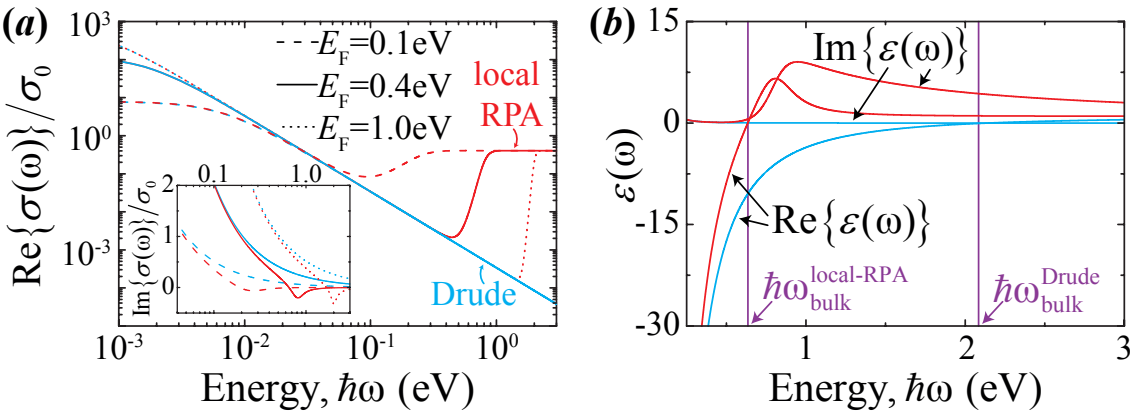

Figure 1.5: Conductivity and dielectric function of doped graphene. (a) Real part of the conductivity of doped graphene as a function of the incident photon energy. We compare the Drude model (blue curves) with the local-RPA model at temperature $T = 300\,\mathrm{K}$ (red curves) for different doping energies E_F. The inset shows the evolution of the imaginary part. The conductivity is normalized to that in pristine graphene $\sigma_0 = e^2/4\hbar$ [31]. (b) Evolution of the dielectric function $1 + 4\pi\mathrm{i}\sigma(\omega)/\omega t$ of a graphene slab with $E_\mathrm{F} = 0.4\,\mathrm{eV}$ and thickness $t = 0.5\,\mathrm{nm}$. The purple vertical lines represent the bulk plasma frequency corresponding to local-RPA and Drude models, respectively. At these frequencies, graphene changes from a metallic to a dielectric-like behavior. The mobility here used is $\mu = 10000\,\mathrm{cm}^2/(\mathrm{V\,s})$.

Here, $\omega_\mathrm{bulk}^\mathrm{Drude} = (2e/\hbar)\sqrt{E_\mathrm{F}/t}$ is the Drude bulk plasma frequency that depends on the graphene Fermi energy and the thickness [*e.g.*, for $E_\mathrm{F} = 0.4\,\mathrm{eV}$ and $t = 0.5\,\mathrm{nm}$ –well converged value with t_nom– we find $\hbar\omega_\mathrm{bulk}^\mathrm{Drude} \approx 2.15\,\mathrm{eV}$, as shown within the purple vertical line on the right side of Fig. 1.5(b)]. Using Eq. (1.9), this bulk plasma frequency can be also expressed as $\omega_\mathrm{bulk}^\mathrm{Drude} = \sqrt{4\pi n e^2/t m_e^*}$. The importance of $\omega_\mathrm{bulk}^\mathrm{Drude}$ relies on the fact that it determines how is the response displayed by graphene to external radiation:

- For $\omega < \omega_\mathrm{bulk}^\mathrm{Drude}$, doped graphene shows a behavior similar to metals, so that conduction electrons (or holes) are capable of screening external radiation. The dielectric function satisfies $\mathrm{Re}\{\varepsilon^\mathrm{Drude}(\omega)\}<0$.

- For $\omega > \omega_\mathrm{bulk}^\mathrm{Drude}$, doped graphene behaves as a dielectric to external radiation, so that light can propagate through it. The dielectric function satisfies $\mathrm{Re}\{\varepsilon^\mathrm{Drude}(\omega)\}>0$.

However, there are more elaborated models that take into account not only the scattering processes of the conduction electrons (or holes) and intraband transitions at $T = 0$, but also electronic interband transitions at finite temperatures. For example, within the random-phase approximation (RPA) [32, 33, 34, 35, 36] we can describe more realistically the conductivity of graphene [31] $\sigma^{\mathrm{RPA}}(k_{\parallel}, \omega) = -\mathrm{i}\omega\chi(k_{\parallel}, \omega)$, where $\chi(k_{\parallel}, \omega)$ is the linear graphene susceptibility. In the local limit ($k_{\parallel} \to 0$), the local-RPA conductivity [31, 37] is expressed as follows

$$\sigma^{\mathrm{local-RPA}}(\omega) = \frac{\mathrm{i}e^2}{\pi\hbar^2}\frac{-1}{\omega + \mathrm{i}\gamma}\int_{-\infty}^{\infty}\mathrm{d}\epsilon\left[|\epsilon|\frac{\partial f_\epsilon}{\partial\epsilon} + \frac{(\epsilon/|\epsilon|)}{1 - 4\epsilon^2/\left[\hbar^2\left(\omega + \mathrm{i}\gamma\right)^2\right]}f_\epsilon\right], \quad (1.18)$$

where f_ϵ is the Fermi-Dirac electron distribution as a function of the energy ϵ [see Eq. (1.21)].

The first term inside the integral of Eq. (1.18) corresponds to the intraband transitions –dominant at photon energies roughly below the Fermi energy E_{F}– and can be integrated analytically resulting in $\mathrm{i}e^2E_{\mathrm{F}}^*/\hbar^2\left(\omega + \mathrm{i}\gamma\right)$, with $E_{\mathrm{F}}^* = E_{\mathrm{F}} + 2k_{\mathrm{B}}T\ln\left(1 + \mathrm{e}^{-E_{\mathrm{F}}/k_{\mathrm{B}}T}\right)$, thus converging to the Drude model at $T = 0$.

The second term inside the integral of Eq. (1.18) corresponds to interband transitions and needs to be solved numerically. As depicted by the red curves in Fig. 1.5(a) for different Fermi energies, this term contributes a step function to the real part of $\sigma^{\mathrm{local-RPA}}(\omega)$ when $\epsilon \approx 2E_{\mathrm{F}}$, which is smoothed by the inclusion of finite values of the temperature and damping. The effect of the interband transitions is also appreciable in the imaginary part of $\sigma^{\mathrm{local-RPA}}(\omega)$ with a clear valley again at $\epsilon \approx 2E_{\mathrm{F}}$ [see red curves of the inset of Fig. 1.5(a)]. Moreover, we show in Fig. 1.5(b) the evolution of the real and imaginary parts of the dielectric functions for the two local classical models under study. Although the Drude model (blue curves) can be considered a good approximation (particularly when $\epsilon \ll E_{\mathrm{F}}$ for E_{F} smaller than the optical phonon energy $\sim 0.2\,\mathrm{eV}$ [38]), an in-depth analysis of the graphene conductivity including the interband transitions and finite temperature effects result in clear redshifts of the bulk plasma frequency. Additionally, since the choice of sign for time-dependence is $\exp(-\mathrm{i}\omega t)$, we find in the whole frequency spectrum for both models that $\mathrm{Im}\{\varepsilon(\omega)\}>0$, so that we can assert that graphene is a lossy material. Finally, we want to mention that for graphene characteristic sizes larger than λ_{F},

the inclusion of nonlocal effects does not induce significant changes with respect to the local limit, and qualitatively similar results are observed [31].

The employed lifetime or relaxation time $\tau = \gamma^{-1}$ of Fig. 1.5 is obtained using the impurity-limited approximation $\tau = \mu E_{\mathrm{F}}/ev_{\mathrm{F}}^2$, where μ is the direct current (dc) graphene electrical mobility [see section (1.3.4)]. For instance, in Fig. 1.5(b) we use the parameters $E_{\mathrm{F}} = 0.4\,\mathrm{eV}$ and $\mu = 10000\,\mathrm{cm}^2/(\mathrm{V\,s})$, thus the predicted lifetime in graphene is $\tau \approx 400\,\mathrm{fs}$ (*i.e.*, $\hbar\gamma \approx 1.65\,\mathrm{meV}$). This value is substantially higher than $\tau \approx 10\,\mathrm{fs}$ in gold [39]. In all the figures depicted in this introductory chapter, the damping rate is calculated using this dc procedure.

1.4.2 Quantum-mechanical description: Random-phase approximation

The local classical descriptions of the electromagnetic response of graphene to external radiation presented in the previous section are no longer valid when the size of the graphene nanostructure D fulfills $D \lesssim \lambda_{\mathrm{F}}$. Hence, a microscopic quantum-mechanical procedure that takes also into account finite-size and edge effects, is necessary to characterize the optoelectronic response of graphene. In this thesis, we combine the RPA with a TB model similar to the one described in the section (1.3.2) [see Ref. [40] for a detailed description of the method used here]. However, in our case we only consider the hopping between nearest neighbors l and l', so that the TB Hamiltonian satisfies $\langle l|\, H\, |l'\rangle = -t$ with the already known hopping parameter $t \sim 2.8\,\mathrm{eV}$. The diagonalization of this Hamiltonian permits finding the energy ϵ_j of each single-electron state j. Once this is done, we are interested in finding the non-interacting susceptibility $\chi^0_{ll'}(\omega)$ using the RPA. This quantity relates the induced charge density $\rho^{\mathrm{ind}}_l(\omega)$ with the total potential per unit area resulting from the sum of the external and induced potentials $\Phi_l(\omega) = \Phi^{\mathrm{ext}}_l(\omega) + \Phi^{\mathrm{ind}}_l(\omega)$ as

$$\rho^{\mathrm{ind}}_l(\omega) = \sum\nolimits_{l'} \chi^0_{ll'}(\omega)\, \Phi_{l'}(\omega)\,, \tag{1.19}$$

where l and l' run over the carbon sites of the graphene structure [41]. For simplicity, we have just considered the non-interacting susceptibility between electrons, otherwise finding a solution requires the use of many-body theory. By means of the

expansion coefficients a_{jl} of each TB state $\sum_l a_{jl}\,|l\rangle$, the non-interacting susceptibility yields

$$\chi^0_{ll'}(\omega) = -2e^2 \sum\nolimits_{jj'} \left(f_{\epsilon_j} - f_{\epsilon_{j'}}\right) \frac{a_{jl}\, a^*_{jl'}\, a^*_{j'l}\, a_{j'l'}}{\hbar\omega - \epsilon_j + \epsilon_{j'} + \mathrm{i}\hbar/2\tau}, \tag{1.20}$$

where $\hbar\omega$ is the energy of the incident photon, τ is the finite lifetime of the electronic excitations, and

$$f_{\epsilon_j} = \frac{1}{1 + \mathrm{e}^{(\epsilon_j - E_\mathrm{F})/k_\mathrm{B}T}} \tag{1.21}$$

is the Fermi-Dirac electron distribution of the state j at Fermi energy E_F and temperature T. The factor 2 immediately after the equal sign in Eq. (1.20) stems from the spin degeneracy. Additionally, the total potential per unit area can be also expressed as

$$\Phi_l(\omega) = \Phi^{\mathrm{ext}}_l(\omega) + \sum\nolimits_{l'} v_{ll'}(\omega)\, \rho^{\mathrm{ind}}_{l'}(\omega), \tag{1.22}$$

where $v_{ll'}(\omega) = 1/r_{ll'}$ is the Coulomb interaction between sites l and l'. Finally, combining Eqs. (1.19) and (1.22), we can get a self-consistent solution of the induced charge density given by

$$\rho^{\mathrm{ind}}(\omega) = \left[1 - \chi^0(\omega)\cdot v(\omega)\right]^{-1} \cdot \chi^0(\omega) \cdot \Phi^{\mathrm{ext}}(\omega), \tag{1.23}$$

from which we can directly obtain the induced dipole moment [see section (1.5.3)] and the electric polarizability $\alpha(\omega)$. A detailed study of the effects regarding this quantum-mechanical approach is fully illustrated for different graphene geometries in Chapters 3 and 4.

1.5 Plasmons in graphene

Graphene plasmons are collective surface oscillations of electrons with respect to the fixed positively-charged lattice of carbon nuclei. The oscillation occurs because the attractive binding exerted by the lattice is weak, so that electrons can move freely forming an electronic cloud reacting to external radiation. Plasmons sustained by graphene are generically divided into two different groups: intrinsic and extrinsic plasmons. The former are observable under any doping conditions –even in pristine graphene– and can be subdivided into two different subgroups: σ and π plasmons.

The latter, also named Dirac plasmons, only appear when graphene is extrinsically doped.

In the next section, we briefly introduce the main properties of intrinsic graphene plasmons. Their extremely high resonance frequencies ($\gtrsim 4.5\,\mathrm{eV}$) are in contrast to the suitable ones of Dirac plasmons ($\lesssim 3\,\mathrm{eV}$) which make them more interesting for nanophotonics opening a wide range of potential applications. Afterwards, we explain the main properties of these Dirac plasmons but always assuming a classical description for graphene.

1.5.1 σ AND π PLASMONS

These plasmons arise respectively from the collective oscillation in the 2D plane of delocalized σ and π electrons [see section (1.3.2)]. They were first observed in fullerene [42, 43], and later in CNTs [44, 45] and extended graphene [46] via electron energy loss spectroscopy (EELS). This technique has been extensively employed for spectrally and spatially characterizing diverse plasmons in noble metals [47, 48, 49, 50, 51] and graphene [52, 53, 54]. Essentially, in EELS an electron beam passes near or through a plasmonic target and the electrons lose part of their energy by exciting plasmons.

The resonance frequencies of π plasmons oscillate between 4.5 and 7 eV, while for σ plasmons the range fluctuates from 14.5 to 30 eV, which confine both deeply in the UV regime. Moreover, they display a limited tunability, similarly to those in typical noble metals. Finally, we need to remark that at electron energies $\sim 5\,\mathrm{eV}$, vertical interband transitions between the π and π^* bands can occur for wave vectors situated between the Dirac points [see Fig. 1.3(b)]. The resulting possible coupling of this mechanism with the π plasmon is known as plexciton [55]. In the rest of this thesis, we do not discuss these plasmons any more.

1.5.2 DIRAC PLASMONS

As explained in section (1.3.2), pristine graphene presents a peculiar linear dispersion relation around the Dirac points with a zero-energy optical gap between the completely filled valence band and the fully empty conduction band (*i.e.*, pristine graphene can be treated as a zero-gap semiconductor). Within these conditions, the

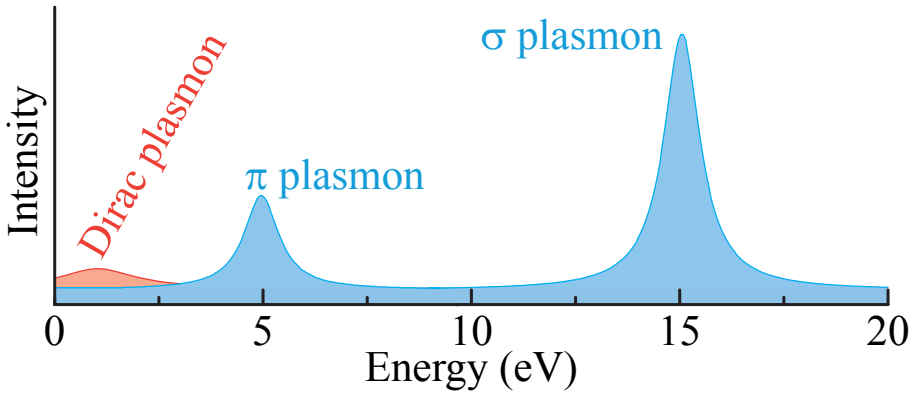

Figure 1.6: Schematic representation of the different plasmons sustained by graphene. The blue region corresponds to the plasmons excited in pristine graphene, where we can distinguish between the π plasmons at energies $\sim 5\,\text{eV}$, and the σ plasmons at $\sim 15\,\text{eV}$. For doped graphene, a new type of low-energy plasmons appear (red region), the so-called Dirac plasmons with energy $\lesssim 3\,\text{eV}$.

Dirac points mark exactly the Fermi level [see Fig. 1.3(b)]. Besides, the only possible e-h excitation when graphene is illuminated under this null doping condition is an interband transition. These transitions are responsible for a nearly-constant absorption [30] of self-standing undoped extended graphene [56, 57] $\pi\alpha \approx 2.3\%$ (*i.e.*, conductivity $\sigma_0 = e^2/4\hbar$ [31]), where $\alpha = e^2/\hbar c \approx 1/137.036$ is the fine-structure constant.

When we add extra charge carriers (electrons) to the conduction band (*i.e.*, n-doped graphene), an optical gap opens and the Fermi energy substantially shifts to $E_\text{F} = \hbar v_\text{F}\sqrt{\pi n}$, where now n is the density of these extra electrons [see Fig. 1.8(a) for an illustrative representation of the variation of E_F with the external doping]. Due to the symmetry of the bands, the doping can be also produced by the removal of valence electrons (*i.e.*, p-doped graphene), so that the Dirac massless particles responsible for the doping are now the holes in the valence band. The remarkable tunability of the Fermi level in graphene with the addition of external carriers is in contrast to the response of typical noble metals, which is rather unaffected by doping. Moreover, noble metals present a parabolic dispersion of their conduction band that electrons fill up to a certain level determined by E_F, and there is no optical gap so that electrons below the Fermi level can move up to any of the unoccupied

states above E_{F}. However, significant changes in the electronic carrier density n in metals will only slightly affect their optoelectronic response. Furthermore, in metals n is expressed per unit of volume while in graphene it is per unit of area, so that a bigger quantity of electrons is required for inducing significant changes in E_{F}.

Experimentally, the injection of additional charge carriers (either electrons or holes) is usually achieved by electrostatic gating [58, 59] or with chemical methods [60, 61]. Within the former, a potential difference with respect to a backgate is applied to graphene, thus inducing a perpendicular dc electric field $\mathbf{E}_0$ that is uniformly applied to one side of the carbon layer and screened by an induced doping charge carrier density $n = -E_0/4\pi e$. Fermi levels as high as $\sim 1\,\mathrm{eV}$ have been obtained using this technique [58, 59], which correspond to $n \sim 75 \times 10^{12}\,\mathrm{cm}^{-2}$.

Moreover, when light impinges on doped graphene, electrons from the conduction band can be excited up to unoccupied states. This can occur through the absorption of the energy and momentum of incident photons. Therefore, in addition to interband e-h transitions [*i.e.*, the green and blue arrows in Fig. 1.8(a)], intraband e-h transition are also allowed [*i.e.*, the magenta arrow in Fig. 1.8(a)].

Within the opening of an optical gap of maximum width $2E_{\mathrm{F}}$, apart from the e-h transitions, doped graphene can support surface plasmons without undergoing Landau damping [62]. These are the Dirac plasmons mentioned above –collective oscillations of the conduction electrons (or holes)– whose resonance frequency fall between the THz and the near infrared region (NIR) [35, 63, 64, 65, 66, 67, 68, 69, 70, 71, 72, 73]. Graphene Dirac plasmons present an impressive number of salient properties in comparison with those in typical noble metals: (i) stronger interaction with light; (ii) ability of producing a large field enhancement [26, 31] ($> 10^5$ in near-field intensities) upon external illumination; (iii) smaller wavelength in comparison to the external radiation which results in an extraordinary light and field confinement; (iv) longer lifetimes [38, 74]; and (v) stronger nonlinearities [75, 76, 77, 78, 79, 80, 81]. Furthermore, the spectral and spatial control via electrical gating over these collective oscillations have been intensively investigated in recent years both experimentally [64, 65, 66, 67, 68, 69, 71, 82, 83] and theoretically [31, 34, 35, 38, 30, 81, 84, 85, 86, 87, 88, 89, 90]. Owing to the former appealing properties, graphene Dirac plasmons can be currently found in a vast range of applications: light modulation [69, 71, 91], nonlinear optics [75, 76, 77, 78, 81], sensing [92, 93],

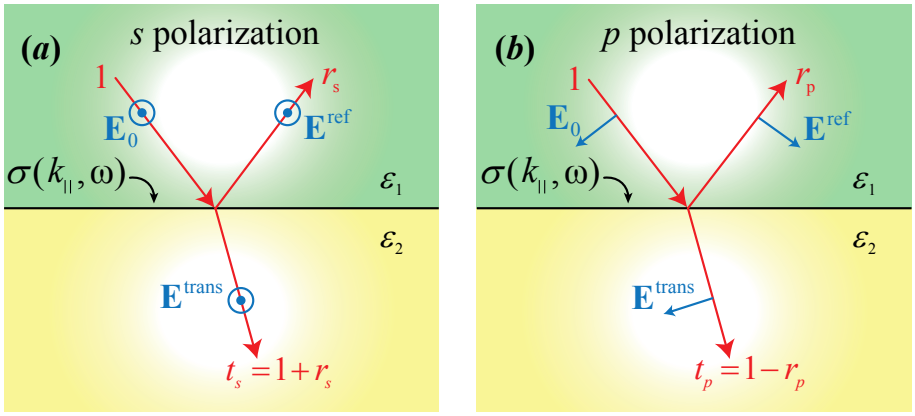

Figure 1.7: Reflection and transmission coefficients of impinging (a) s polarized and (b) p polarized waves by a thin graphene layer. The graphene layer is characterized by its conductivity $\sigma(k_{\|},\omega)$ and acts as an interface between two different media with dielectric functions ε_1 and ε_2, respectively. The orientations of the incident ($\mathbf{E}_0$), reflected ($\mathbf{E}^{\text{ref}}$), and transmitted ($\mathbf{E}^{\text{trans}}$) electric fields are depicted within blue arrows.

and signal processing [63], among other feats.

We focus now on the two different subgroups of Dirac plasmons sustained by doped graphene which we distinguish according to their propagating features: surface plasmon polaritons and localized surface plasmons.

Surface plasmon polaritons in graphene

The surface plasmon polaritons (SPPs) are electromagnetic modes traveling along an extended graphene layer acting as an interface between two dielectric media. They are transverse solutions [*i.e.*, $\nabla \cdot \mathbf{E}(\mathbf{r},\omega) = 0$] of the macroscopic Maxwell's equations described in Eq. (1.11) in the absence of external sources, and fulfill the condition of non-zero magnetic field in both surrounding dielectric media and graphene.

Once the graphene interface –which we assume in the limit of a thin layer– is illuminated by a plane wave, we can easily obtain the relations between the reflected and transmitted electric fields at the interface through the Fresnel coefficients [26]. The expressions of these coefficients depend on the two different types of electromagnetic field polarizations. For s polarization [*i.e.*, TE modes: the incident light impinging from medium 1 is polarized with its electric field perpendicular to the

plane of incidence as shown in Fig. 1.7(a)], we get

$$r_s = \frac{k_{1\perp} - k_{2\perp} - \frac{4\pi\sigma}{c}k}{k_{1\perp} + k_{2\perp} + \frac{4\pi\sigma}{c}k}, \qquad t_s = 1 + r_s, \tag{1.24}$$

where $\sigma(k_\parallel, \omega)$ is the graphene conductivity and $k_{j\perp}$ is the free-space light wave vector component oriented perpendicularly to the graphene layer in the dielectric medium $j = 1, 2$ (above or below graphene, respectively). The wave vector in each dielectric medium evolves as $k_j = \sqrt{\varepsilon_j}k$ and it can be split into its components as $k_j = \sqrt{k_\parallel^2 + k_{j\perp}^2}$, where the parallel wave vector component $k_\parallel$ is equal in both media. The interesting point of this TE mode is that, unlike metal-dielectric interfaces, graphene can sustain it [94] but only when $\mathrm{Im}\{\sigma(\omega)\}<0$ [*i.e.*, for low levels of doping, $2E_\mathrm{F} \lesssim \hbar\omega$, as depicted in the inset of Fig. 1.5(a)].

For p polarization [*i.e.*, TM modes: the incident light is polarized with the associated electric field parallel to the incidence plane as shown in Fig. 1.7(b)] we have

$$r_p = \frac{\varepsilon_2 k_{1\perp} - \varepsilon_1 k_{2\perp} + \frac{4\pi\sigma}{\omega}k_{1\perp}k_{2\perp}}{\varepsilon_2 k_{1\perp} + \varepsilon_1 k_{2\perp} + \frac{4\pi\sigma}{\omega}k_{1\perp}k_{2\perp}}, \qquad t_p = 1 - r_p, \tag{1.25}$$

where now the surface mode only propagates under the condition of $\mathrm{Im}\{\sigma(\omega)\}>0$ [*i.e.*, for high levels of doping, $2E_\mathrm{F} \gtrsim \hbar\omega$, as depicted in the inset of Fig. 1.5(a)]. The dispersion relation of the p polarized graphene SPPs is obtained through the pole of r_p, which satisfies the equation

$$\frac{\varepsilon_1}{\sqrt{k_\mathrm{spp}^2 - \varepsilon_1 k^2}} + \frac{\varepsilon_2}{\sqrt{k_\mathrm{spp}^2 - \varepsilon_2 k^2}} = -\frac{4\pi\mathrm{i}\sigma}{\omega}, \tag{1.26}$$

for the in-plane component of the plasmon wave vector k_spp. In Fig. 1.8(b) we plot the self-consistent solution of $\mathrm{Im}\{r_p\}$ for self-standing (*i.e.*, $\varepsilon_1 = \varepsilon_2 = 1$) extended graphene with $E_\mathrm{F} = 0.4\,\mathrm{eV}$ and $\mu = 10000\,\mathrm{cm}^2/(\mathrm{V\,s})$. Here, the graphene conductivity is taken from the full (nonlocal) RPA model [see supplementary material (SM) of Ref. [31]]. As we can observe, for $k_\parallel < k_\mathrm{F}$ and $\hbar\omega < 2E_\mathrm{F}$, an optical gap opens, and a propagating mode along the surface arises (*i.e.*, the SPP). Thus, a distinct absorption feature is generated apart from the intraband and interband e-h transitions (lower and upper orange triangles on the right side).

Interestingly, in the electrostatic limit the light wave vector –depicted within a

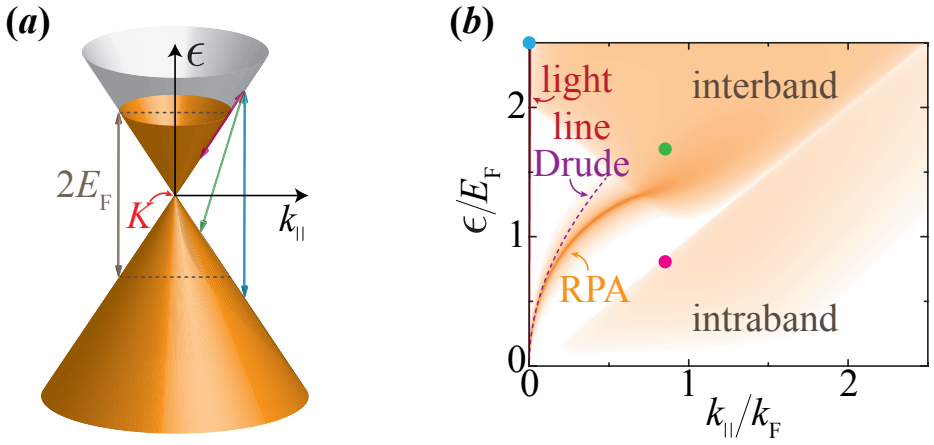

Figure 1.8: Dispersion relation of graphene. (a) Optical dispersion diagram of graphene with the typical linear behavior [*i.e.*, zoom around the Dirac point K in Fig. 1.3(a)]. For doped graphene the lower band (valence band) is completely filled, and the upper band (conduction band) is partially filled with conduction electrons up to a certain level with respect to K, thus marking the Fermi energy E_F. We also represent here three different possible e-h excitations: intraband (magenta dot) and interband (green and blue dots) transitions. (b) Density plot representing the dispersion relation of self-standing extended graphene with the possible intraband and interband transitions of electrons including the three cases depicted in panel (a). We observe an optical gap (white triangle on the left at parallel wave vector smaller that the Fermi wave vector, *i.e.*, $k_\parallel < k_\mathrm{F}$), where graphene SPPs can be sustained. We represent here the $\mathrm{Im}\{r_p\}$ as a function of $k_\parallel$ and ω, using the RPA model at temperature $T = 300\,\mathrm{K}$ for $E_\mathrm{F} = \hbar v_\mathrm{F} k_\mathrm{F} = 0.4\,\mathrm{eV}$ and mobility $\mu = 10000\,\mathrm{cm}^2/(\mathrm{V\,s})$, where $v_\mathrm{F} \approx c/300$ is the Fermi velocity. The dispersion of the plasmons obtained from the Drude model is plotted within the purple dashed curve. The light line is represented in red and in close proximity to the vertical axis.

red line in close proximity to the left vertical axis– fulfills the condition $k \ll |k_{\rm spp}|$ (in reality, this is fulfilled for $\hbar\omega \gg \alpha E_{\rm F}$), so that Eq. (1.26) can be expressed as

$$k_{\rm spp}(k_{\parallel},\omega) \approx \frac{(\varepsilon_1+\varepsilon_2)}{2}\frac{{\rm i}\omega}{2\pi\sigma(k_{\parallel},\omega)}. \tag{1.27}$$

Due to the momentum mismatch between light and SPP, we immediately claim that SPPs cannot be directly excited with light (*i.e.*, they are dark modes with non-radiative nature), and overcoming this problem becomes a challenge [see section (2.4)].

For completeness, we represent within the purple dashed curve the dispersion relation of SPPs following the Drude model [see Eq. (1.16)]. Here, the plasmon wave vector reduces to $k_{\rm spp}^{\rm Drude}(\omega) \approx [(\varepsilon_1+\varepsilon_2)/2]\,\hbar^2\omega\,(\omega+{\rm i}\gamma)/2e^2E_{\rm F}$, clearly showing a quadratic dependence on the frequency. Since $\lambda_{\rm spp} = 2\pi/{\rm Re}\{k_{\rm spp}\}$, we can directly obtain the ratio between the SPP and the free-space-light wavelengths

$$\frac{\lambda_{\rm spp}^{\rm Drude}}{\lambda} \approx \frac{2}{(\varepsilon_1+\varepsilon_2)}\frac{2\alpha E_{\rm F}}{\hbar\omega}, \tag{1.28}$$

which illustrates the high degree of confinement of graphene SPPs.

On the other hand ${\rm Im}\{k_{\rm spp}\}$, which strongly depends on γ, accounts for the damping of the SPPs as they propagate along graphene. For a decay of 1/e in the plasmon intensity, the longitudinal propagated length of the plasmon is $L_{\parallel} \approx 1/\,2{\rm Im}\{k_{\rm spp}\}$. Additionally, the perpendicular wave vector component is $\sim {\rm i}k_{\rm spp}$, so that it presents a dominant imaginary part which turns into a tighter confinement of the field in the transverse direction of the graphene layer. Specifically, the transversal plasmon intensity decays exponentially with $L_{\perp} \approx 1/\,2{\rm Re}\{k_{\rm spp}\} \ll L_{\parallel}$ (although rigorously, when $\varepsilon_1 > \varepsilon_2$ we have $L_{1\perp} < L_{2\perp} \ll L_{\parallel}$). The balance of both properties: the degree of confinement and the propagation length, is an inherent problem when dealing with graphene SPPs.

Localized surface plasmons in graphene

The second fundamental plasmon excitation in doped graphene are the localized surface plasmons (LSPs), which are collective charge oscillations confined in finite

nanostructures with characteristic size D (*e.g.*, triangles, ribbons, disks, etc.) Unlike SPPs, these plasmons can be directly excited by external plane waves, thus contributing to multiple absorption and scattering mechanisms. However, due to the lack of translational invariance, they are constrained to the two dimensions of the graphene nanostructures (*i.e.*, they are localized or non-propagating waves [28]).

We start by taking macroscopic Maxwell's equations from Eq. (1.11) and after assuming negligible the external currents and charges, the first two expressions remain

$$\begin{aligned} \nabla \times \nabla \times \mathbf{E}(\mathbf{r},\omega) - \varepsilon(\omega) k^2 \mathbf{E}(\mathbf{r},\omega) = 0, \\ \nabla \times \varepsilon^{-1}(\omega) \nabla \times \mathbf{H}(\mathbf{r},\omega) - k^2 \mathbf{H}(\mathbf{r},\omega) = 0. \end{aligned} \tag{1.29}$$

Implementing the convenient boundary conditions for each arbitrary graphene geometry, it is possible to get an analytical full-retarded solution of Eq. (1.29). Nevertheless, as mention in section (1.4.1), even for the simplest nanostructures, finding a solution involves huge numerical calculations. Thus, if we assume that the size of the nanostructure is much smaller than the wavelength of the incident radiation, we can safely work in the electrostatic limit and the problem simplifies to just solving the Poisson equation given in Eq. (1.13).

Like SPPs supported in extended graphene, LSPs also present interesting properties such as strong field enhancement, a high degree of confinement, and a low level of losses in comparison to those in typical noble metals. Besides, as we will show below, graphene LSPs highly depend on the size and shape of the supporting particle. Slight variations of these geometrical parameters induce remarkable shifts in the plasmon frequencies that are strongly tunable with the level of doping. Moreover, LSPs permit boosting light-matter interactions up to levels where the effective plasmonic area can be higher than the proper geometric area of the nanostructure.

The existence of the LSPs is easily demonstrated through the scattering and absorption light processes produced in the graphene nanostructures. In fact, the most common way of quantifying them is via the scattering and absorption cross-sections, which are directly derived from the optical theorem [26]

$$\sigma^{\mathrm{sc}}(\omega) = \frac{8\pi\omega^4}{3c^4} \left|\alpha(\omega)\right|^2, \qquad \sigma^{\mathrm{abs}}(\omega) = \frac{4\pi\omega}{c} \operatorname{Im}\{\alpha(\omega)\} - \sigma^{\mathrm{sc}}(\omega). \tag{1.30}$$

The sum of these variables is known as the extinction cross-section $\sigma^{\rm ext}(\omega)$. Interestingly, for sufficiently small particles, absorption dominates over scattering since the former scales with D^3, and the latter with D^6 [28].

In Fig. 1.9 we represent the lowest-order dipolar LSP excited in a graphene nanodisk under normal illumination. The panel (a) shows the absorption and scattering cross-sections of an illuminated disk of 30 nm in diameter embedded in vacuum (see upper right inset). The Fermi level, thickness, and mobility of the disk are $E_{\rm F} = 0.4\,{\rm eV}$, $t = 0.5\,{\rm nm}$, and $\mu = 10000\,{\rm cm}^2/({\rm V\,s})$, respectively. We compare the solution of Maxwell's equations (solid curves) with the electrostatic approach (dashed curves). As we can observe, the models are in excellent agreement. Besides, we also compare the results from the two different local models for the dielectric function of the graphene disk studied in this thesis: the Drude (blue curves), and the local-RPA model at room temperature $T = 300\,{\rm K}$ (red curves) [see Eqs. (1.16) and (1.18), respectively]. We observe that the different approaches give similar results but, again, the inclusion of the temperature and the interband transitions result in slight redshifts of the LSP resonance frequencies.

The curves of the cross-sections were numerically obtained through BEM calculations and present a Lorentzian lineshape centered at the LSP resonance frequency $\omega_{\rm p}$, and its broadening presents a spectral FWHM given by the damping rate γ [26]. Moreover, the plasmon quality factor ($Q = \omega_{\rm p}/\gamma$) reaches here for the Drude model a value $\gtrsim 150$, which is remarkably higher than in typical noble metals. Finally, we observe that the absorption cross-section reaches ~ 7 times the geometric area of the disk, which turns graphene into a perfect tool for the confinement of light at the nanoscale. In panel (b) we plot the induced near-field intensity enhancement ($|\mathbf{E}/\mathbf{E}_0|^2$) produced in the vicinity of the disk at the LSP frequency of the red solid curve ($\hbar\omega_{\rm p} \approx 0.262\,{\rm eV}$). The huge value induced close to the surface (~ 1000) illustrates the importance of LSPs for the enhancement of electromagnetic fields. The white arrows indicate the orientation of the electric field. As we observe, the induced electric field created inside the disk is capable of screening the external field, and the metallic behavior is preserved.

Finally, it is also interesting to know the number of charge carriers (conduction electrons or holes) responsible for the LSPs. This quantity can be estimated via the f-sum rule [32, 95], which in graphene possesses singular properties [96]. In the

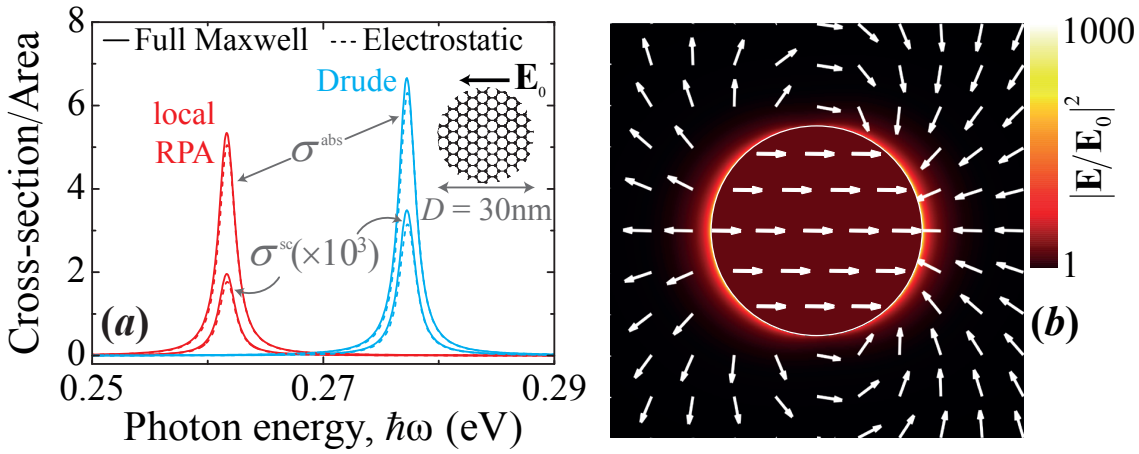

Figure 1.9: Localized surface plasmons (LSPs) excited in a graphene nanodisk by the effect of an electric field ($\mathbf{E}_0$) associated with external light impinging perpendicularly to the graphene area. (a) We plot the absorption ($\sigma^{\rm abs}$) and scattering ($\sigma^{\rm sc}$) cross-sections as a function of the incident photon energy of a self-standing graphene nanodisk with diameter $D = 30\,\text{nm}$, Fermi level $E_{\rm F} = 0.4\,\text{eV}$, thickness $t = 0.5\,\text{nm}$, and mobility $\mu = 10000\,\text{cm}^2/(\text{V s})$ (see inset). The dielectric function of the graphene disk is described by two different models: the local-RPA at temperature $T = 300\,\text{K}$ (red curves) and the Drude model (blue curves). The cross-sections are normalized to the disk area ($\pi D^2/4$). We compare the results from the solution of full-retarded Maxwell's equations (solid curves) with the electrostatic approach (dashed curves). The multiplying factor in the scattering cross-section indicates that the depicted curves in reality should be divided by 10^3 (we use this procedure only for aesthetic reasons). (b) Induced near-field intensity enhancement ($|\mathbf{E}/\mathbf{E}_0|^2$) plotted in linear scale at the LSP frequency corresponding to the LSP resonance of the red solid curve (*i.e.*, $\hbar\omega_{\rm p} \approx 0.262\,\text{eV}$). The white arrows represent the orientation of the induced electric field. All the results are calculated using the boundary-element method (BEM) through the MNPBEM toolbox [97].

electrostatic limit, it presents the form [30]

$$\int_0^\infty \omega\,\mathrm{d}\omega\,\mathrm{Im}\{\alpha(\omega)\} = \frac{\pi e^2}{2m_e^*}N_e, \tag{1.31}$$

with N_e being the number of charge carriers in the graphene nanostructure and m_e^* the cyclotron mass given in Eq. (1.9). Fortunately, since the most intense LSPs appear at low energies, we can shorten the range of frequencies inside the integral.

1.5.3 Optical losses

Once excited, plasmons in graphene possess a finite lifetime γ^{-1} before they dissipate either through radiative or non-radiative (inelastic) channels. The former are related with re-emission of photons [98], while the latter are associated with other path-ways [99] like coupling with phonons [38], collision with lattice defects [100], finite-size and edge effects [40, 101], or generation of hot e-h pairs [102]. Thus, we can split the decay rate into a radiative and non-radiative components as $\gamma = \gamma_{\rm r} + \gamma_{\rm nr}$. The radiative contribution is usually a factor $\sim 10^3$ smaller and is given by [98]

$$\hbar\gamma_{\rm r}(\omega) = \sqrt{\frac{(\varepsilon_1 + \varepsilon_2)}{2}}\,\frac{4\omega^3}{3c^3}\,|\mathbf{p}(\omega)|^2, \tag{1.32}$$

where $\mathbf{p}(\omega) = \int \rho^{\rm ind}(\mathbf{R},\omega)\,\mathbf{R}\,{\rm d}^2\mathbf{R}$ is the dipole moment associated with the graphene layer, and $\varepsilon_1|\varepsilon_2$ the permittivities above|below graphene, respectively.

Regarding the non-radiative decay channels, the coupling with phonons plays an important role above the threshold energy $\sim 0.2\,$eV [38, 70]. Moreover, the edge effects also induce a remarkable increment of the damping due to the creation of electronic edge states [20]. There are two different types of edge terminations in the graphene nanostructures: *armchair* or *zigzag* [see right inset of Fig. 3.1]. The electronic edge states are only present in zigzag terminations [20] and produce a strong plasmon quenching [40] when $\hbar\omega_{\rm p} \gtrsim E_{\rm F}$ [101]. Under the same energy condition, for the armchair terminations the edge effects only induce a slight broadening of the plasmons [89, 101]. Finally, the decay of plasmons into e-h pairs because of Landau damping may occur when additional momentum is provided, and the plasmons fall inside the region of electronic interband transitions [see Fig. 1.8(b)].

1.5.4 Electrostatic scaling law

In previous sections we have showed that for graphene nanostructures of size D (*e.g.*, width of ribbons, diameter of disks, lateral size of equilateral triangles...) much smaller than the incident light wavelength, retardation effects can be neglected and we can safely work in the electrostatic limit. Thus, we can study the response of graphene in terms of an electrostatic potential $\Phi(\mathbf{r},\omega)$. The self-consistent equation

of this potential created by a certain bidimensional charge density acting as an interface between two dielectric media with permittivities[2] ε_1 and ε_2 is [53]

$$\Phi(\mathbf{r},\omega) = \Phi^{\text{ext}}(\mathbf{r},\omega) + \frac{2}{(\varepsilon_1+\varepsilon_2)}\int \frac{\mathrm{d}^2\mathbf{R}'}{|\mathbf{r}-\mathbf{R}'|}\rho^{\text{ind}}(\mathbf{R}',\omega). \tag{1.33}$$

This expression is valid for any point $\mathbf{r} = (\mathbf{R}, z)$, but since we restrict our analysis to the graphene sheet which lies in the plane $z = 0$, the self-consistent potential will only involve coordinate vectors $\mathbf{R} = (x, y)$. The expression of Eq. (1.33) is the sum of two contributions: the external perturbation [now rewritten as $\Phi^{\text{ext}}(\mathbf{R},\omega)$], and the potential created by the charge induced in doped graphene under external illumination which is globally represented by the integral. We can relate this induced charge with the current by means of the continuity equation given in Eq. (1.14). Furthermore, if we assume a linear response of graphene, the current can be obtained from the multiplication of the local, in-plane graphene conductivity $\sigma(\mathbf{R},\omega)$ by the total electric field $\mathbf{E}(\mathbf{R},\omega)$. Combining all the former elements, we can rearrange the self-consistent equation of the potential to obtain

$$\Phi(\mathbf{R},\omega) = \Phi^{\text{ext}}(\mathbf{R},\omega) + \frac{2}{(\varepsilon_1+\varepsilon_2)}\frac{\mathrm{i}}{\omega}\int \frac{\mathrm{d}^2\mathbf{R}'}{|\mathbf{R}-\mathbf{R}'|}\nabla_{\mathbf{R}'}\cdot\sigma(\mathbf{R}',\omega)\nabla_{\mathbf{R}'}\Phi(\mathbf{R}',\omega). \tag{1.34}$$

We need to remark that the abrupt change of the conductivity produced at the edge of the nanostructure produces a divergent contribution to the integral of Eq. (1.34). The numerical solution of this issue involves the implementation of a smoothing at the graphene edge [an example is described in section (2.3)] that barely affects the final result [90].

Owing to the complete lack of absolute length scales in electrostatics, we can introduce for simplicity the dimensionless coordinate vector $\vec{\theta} = \mathbf{R}/D$. Besides, we consider that the conductivity can be split into a position and a frequency dependent terms as $\sigma(\mathbf{R},\omega) = f(\mathbf{R})\sigma(\omega)$. Under uniform doping, the occupation function $f(\mathbf{R})$ takes the constant value 1 inside the graphene area and vanishes elsewhere. As we will see in the next chapter, this formalism can be easily applied to diverse inhomogeneous doping configurations by just modifying the spatial distribution of

[2] see Appendix A for the derivation of the factor $2/(\varepsilon_1+\varepsilon_2)$ regarding the dielectric environment

$f(\mathbf{R})$ [86, 90, 103]. Thus, implementing these elements in Eq. (1.34), we obtain

$$\Phi(\vec{\theta},\omega) = \Phi^{\text{ext}}(\vec{\theta},\omega) + \eta(\omega)\int \frac{\mathrm{d}^2\vec{\theta}'}{|\vec{\theta}-\vec{\theta}'|}\nabla_{\vec{\theta}'}\cdot f(\vec{\theta}')\nabla_{\vec{\theta}'}\Phi(\vec{\theta}',\omega), \tag{1.35}$$

where

$$\eta(\omega) = \frac{2}{(\varepsilon_1+\varepsilon_2)}\,\frac{\mathrm{i}\sigma(\omega)}{\omega D}, \tag{1.36}$$

is a dimensionless parameter that contains all the information about the full dependence of graphene on the frequency, temperature, size, dielectric environment, and doping level. Integrating by parts Eq. (1.35) and taking the in-plane gradient on both sides, we find

$$\vec{\mathcal{E}}(\vec{\theta},\omega) = \vec{\mathcal{E}}^{\text{ext}}(\vec{\theta},\omega) + \eta(\omega)\int \mathrm{d}^2\vec{\theta}'\,\mathbf{M}(\vec{\theta},\vec{\theta}')\cdot\vec{\mathcal{E}}(\vec{\theta}',\omega), \tag{1.37}$$

where

$$\vec{\mathcal{E}}(\vec{\theta},\omega) = \sqrt{f(\vec{\theta})}\,\mathbf{E}(\vec{\theta},\omega), \tag{1.38}$$

and $\mathbf{M}(\vec{\theta},\vec{\theta}') = \sqrt{f(\vec{\theta})f(\vec{\theta}')}\,\nabla_{\vec{\theta}}\otimes\nabla_{\vec{\theta}'}\left(1/|\vec{\theta}-\vec{\theta}'|\right)$ is a real and symmetric operator. This operator possesses a complete dimensionless set of real, negative eigenvalues $1/\eta_j$, and eigenvectors $\vec{\mathcal{E}}_j(\vec{\theta})$ that satisfy the eigenstate, orthogonality, and closure conditions given respectively by

$$\begin{aligned}
\eta_j\int \mathrm{d}^2\vec{\theta}'\,\mathbf{M}(\vec{\theta},\vec{\theta}')\cdot\vec{\mathcal{E}}_j(\vec{\theta}') &= \vec{\mathcal{E}}_j(\vec{\theta}),\\
\int \mathrm{d}^2\vec{\theta}\;\vec{\mathcal{E}}_j(\vec{\theta})\cdot\vec{\mathcal{E}}_{j'}(\vec{\theta}) &= \delta_{jj'},\\
\sum\nolimits_j \vec{\mathcal{E}}_j(\vec{\theta})\cdot\vec{\mathcal{E}}_j(\vec{\theta}') &= \delta(\vec{\theta}-\vec{\theta}')\mathcal{I}_2,
\end{aligned} \tag{1.39}$$

with $\mathcal{I}_2$ being the 2×2 unit matrix. Then, the solution to Eq. (1.37) can be transformed into

$$\vec{\mathcal{E}}(\vec{\theta},\omega) = \sum\nolimits_j \frac{c_j}{1-\eta(\omega)/\eta_j}\vec{\mathcal{E}}_j(\vec{\theta}), \tag{1.40}$$

where the expansion coefficients

$$c_j = \int \mathrm{d}^2\vec{\theta}\;\vec{\mathcal{E}}_j(\vec{\theta})\cdot\vec{\mathcal{E}}^{\text{ext}}(\vec{\theta},\omega) \tag{1.41}$$

hold the same units as the electric field. If we assume normal-incidence illumination (*i.e.*, $k_{\parallel} = 0$) with an associated external field uniformly distributed with amplitude $\mathbf{E}_0$ and oriented along the direction $\hat{\mathbf{x}}$ of the nanostructure [*i.e.*, $\vec{\mathcal{E}}^{\rm ext}(\vec{\theta}) = \sqrt{f(\vec{\theta})}E_0\,\hat{\mathbf{x}}$], we can get the expression of the polarizability along that direction $\alpha(\omega) = (D^3/E_0)\int \mathrm{d}^2\vec{\theta}\;\theta_x\,\rho^{\rm ind}(\vec{\theta},\omega)$, where the induced density is

$$\rho^{\rm ind}(\vec{\theta},\omega) = -\frac{\mathrm{i}\sigma(\omega)}{\omega D}\left[\nabla_{\vec{\theta}}\cdot\sqrt{f(\vec{\theta})}\vec{\mathcal{E}}(\vec{\theta},\omega)\right]. \tag{1.42}$$

It is then convenient to insert Eq. (1.40) into this expression, then we finally find

$$\alpha(\omega) = \frac{(\varepsilon_1+\varepsilon_2)}{2}D^3\sum\nolimits_j \frac{\xi_j^2}{\frac{1}{\eta(\omega)}-\frac{1}{\eta_j}}, \tag{1.43}$$

where j runs over each eigenmode and

$$\xi_j^2 = \left|\int \mathrm{d}^2\vec{\theta}\sqrt{f(\vec{\theta})}\,\mathcal{E}_j(\theta_x)\right|^2, \tag{1.44}$$

are real, positive, and dimensionless coefficients that only depend on the specific shape of the nanostructure considered. Interestingly, for the Drude model we find $\alpha^{\rm Drude}(\omega) \propto D^{5/2}E_{\rm F}^{1/2}$.

The ξ_j and η_j factors obey two useful sum rules [30] that enable estimating analytically their values: (i) in the weak coupling regime (*i.e.*, $\sigma \to 0$) upon application of the closure relation for $\vec{\mathcal{E}}_j(\vec{\theta})$, we have

$$\sum\nolimits_j \xi_j^2 = \frac{A}{D^2}, \tag{1.45}$$

where A in the area of the graphene nanostructure; and (ii) in the limit of a perfect conductor (*i.e.*, $\sigma \to \infty$), we get

$$-\sum\nolimits_j \eta_j\xi_j^2 = \frac{2\,[\alpha(0)/D^3]}{(\varepsilon_1+\varepsilon_2)}. \tag{1.46}$$

In particular, for nanodisks we have [104] $\alpha(0)/D^3 = 1/6\pi$, while for nanoribbons we find [105] $\alpha(0)/D^3 = L/16D$ where $L \to \infty$ is the nanoribbon length. In Table 1.1 we summarize the analytical values of these factors for both nanostructures

Geometry	$-\sum_j \eta_j \xi_j^2$	$\sum_j \xi_j^2$	$\sum_j \eta_j$
disk	$[2/(\varepsilon_1+\varepsilon_2)]\,(1/6\pi)$	$\pi/4$	$[2/(\varepsilon_1+\varepsilon_2)]\,(-2/3\pi^2)$
ribbon	$[2/(\varepsilon_1+\varepsilon_2)]\,(1/16)$	1	$[2/(\varepsilon_1+\varepsilon_2)]\,(-1/16)$

Table 1.1: Analytical approximations for the parameters ξ_j and η_j of the electrostatic scaling law.

Interestingly, for the nanostructures here considered, one finds that the first mode $j = 1$ (*i.e.*, lowest-order dipolar mode) is dominant and owns most of the weight in the sums given in Eqs. (1.45) and (1.46) [30]. Additionally, we need to remark that the condition $\eta(\omega_j) = \eta_j$ sets the plasmon frequency ω_j of the corresponding eigenstate j. Since all the graphene properties are contained inside $\eta(\omega)$, these eigenvalues η_j only depend on the geometrical shape of the graphene nanostructure and can be calculated once and for all in order to get the plasmon frequencies for any desired value of the temperature, size, dielectric environment, or doping level. In particular, using the Drude model [see Eq. (1.16)], we easily obtain [see Appendix B]

$$\omega_{\mathrm{p}}^{\mathrm{Drude}} \approx \omega_j^{\mathrm{Drude}} - \mathrm{i}\gamma/2, \tag{1.47}$$

with

$$\omega_j^{\mathrm{Drude}} = \frac{e}{\hbar}\sqrt{\left[\frac{2}{\varepsilon_1+\varepsilon_2}\right]\left[\frac{1}{-\pi\eta_j}\right]\left[\frac{E_{\mathrm{F}}}{D}\right]}. \tag{1.48}$$

As an example, we take the conditions used in Fig. 1.9 of $E_{\mathrm{F}} = 0.4\,\mathrm{eV}$ and $D = 30\,\mathrm{nm}$ of a uniformly doped, self-standing nanodisk. If we assume dominant the lowest-order dipolar plasmon, we find that the estimated LSP energy is $\hbar\omega_1^{\mathrm{Drude}} \approx 0.3\,\mathrm{eV}$, which is in good agreement with the numerical solution of full-retarded Maxwell's equations depicted in Fig. 1.9(a).

The fact that the resonance frequencies of LSPs in graphene nanostructures obey the approximate behavior $\omega_{\mathrm{p}} \propto \sqrt{E_{\mathrm{F}}/D}$, illustrates their strong tunability and pave the way for plenty of potential applications to exploit the plasmonic properties of doped graphene.

Chapter 2

Plasmons in multiple doping configurations

In the previous chapter, we have presented a description of graphene plasmons sustained by extended layers or individual nanostructures under a uniform doping configuration. The plasmonic response of graphene under this doping scheme has been extensively described in the literature and plenty of potential applications have been developed up to date [30, 31, 63, 88].

It is well-known that Dirac plasmons arise in doped graphene with a resonance frequency proportional to $n^{1/4}$, where n is the doping charge carrier density. However, we find that usually n is not uniformly distributed, and therefore, its profile depends on the particular geometrical configuration which modifies the plasmonic response of graphene. Besides, the interaction of neighboring nanostructures can also produce remarkable differences in the Dirac plasmons developed on each single island.

Motivated by these facts, in this chapter we classically study the effects of different geometric, and inhomogeneous doping schemes exerted on LSPs (for convenience, during this chapter we will refer to them simply as "plasmons") and SPPs. Using extensively the electrostatic scaling law described in section (1.5.4), we specifically discuss the following topics:

– We start by analyzing the interaction between identical uniformly doped graph-

ene nanoribbons via a novel and easy-to-handle model based on the plasmon wave function (PWF) which presents a higher level of accuracy than other existing commonly-used models.

- Then, we describe the properties of plasmons generated under multiple inhomogeneous doping configurations. Firstly, we analyze the plasmons sustained on nanoribbons with diverse non-uniform distributions of n over the surface. Secondly, we concentrate on plasmons supported by individual inhomogeneously doped graphene nanodisks.
- Finally, we investigate SPPs created on periodically doped extended graphene which develop a plasmonic band structure.

2.1 Plasmons in interacting uniformly doped ribbons

In this section, we describe the plasmonic response of uniformly doped graphene nanoribbons of width D. We focus on this geometry due to the availability of new synthesis methods with control down to the nanometer scale [106, 107, 108, 109]. For our purpose, we analytically derive a model based on the PWF together with the electrostatic scaling law formalism presented in section (1.5.4). We conveniently define the PWF associated with the electromagnetic mode j as

$$\rho_j(\theta_x) = \frac{\partial}{\partial \theta_x}\sqrt{f(\theta_x)}\,\mathcal{E}_j(\theta_x), \tag{2.1}$$

where we have assumed that the nanoribbon is normally illuminated with the electric field polarized along the transversal direction $\hat{\mathbf{x}}$ with amplitude $\mathbf{E}_0$. In Fig. 2.1 we illustrate the interaction between two ribbons through the interaction of their PWFs. The ribbons are separated a center-to-center distance $\mathbf{r}$ and aligned along $\hat{\mathbf{y}}$ (*i.e.*, they can lie in different z planes) under the illumination conditions mentioned above. The impinging light induces a line dipole along $\hat{\mathbf{x}}$. The PWF profile at the plasmon frequency is also included displaying a uniform dipolar-like behavior along $\hat{\mathbf{y}}$.

Using the definition of the PWF given in Eq. (2.1), the expansion coefficients of

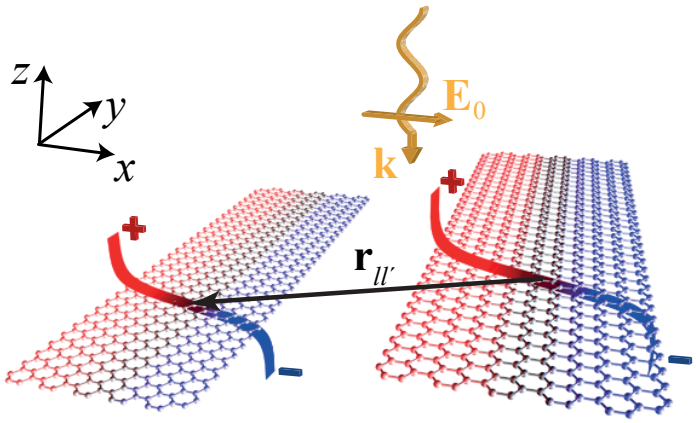

Figure 2.1: Plasmon wave functions (PWFs) of two interacting graphene nanoribbons aligned along $\hat{\mathbf{y}}$ under normal-incidence illumination. We represent the PWF associated with the lowest-order dipolar mode of two graphene nanoribbons separated by a vector $\mathbf{r}_{ll'}$ and excited by a normal-incidence plane wave of transverse polarization. The shape of the PWF is obtained from the induced charge density at the frequency of this lowest-order plasmon (ρ_1) and clearly shows a dipolar-like behavior going from positive (red color) to negative (blue color) values along the transversal direction of the ribbons. The figure is adapted from Ref. [110].

Eq. (1.41) can be now expressed as $c_j = -E_0\,\xi_j$, whereas the dimensionless coefficients of Eq. (1.44) remain

$$\xi_j^2 = \left| \int \mathrm{d}\theta_x\, \theta_x\, \rho_j(\theta_x) \right|^2 . \tag{2.2}$$

Remarkably, the PWF is proportional to the induced charge density of the plasmon mode j, whereas ξ_j can be treated as the normalized dipole moment. Moreover, the PWF also fulfills the charge neutrality condition $\int \mathrm{d}\theta_x\, \rho_j(\theta_x) = 0$.

For simplicity, we study the response of identical ribbons within a spectral region dominated by their lowest-order transversal dipole mode ($j = 1$), neglecting other modes in what follows. Besides, we intentionally discard the x subindex since we know that the geometric evolution of the PWF varies along the $\hat{\mathbf{x}}$ direction. Thus, we can express $\mathcal{E}(\theta, \omega)$ in terms of this lowest-order mode as

$$\mathcal{E}(\theta, \omega) = \sum\nolimits_l d_l(\omega)\, \mathcal{E}_1(\theta - \theta_l), \tag{2.3}$$

where l runs over each different ribbon, and θ_l indicates the position of the central point of the nanoribbon. Inserting Eq. (2.3) into Eq. (1.37), and using the eigenstate and orthogonality conditions given in Eq. (1.39), we find the self-consistent equation

$$d_l(\omega) = \frac{1}{1-\eta(\omega)/\eta_1}\Big[- E_0\,\xi_1 + \eta(\omega)\sum\nolimits_{l'\neq l} \mathbf{M}_{ll'}(\theta,\theta')\,d_{l'}(\omega)\Big], \tag{2.4}$$

for the expansion coefficients, where

$$\begin{aligned}\mathbf{M}_{ll'}(\theta,\theta') &= \int \mathrm{d}\theta \int \mathrm{d}\theta'\ \mathcal{E}_1(\theta-\theta_l)\mathbf{M}(\theta,\theta')\mathcal{E}_{l'}(\theta'-\theta_{l'}) \\ &= \int \mathrm{d}\theta \int \mathrm{d}\theta'\ \rho_1(\theta)\rho_1(\theta')\ \ln\left[(\theta-\theta'+\theta_l-\theta_{l'})^2+(z_l-z_{l'})^2/W^2\right],\end{aligned} \tag{2.5}$$

describes the interaction between ribbons l and l'. Notice that we have generalized $\mathbf{M}_{ll'}(\theta,\theta')$ in order to deal with ribbons that are located at different heights z_l.

Considering now the expression of the induced charge density given in Eq. (1.42), we can easily find the dipole moment induced in ribbon l

$$p_l(\omega) = -\eta(\omega)D^2L\,d_l(\omega)\xi_1. \tag{2.6}$$

Taking into account that the self-consistent interaction between the dipoles of different ribbons is [104]

$$p_l(\omega) = \alpha(\omega)E_0 + \alpha(\omega)\sum\nolimits_{l'\neq l}\mathcal{G}_{ll'}\,p_{l'}(\omega), \tag{2.7}$$

where we identify

$$\mathcal{G}_{ll'} = \left[\frac{1}{D^2L\xi_1^2}\right]\mathbf{M}_{ll'}(\theta,\theta') = \frac{-\left[2/(\varepsilon_1+\varepsilon_2)\right]}{p_1^2(\omega)}\int \mathrm{d}^2\mathbf{R}\int \mathrm{d}^2\mathbf{R}'\,\frac{\rho_1(\mathbf{R})\rho_1(\mathbf{R}')}{|\mathbf{R}-\mathbf{R}'-\mathbf{r}_{ll'}|} \tag{2.8}$$

as the Green tensor [26, 111] for the electric field produced by a single dipole, which contains all the information about the interaction between nanoribbons. As we can observe, it is directly related with the PWF which is well approximated by the phenomenological analytical function [110]

$$\rho_1(\theta) \approx 9\theta\left\{1+\frac{\mathrm{e}^{-5+20\theta^2}}{4\sqrt{1-4\theta^2}}\right\}. \tag{2.9}$$

Moreover, $\mathbf{p}_1(\omega)$ is the dipole moment at the plasmon frequency, and $\alpha(\omega) = [(\varepsilon_1+\varepsilon_2)/2]\, D^2 L \xi_1^2 / [1/\eta(\omega) - 1/\eta_1]$ is the individual nanoribbon polarizability in the single-mode approximation that presents a similar expression to Eq. (1.43). Remarkably, from our calculations we get that the fitting coefficients are $\eta_1 \approx -0.069$ and $\xi_1 \approx 0.94$, which are in good agreement with the purely analytical values predicted in section (1.5.4) $\sum_j \eta_j = -1/16 \approx -0.063$ and $\sum_j \xi_j^2 = 1$.

If we take now into account that the extinction cross-section is the sum of the expressions given in Eq. (1.30), for a system formed by interacting ribbons we get

$$\sigma^{\rm ext}(\omega) = \frac{4\pi\omega}{c} \sum\nolimits_{ll'} {\rm Im} \left\{ \frac{1}{1/\alpha(\omega) - \mathcal{G}} \Big|_{ll'} \right\}, \tag{2.10}$$

where $\mathcal{G}$ is a matrix of elements $(1-\delta_{ll'})\, \mathcal{G}_{ll'}$. Note that since we assume symmetry along the longitudinal direction of the nanoribbon with length $L \to \infty$, we in fact implement in Eq. (2.10) the polarizability per unit length $\alpha(\omega)/L$ and $\mathcal{G}L$, so that the resulting extinction cross-section in also given per unit length.

We depict in Fig. 2.2 the extinction cross-section normalized to the nanoribbon area of two interacting self-standing graphene nanoribbons ($l = 1, 2$). The dielectric response of the carbon layer is taken from the local-RPA model at temperature $T = 300\,{\rm K}$ [see Eq. (1.18)], where $E_{\rm F} = 0.4\,{\rm eV}$ is the Fermi level and $\hbar\gamma = 20\,{\rm meV}$ is the decay rate. The system displays a prominent dipolar plasmon that starts at the single-ribbon energy limit, corresponding to large separations between nanoribbons (blue curves) and undergoes dramatic redshifts (blueshifts) due to inter-ribbon attractive (repulsive) interaction in co-planar (stacked) arrangements, as illustrated in panel (a) [panel (b)]. The attractive (repulsive) character of this interaction is intuitively suggested from the induced charge distribution shown in Fig. 2.1. We find that the results from the PWF model (dashed curves) agree well with the full numerical solution (solid curves) down to very small edge-to-edge separations. In contrast, the dipole-dipole model (dotted curves) only produces accurate results at large separations, and its failure at small distances is particularly severe for stacked ribbons. This dipole-dipole model treats each ribbon as a line dipole along the transversal direction [30], and thus, the plasmon of the system results from the interaction between different dipoles that are oriented parallel to the external radiation.

In Fig. 2.3 we plot the evolution of the plasmon frequency for interacting rib-

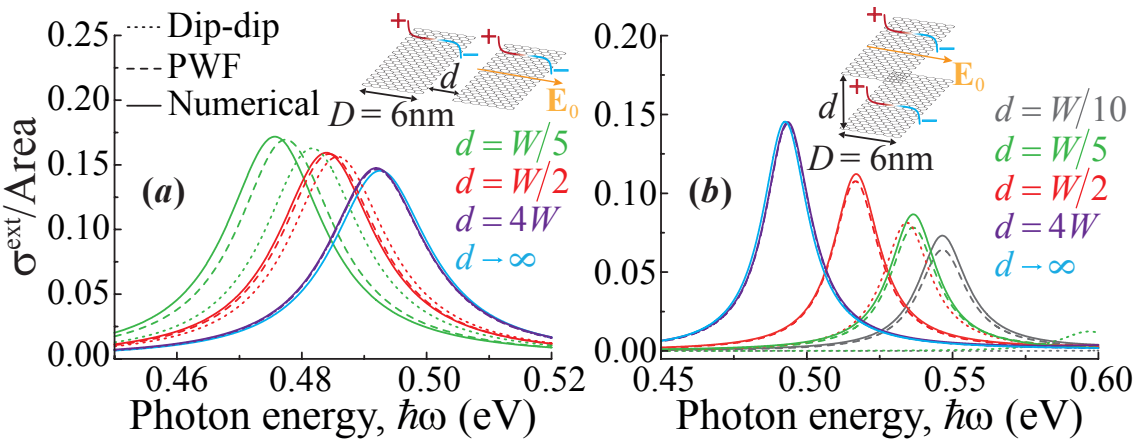

Figure 2.2: Extinction cross-section normalized to the total graphene area of dimers formed by self-standing graphene nanoribbons. The edge-to-edge distance is d for coplanar (a) and vertically-aligned (b) configurations. The ribbon width is $D = 6\,\mathrm{nm}$, while the Fermi energy and damping are $E_\mathrm{F} = 0.4\,\mathrm{eV}$, and $\hbar\gamma = 20\,\mathrm{meV}$, respectively. The conductivity of graphene is obtained from the local-RPA model at temperature $T = 300\,\mathrm{K}$ [see Eq. (1.18)]. The solid curves correspond to the numerical solutions of full-retarded macroscopic Maxwell's equations, directly calculated using BEM [see section (1.4)]. The PWF calculations are represented by dashed curves while the analytical dipole-dipole interaction is plotted with dotted curves. The figure is adapted from Ref. [110].

bons over a more extended spatial range. The red curves correspond to the ribbon dimers presented in Fig. 2.2, whereas the green curves correspond to an infinite periodic array of ribbons. The plasmon modes are calculated here from the condition $\mathrm{Re}\{1/\alpha(\omega) - \mathcal{G}\} = 0$. As we can observe, the frequency shifts are larger in the array than in dimers due to the inter-ribbon interactions. Remarkably, the results from our PWF model are in excellent agreement with numerical calculations even at very short edge-to-edge distances, especially in the stacked system as represented in Fig. 2.3(b). For the periodic array, we have assumed that Eq. (2.7) can be analytically solved by summing $G = \sum_{l\neq 0} \mathcal{G}_{0l} \mathrm{e}^{\mathrm{i}k_\parallel a l}$, where a is the period of the array and $k_\parallel$ is the wave vector component along the array direction. In the case of the green curves displayed in Fig. 2.3, since the incidence of light is normal, we have $k_\parallel = 0$, and therefore, $G = \sum_{l\neq 0} \mathcal{G}_{0l}$.

Furthermore, within the PWF model for long distances between the ribbons,

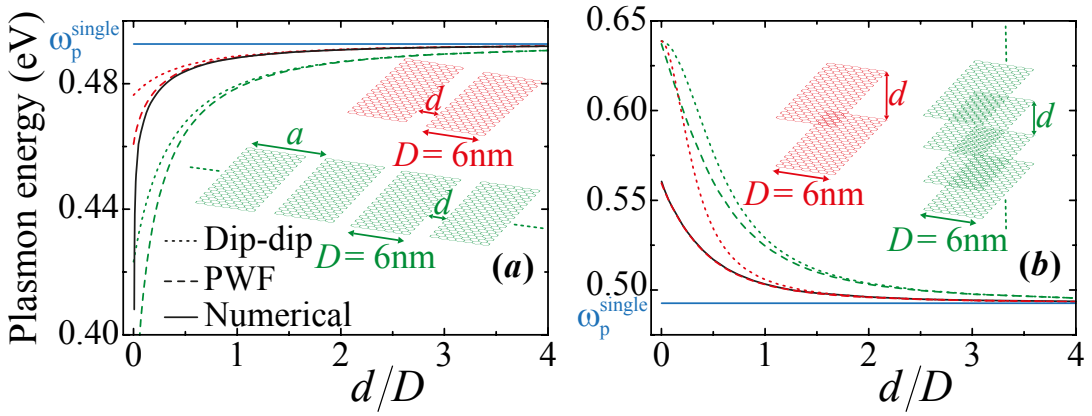

Figure 2.3: Plasmon energy of interacting graphene nanoribbons in different dimer and array configurations. (a) We plot the evolution of the plasmon energies with the edge-to-edge separation d in co-planar ribbon dimers (red curves) and infinite periodic arrays (green curves). The black solid curve corresponds to the full numerical solution of the Maxwell's equations for the dimers [see section (1.4)]. The dielectric response of the graphene ribbons, whereas their doping and damping parameters are the same as in Fig. 2.2. (b) Same as panel (a) for vertically offset nanoribbons. The figure is adapted from Ref. [110].

we recover the values from the dipole-dipole model. In this long-distance limit (*i.e.*, large $r_{ll'}$ compared with the ribbon width), we can expand the Coulomb interaction described by the logarithm function of Eq. (2.5), which leads to the well-known expression for the dipole-dipole interaction

$$\mathcal{G}_{ll'}^{\rm dip} \approx \frac{2}{(\varepsilon_1+\varepsilon_2)}\left\{\frac{3x_l x_{l'}}{r_{ll'}^5}-\frac{1}{r_{ll'}^3}\right\} \approx \frac{2}{(\varepsilon_1+\varepsilon_2)}\,\frac{2}{L}\,\frac{(z_l-z_{l'})^2-(x_l-x_{l'})^2}{[(z_l-z_{l'})^2+(x_l-x_{l'})^2]^2}. \quad (2.11)$$

Here, for co-planar and vertically stacked dimers separated by a center-to-center distance a, we have $\mathcal{G}_{12}^{\rm dip} = [2/(\varepsilon_1+\varepsilon_2)]\,2/La^2$ and $-[2/(\varepsilon_1+\varepsilon_2)]\,2/La^2$, respectively. For periodic arrays of co-planar ribbons and period $a = (D+d) \ll \lambda$ (*i.e.*, there is no diffraction), we have $x_l = la$ and $z_l = 0$, leading to $\mathcal{G}_{0l}^{\rm dip} = [2/(\varepsilon_1+\varepsilon_2)]\,2/L(la)^2$, so that $G^{\rm dip} = [2/(\varepsilon_1+\varepsilon_2)]\,g/La^2$, with $g = 2\pi^2/3 \approx 6.58$. Likewise, for vertically stacked ribbons of period $a = d$ (*i.e.*, $x_l = 0$ and $z_l = la$), we find $G^{\rm dip}$ to be exactly the value of the co-planar array but with opposite sign. For completeness, in the cases of 2D co-planar hexagonal and square arrays when $\lambda \gtrsim 50a$, we find $g \approx 5.52$

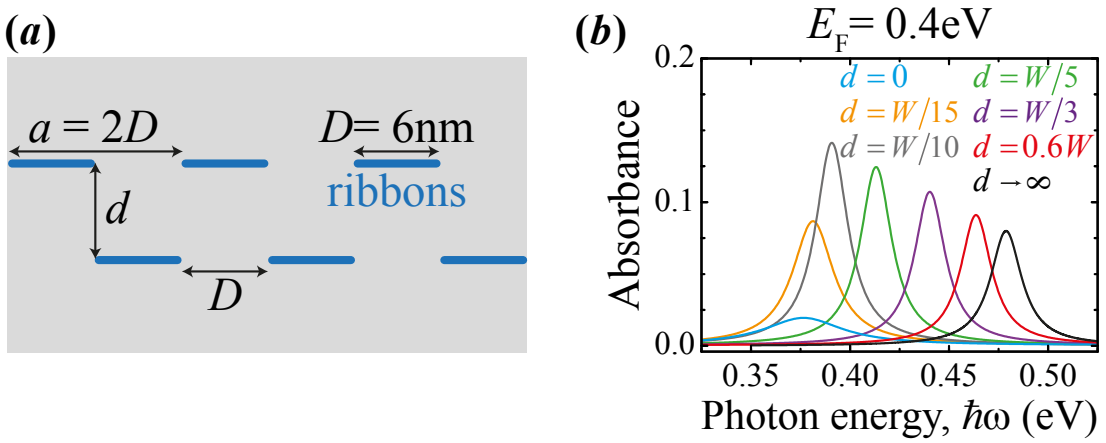

Figure 2.4: Absorbance of a bilayer array with a lateral offset obtained from the PWF model. (a) Sketch of the geometry under consideration where, for simplicity, the interlayer distance d in the only variable parameter. (b) Normal-incidence absorbance (s polarization) for several values of d. The dielectric response, doping, and damping of the self-standing graphene nanoribbons are the same as in Fig. 2.2. The figure is adapted from Ref. [110].

and $g \approx 4.52$, respectively [88].

Finally, the versatility of our PWF model also permits us to calculate the absorbance of the periodic co-planar array of nanoribbons depicted in green in the inset of Fig. 2.3(a), or even more complicated systems. The expressions of the reflection and transmission Fresnel coefficients in the dipole-dipole limit of an infinite periodic array of co-planar ribbons acting as a $\varepsilon_1|\varepsilon_2$ interface for incident light incoming from medium 1 are given by [88]

$$\begin{aligned} \widetilde{r}_s &= r_s + \frac{\mathrm{i}S_s(1+r_s)}{\alpha^{-1} - G - \mathrm{i}S_s + 2\mathrm{i}k^3/3}, \qquad \widetilde{t}_s = 1 + \widetilde{r}_s, \\ \widetilde{r}_p &= r_p - \frac{\mathrm{i}S_p(1-r_p)}{\alpha^{-1} - G - \mathrm{i}S_p + 2\mathrm{i}k^3/3}, \qquad \widetilde{t}_p = 1 - \widetilde{r}_p, \end{aligned} \tag{2.12}$$

where the subindex stay for s and p polarizations of the incoming light, respectively. Besides, the Fresnel coefficients r_s, t_p, r_p, and t_p of individual graphene nanoribbons are described in Eqs. (1.24) and (1.25), and the $-\mathrm{i}S_{s,p} + 2\mathrm{i}k^3/3$ factors in the denominators stay for the radiative damping [88]. Moreover,

$$S_s = \frac{4\pi}{aL}\frac{k^2}{k_{1\perp}+k_{2\perp}},$$
$$S_p = \frac{4\pi}{aL}\frac{k_{1\perp}k_{2\perp}}{\varepsilon_2 k_{1\perp}+\varepsilon_1 k_{2\perp}}, \tag{2.13}$$

where $k_{j\perp}$ are the perpendicular components of the wave vector in the media $j = 1, 2$ as described in section (1.5.2). Combining all the former equations, we get the expression of the absorbance of the thin-layer array remains [112]

$$\mathcal{A}_{s,p} = 1 - |\widetilde{r}_{s,p}|^2 - \sqrt{\frac{\varepsilon_2}{\varepsilon_1}}\,|\widetilde{t}_{s,p}|^2. \tag{2.14}$$

Interestingly, for the conditions here assumed (self-standing layers and normal-incidence light), the maximum possible absorbance is 50%. However, a suitable combination of the surrounding dielectric media and angle of incidence of the external light permits achieving complete optical absorption (100%) [88]. Full absorption can further be achieved by placing the structure approximately a quarter wavelength away from a good mirror (Salisbury screen configuration [113, 114]).

As an illustrative example, we calculate the absorbance of two neighboring layers of graphene ribbon arrays with a lateral offset as depicted in Fig. 2.4(a). We assume that the ribbons are self-standing and normally illuminated with s polarized light (see Fig. 9 in Ref. [30]). Besides, we only vary the distance d between both layers and we consider that the reflection coefficient of the global system is the sum of the two independent layers. The spectra depicted in Fig. 2.4(b) are dominated by a single plasmon feature that is redshifted with decreasing interlayer distance due to attractive interaction similar to the dimers described in Fig. 2.2(a). Interestingly, when $d = 0$ we recover the extended graphene layer limit and the resulting absorbance is approximately the value given in section (1.5.2) $\pi\alpha \approx 2.3\%$. Note that, since our bilayer array is doped with a finite Fermi energy, here at the plasmon frequency the absorbance is slightly smaller than that 2.3% value. This is due to the opening of a gap of size $E_{\rm F}$ between the Dirac points and the first unoccupied state in the conduction band so that the e-h pairs creation is energetically less favorable.

2.2 Plasmons in inhomogeneously doped nanoribbons

In this section, we concentrate on the study of the plasmonic response of inhomogeneously doped self-standing graphene nanoribbons. Here, the spatial distribution of the doping charge carrier density n is obtained via an electrostatic boundary-element calculation. We particularly focus on three different realistic geometrical configurations: (i) backgated ribbons, (ii) co-planar ribbon pairs placed at opposite potentials, and (iii) individual ribbons subject to a uniform electric field.

2.2.1 Backgated nanoribbons

The first studied case consists of a nanoribbon of width D at a potential V relative to a planar backgate at a distance d [see Fig. 2.5(a)]. Although the induced charge density distribution $-en(x)$ over the structure surface $0 < x < D$ has been already reported in the past [115, 116, 117, 118], it can be analytically obtained using the method of charge images [111]. Within this approach, the problem reduces to solving a system formed by two parallel nanoribbons vertically separated by a distance $2d$ and placed at potentials $+V$ (the upper one) and $-V$ (the lower one), so that the backgate plane ($z = 0$) is at zero potential. The lower nanoribbon is thus represented by a induced charge density $en(x)$. Thereby, the potential at position x in the upper nanoribbon is

$$V = \int_0^D \mathrm{d}x' \int_{-\infty}^{+\infty} \mathrm{d}y \, [-en(x')] \left[\frac{1}{\sqrt{(x-x')^2 + y^2}} - \frac{1}{\sqrt{(x-x')^2 + y^2 + 4d^2}} \right]. \tag{2.15}$$

Calculating analytically this integral along the y coordinate and using the notation $\kappa = D/d$, $\theta = x/d$, with

$$u = -V/ed, \tag{2.16}$$

we can rewrite Eq. (2.15) as

$$u = \int_0^\kappa \mathrm{d}\theta' \, n(\theta' d) \, F(\theta, \theta'), \tag{2.17}$$

where

$$F(\theta,\theta') = \ln\left[1+\frac{4}{(\theta-\theta')^2}\right]. \tag{2.18}$$

We solve this integral equation by discretizing θ through a set of N equally spaced points $\theta_i = (i+1/2)\kappa/N$, with $i = 0,\ldots,N-1$. Thus, Eq. (2.17) can be approximated as

$$u \approx \sum\nolimits_{i'} n(\theta_{i'}d)\, M_{ii'}, \tag{2.19}$$

with

$$M_{ii'} = \int_{\theta_{i'}-\kappa/2N}^{\theta_{i'}+\kappa/2N} \mathrm{d}\theta'\, F(\theta_i,\theta') \tag{2.20}$$

being an integral over the interval surrounding point $\theta_{i'}$. Finally, the distribution of the doping charge carrier density is found by inverting the matrix M, so that

$$n(\theta_i d) = u \sum\nolimits_{i'} \left[M^{-1}\right]_{ii'}. \tag{2.21}$$

In practice, this method converges for $N \sim 100$. Interestingly, all the curves depicted in Figs. 2.5(b),(c) consist of two different curves with $N = 100$ and $N = 500$, and the difference is negligible on the scale of the plot. Interestingly, notice that the uniform doping charge carrier density in the $D/d \gg 1$ limit is given by $n^\infty = -V/4\pi ed$. Thus, we can obtain the expression of the average Fermi energy $\langle|E_\mathrm{F}|\rangle$ normalized to the value in the $D/d \gg 1$ limit $E_\mathrm{F}^\infty = \hbar v_\mathrm{F}\sqrt{|V|/4ed}$

$$\frac{\langle|E_\mathrm{F}|\rangle}{E_\mathrm{F}^\infty} \approx \frac{1}{N}\sum\nolimits_i \sqrt{4\pi|n(\theta_i d)/u|}. \tag{2.22}$$

Incidentally, we consider the absolute value of E_F because the graphene response is nearly insensitive to the sign of E_F.

Once we know the spatial distribution of the Fermi energy, we can use the electrostatic scaling law formalism presented in section (1.5.4) since $D \ll \lambda$, where λ is the wavelength of the incident light. We assume that the Fermi energy can be split as $E_\mathrm{F}(\mathbf{R}) = \langle|E_\mathrm{F}|\rangle f(\mathbf{R})$, where now the occupation function $f(\mathbf{R})$ is not uniform along the nanoribbon surface. Furthermore, the conductivity of the graphene structure in taken from the Drude model [see Eq. (1.16)]. We solve the self-consistent electrostatic equation given in Eq. (1.34) by describing the graphene nanoribbon as a square

periodic array of surface dipoles with a small period a compared to the characteristic lengths of the structure, *i.e.*, $a = D/\left(N^{\mathrm{dip}} - 1\right)$, where N^{dip} is the number of dipoles across $\hat{\mathbf{x}}$. This formalism is known as discrete surface-dipole approximation (DSDA) [88], where we take the polarizability of each dipole such that the layer formed by a uniform lattice of dipoles has the same conductivity as a uniform layer of graphene. The sum over dipole elements along $\hat{\mathbf{y}}$ is performed before a self-consistent solution is found, and therefore, the numerical problem reduces to solving a set of $2N^{\mathrm{dip}}$ linear equations with $2N^{\mathrm{dip}}$ variables (the dipole components along both $\hat{\mathbf{x}}$ and $\hat{\mathbf{y}}$ directions). In practice, convergence is achieved with a few hundred dipoles for the dimensions considered in this work. Here, we have modified this method by allowing each element to depend through E_{F} on the spatial position along $\hat{\mathbf{x}}$. Finally, we just need to solve a linear eigensystem [86] that produces real eigenvalues η'_j (here the subindex j refers to each eigenstate). Thus, using a similar formalism presented in Eq. (1.47), we express the plasmon frequencies as $\omega_{\mathrm{p}}^{\mathrm{Drude}} \approx \omega'_0/\sqrt{-\eta'_j} - \mathrm{i}\gamma/2$, where $\omega'_0 = (e/\hbar)\sqrt{\langle|E_{\mathrm{F}}|\rangle/D}$ defines a natural normalization frequency that we define for convenience.

We show in Fig. 2.5(b) the evolution of the average Fermi energy of the backgated nanoribbon normalized to E_{F}^{∞} as a function of the width-to-distance ratio D/d. In the limit $D \gg d$, which corresponds to the graphene nanostructure in close proximity to the backgate, $\langle|E_{\mathrm{F}}|\rangle$ converges smoothly to E_{F}^{∞}. Besides, from the inset we observe that the spatial distribution of the Fermi energy is nearly uniform except in the edges where a sharp profile appears. In contrast, in the limit $D \ll d$, which corresponds to large separations between the nanoribbon and the backgate, the profile is determined by the interaction of the nanoribbon with a distant image. Remarkably, in this limit we find that $\langle|E_{\mathrm{F}}|\rangle/E_{\mathrm{F}}^{\infty} \propto \sqrt{(d/D)}/\sqrt{\ln(d/D)}$, and from the inset, we observe that the shape of the Fermi level is smooth and convergent. Finally, we find that the doping level diverges as $\propto x^{-1/4}$ with the distance to the nanoribbon edge x.

In Fig. 2.5(c) we plot the plasmon frequencies of the system $\omega_{\mathrm{p}}^{\mathrm{Drude}}$, normalized to ω'_0, so that the ratio $\omega_{\mathrm{p}}^{\mathrm{Drude}}/\omega'_0$ is a dimensionless number, independent of the specific width D or doping level $\langle|E_{\mathrm{F}}|\rangle$. As an example, for $D = 100\,\mathrm{nm}$ and $\langle|E_{\mathrm{F}}|\rangle = 0.6\,\mathrm{eV}$, we find $\hbar\omega'_0 = 0.093\,\mathrm{eV}$ and a dipolar plasmon energy when $d = 10\,\mu\mathrm{m}$ of $\omega_{\mathrm{p}}^{\mathrm{Drude}} \approx 0.19\,\mathrm{eV}$ (*i.e.*, $\lambda_{\mathrm{p}}^{\mathrm{Drude}} \approx 6.5\,\mu\mathrm{m}$). As we can observe from the solid curves, with this

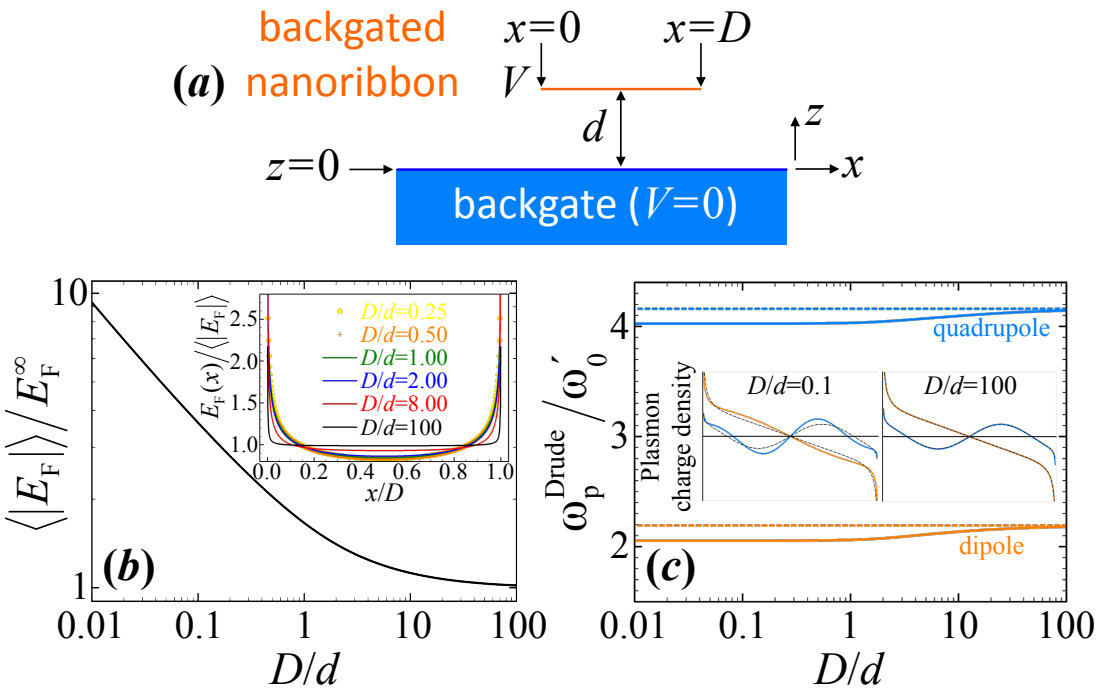

Figure 2.5: Inhomogeneous electrostatic doping and plasmon modes of backgated graphene nanoribbons. (a) Sketch of the geometry under consideration where a single nanoribbon of width D is placed at a potential V over a backgate. The distance between the graphene and the backgate is d. (b) Average Fermi energy $\langle|E_F|\rangle$ as a function of width-to-distance ratio D/d, normalized to the value $E_F^\infty = \hbar v_F\sqrt{|V|/4ed}$ obtained in the $D \gg d$ limit. The inset illustrates the E_F distribution along the nanoribbon, normalized to $\langle|E_F|\rangle$. (c) Frequency ω_p^{Drude} of the dipolar (orange curves) and quadrupolar (blue curves) plasmon modes, normalized to $\omega_0' = (e/\hbar)\sqrt{\langle|E_F|\rangle/D}$. The insets represent the induced charge density at the frequency of these plasmons (vertical axis) as a function of position across the nanoribbon (horizontal axis). The dashed curves indicate the $D \gg d$ limit. The figure is adapted from Ref. [86].

normalization $\omega_{\rm p}^{\rm Drude}/\omega_0'$ displays just a weak dependence on D/d for the dipolar and quadrupolar modes and is nearly constant when $D < d$. Moreover, the plasmon frequencies slightly differ from the ones corresponding to the uniform doping (dashed curves).

The inset of Fig. 2.5(c) shows the corresponding induced charge densities of the dipolar (orange curves) and quadrupolar (blue curves) modes for different D/d ratios, and obtained implementing the induced potential in Eq. (1.14) as $\rho^{\rm ind}(x,\omega) = [{\rm i}\sigma(\omega)/\omega]\nabla_x^2\Phi(x,\omega)$ via finite-difference derivation. We find that their profiles are only slightly affected by the change in doping profile relative to uniform doping (*i.e.*, the average level of doping is a dominant parameter, and the effect of edge divergences is only marginal). In conclusion, the plasmon frequencies and induced densities can be approximately described by assuming a uniform Fermi energy in backgated nanoribbons, thus supporting the validity of previous analyses for this configuration [31, 41, 85] although $\langle|E_{\rm F}|\rangle$ has to be appropriately scaled as plotted in Fig. 2.5(b) to compensate the effect of finite D/d ratios.

2.2.2 Co-planar nanoribbon pairs at opposite potentials

The second geometrical configuration here studied is illustrated in Fig. 2.6(a). It consists of two co-planar parallel nanoribbons of opposite polarity. The graphene nanostructures present the same width D and are separated by an edge-to-edge distance d. Here, the neighboring ribbons can act both as plasmonic structures and gates.

We follow the same analysis described in the previous section for the backgated case in order to get the spatial distribution of the Fermi energy. In our current case, the potential created on the nanoribbon on the right is

$$V = \int_{d/2}^{d/2+D} {\rm d}x' \int_{-\infty}^{+\infty} {\rm d}y\, [-en(x')] \left[\frac{1}{\sqrt{(x-x')^2+y^2}} - \frac{1}{\sqrt{(x+x')^2+y^2}} \right]. \quad (2.23)$$

Moreover, Eqs. (2.17) and (2.19)-(2.21) remain valid but Eq. (2.18) becomes

$$F(\theta,\theta') = 2\ln\left|\frac{\theta'+\theta}{\theta'-\theta}\right|. \quad (2.24)$$

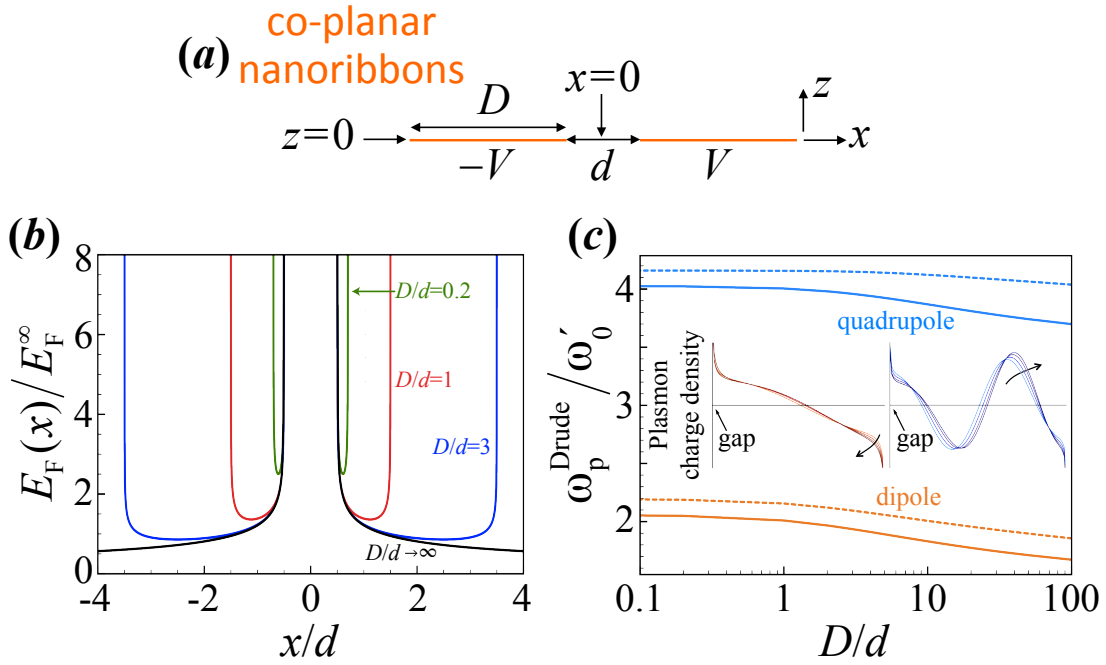

Figure 2.6: Inhomogeneous electrostatic doping and plasmon modes of co-planar parallel graphene nanoribbons of opposite polarity. (a) Sketch of the geometry under consideration with two co-planar parallel nanoribbons of width D, separated a distance d, and set at opposite potentials $-V$ and V, respectively. (b) Fermi energy distribution across the graphene surface for different width-to-distance D/d ratios. The Fermi energy $E_{\rm F}$ is normalized to the value $E_{\rm F}^{\infty} = \hbar v_{\rm F}\sqrt{|V|/4ed}$. (c) Frequency $\omega_{\rm p}^{\rm Drude}$ of the dipolar (orange curves) and quadrupolar (blue curves) plasmon modes, normalized to $\omega_0' = (e/\hbar)\sqrt{\langle|E_{\rm F}|\rangle/D}$, as obtained from the Drude model [see Eq. (1.16)]. The solid (dashed) curves correspond to inhomogeneous (uniform) doping. The insets illustrate the induced charge density associated with both plasmon modes (vertical axis) as a function of position across the nanoribbon on the right (horizontal axis, with the position of the right side of the gap indicated by an arrow) for $D/d = 0.2, 1, 3$, and 10, respectively (curves evolving in the direction of the cambered arrows). The figure is adapted from Ref. [86].

For symmetry, the density of doping charge carriers of the left nanoribbon is found as $n(x + d/2) = -n(-x - d/2)$. Finally, the plasmon frequencies with this specific spatial distribution of the doping are obtained using again the DSDA approach.

In Fig. 2.6(b) we depict the doping profiles across the nanoribbons, which evolve from a shape similar to the one obtained for the single nanostructure shown in the inset of Fig. 2.5(b) in the $D \ll d$ limit, towards a converged profile near the gap in the $D/d \to \infty$ limit. From Fig. 2.6(c) we observe that plasmons here greatly resemble those of neighboring uniformly doped nanoribbons for the same value of $\langle |E_{\mathrm{F}}| \rangle$. Incidentally, plasmons in pairs of uniform nanoribbons had already been thoroughly investigated [41], including the redshift with decreasing d.

2.2.3 Individual nanoribbons under a uniform electric field

The two inhomogeneous doping schemes considered so far for nanoribbons involve fabrication processes including contacts that allow to charge graphene electrically and could turn into structural defects. However, we can prevent these defects with an electrostatic doping through a uniform external electric field easily attainable experimentally by either distant gates or low-frequency radiation. For this reason, the last geometrical configuration studied here consists of a globally neutral nanoribbon exposed to an uniform external electric field $\mathbf{E}_0$ oriented along its width D [see Fig. 2.7(a)].

We follow the same procedure as in the two previous doping configurations in order to get the spatial distribution of the Fermi energy. If we take the nanoribbon to be placed at zero potential, we can write

$$0 = -E_0 x + \int_{-D/2}^{+D/2} \mathrm{d}x' \int_{-\infty}^{+\infty} \mathrm{d}y \, [-en(x')] \, \frac{1}{\sqrt{(x-x')^2 + y^2}}, \tag{2.25}$$

where the first term after the equal sign stays for the scalar potential produced by the external field. Now, using the normalization $\theta = x/D$, the above equation reduces to

$$E_0 \theta = \int_{-1/2}^{+1/2} \mathrm{d}\theta' \, [-en(\theta' d)] \, F(\theta, \theta'), \tag{2.26}$$

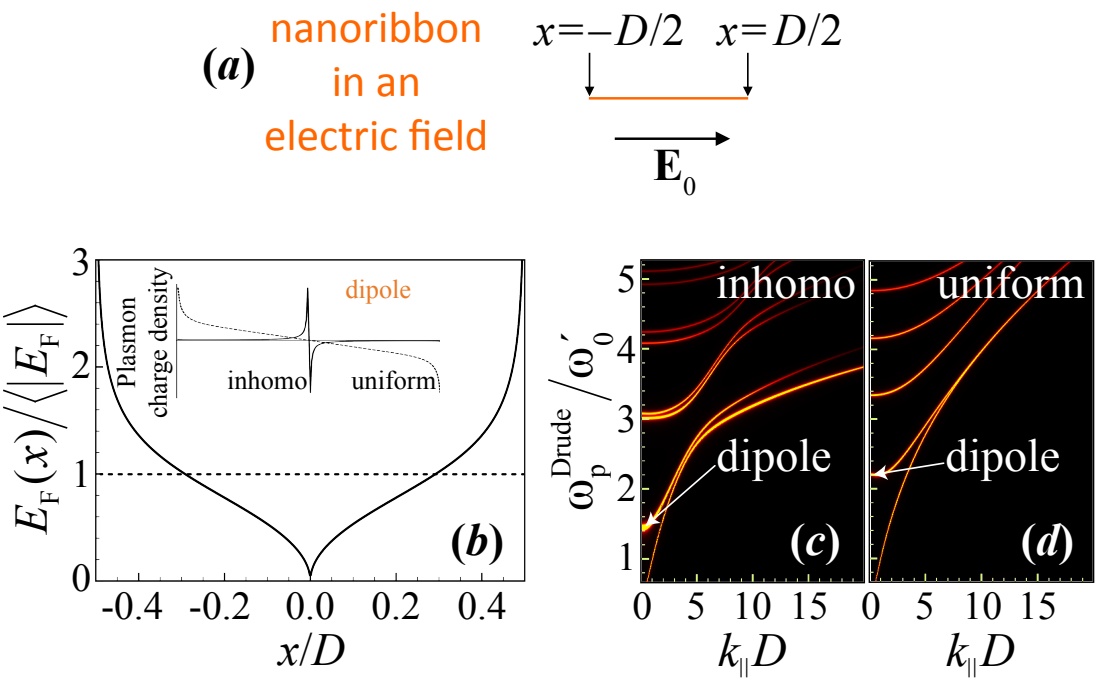

Figure 2.7: Inhomogeneous electrostatic doping and plasmon modes in individual graphene nanoribbons subject to a uniform external electric field $\mathbf{E}_0$. (a) Sketch of the geometry under consideration with a single nanoribbon of width D exposed to a uniform external electric field. (b) Fermi energy distribution normalized to $\langle|E_{\rm F}|\rangle = 0.6\hbar v_{\rm F}\sqrt{E_0/e}$ where the dashed line shows corresponds to the uniform doping case [*i.e.*, $E_{\rm F}(x) = \langle|E_{\rm F}|\rangle$]. The inset corresponds to the induced charge density associated with the dipolar plasmon mode excited when $k_\parallel = 0$ for inhomogeneous (solid curve) and uniform (dashed curve) doping conditions, respectively. Here, the plasmon frequency for inhomogeneous doping is $\omega_{\rm p}^{\rm Drude} \approx 1.45\,\omega_0'$, where $\omega_0' = (e/\hbar)\sqrt{\langle|E_{\rm F}|\rangle/D}$. (c) Plasmon dispersion diagram representing the dependence of the density of optical states on frequency $\omega_{\rm p}^{\rm Drude}$ and wave vector parallel to the nanoribbon $k_\parallel$. (d) Same as panel (c) for uniform doping. The figure is adapted from Ref. [86].

where

$$F(\theta,\theta') = -\ln\left[(\theta-\theta')^2\right]. \tag{2.27}$$

We use the discretization $\theta_i = -1/2 + (i+1/2)/N$ to write an expression similar to Eq. (2.19), where $M_{ii'}$ is still given by Eq. (2.20) with $\kappa = 1$. Finally, the density of doping charge carriers is obtained from

$$n(\theta_i d) = (-E_0/e)\sum\nolimits_{i'} \left[M^{-1}\right]_{ii'}\theta_{i'}. \tag{2.28}$$

We illustrate in Fig. 2.7(b) the spatial distribution of the Fermi energy $E_{\rm F}(x) = \hbar v_{\rm F}\sqrt{\pi|n(x)|}$ normalized to the average Fermi energy, which is found to be $\langle|E_{\rm F}|\rangle = 0.6\,\hbar v_{\rm F}\sqrt{E_0/e}$. We observe that the doping profile (solid curves) exhibits a divergence at the edges again, and it vanishes at the center of the nanoribbon, where n changes sign. The dashed line corresponds to the uniform doping. The resulting induced charge density of the dipolar plasmon for normal-incidence illumination ($k_\parallel = 0$) is plotted in the insets. For the inhomogeneous doping, it displays a large concentration of induced charges near the center of the ribbon, in contrast to the uniform doping case (dashed curve) that shows the typical dipolar-like behavior also observed in Fig. 2.1(a). This inhomogeneous induced dipole-charge density concentration results from the vanishing of n, which can be understood as a thinning of the effective layer thickness, similar to the trapping of graphene plasmons at p-n junctions [119].

Although we have so far discussed plasmons that are invariant along the length of the nanoribbon (*i.e.*, as those excited by light impinging normally to graphene, $k_\parallel = 0$), we represent in Figs. 2.7(c),(d) the full plasmon dispersion relation for a nanoribbon either under inhomogeneous doping produced by $\mathbf{E}_0$ [Fig. 2.7(c)], or uniform doping [Fig. 2.7(d)]. The dispersion relations are rather different in both situations, with the inhomogeneously doped nanoribbon showing a denser set of modes, as well as higher localization of the lowest-energy plasmons for large $k_\parallel$ [86].

Finally, we need to mention that the decay rate γ obtained from the Drude model [see Eq. (1.16)] presents now a spatial dependence on the position through $|E_{\rm F}(\mathbf{R})|$. However, since the local contribution to losses is proportional to $\mathrm{Re}\{\sigma^{\rm Drude}(\omega)\} = (e^2/\pi\hbar^2)|E_{\rm F}|\gamma/\left(\omega^2+\gamma^2\right)$ (*i.e.*, independent of $\mathbf{R}$), we conclude that the inhomogeneity of the decay rate is nonetheless translated into a uniform spatial distribution of

losses. We need to remark that, during this section, we have obtained the decay rate using the impurity-limited approximation for the constant dc graphene mobility $\mu = 10000\,\mathrm{cm}^2/(\mathrm{V\,s})$ [see last paragraph of section (1.4.1)].

2.3 Plasmons in inhomogeneously doped nanodisks

In this section, we change the geometry under study, and we focus on plasmons generated in self-standing graphene nanodisks with small diameter D. In addition to the typical uniform doping distribution, we discuss in particular two different inhomogeneous doping configurations: (i) charged nanodisks under a uniform potential where the additional amount of charge carriers is self-consistently distributed along the graphene surface, and (ii) neutral nanodisks exposed to a neighboring external point charge.

Our work is based on the study of the electromagnetic monopolar ($m = 0$) and the lowest-order dipolar modes ($m = 1$) sustained by the nanodisks, whereas the potential evolves as $\Phi(\mathbf{R},\omega) = \Phi(R,\omega)\,\mathrm{e}^{\mathrm{i}m\varphi}$, with the azimuthal angle φ and the polar coordinates $\mathbf{R} = (R,\varphi)$ [see orange arrows in the lower inset of Fig. 2.8(b)]. In this section, the doping charge carriers density n is also obtained via an electrostatic boundary-element calculation, and the dielectric response of graphene is taken from the Drude model [see Eq. (1.16)].

2.3.1 Disks under uniform potential doping

We start by analyzing charged nanodisks where additional carriers are rearranged to produce a uniform potential

$$V = \int_{R'<D/2} \mathrm{d}^2\mathbf{R}'\ \frac{[-en(R')]}{|\mathbf{R}-\mathbf{R}'|}. \tag{2.29}$$

We numerically solve this integral equation by expanding the Coulomb interaction in terms of Legendre polynomials of order l as [120]

$$\frac{1}{|\mathbf{R}-\mathbf{R}'|} = \sum_{l=0}^{\infty} \frac{R_<^l}{R_>^{l+1}} P_l(\cos(\varphi-\varphi')), \tag{2.30}$$

where $R_> = \max\{R, R'\}$ and $R_< = \min\{R, R'\}$. Besides, changing the radial variable to $\theta = 2R/D$, we can rewrite Eq. (2.29) as

$$\frac{-2V}{eD} = \sum_{n=0}^{\infty} I_{2n,0} \left[\frac{1}{\theta^{2n+1}} \int_0^{\theta} \mathrm{d}\theta' \theta'^{2n+1} n(\theta') + \theta^{2n} \int_{\theta}^{1} \frac{\mathrm{d}\theta'}{\theta'^{2n}} n(\theta') \right], \tag{2.31}$$

where

$$I_{l,m} = \int_{-\pi}^{+\pi} \mathrm{d}\phi \cos(m\phi)\, P_l(\cos(\phi)), \tag{2.32}$$

with $\phi = \varphi - \varphi'$, and in particular,

$$\begin{aligned} I_{2n,0} &= \frac{2\pi}{16^n} \frac{[(2n)!]^2}{(n!)^4}, \\ I_{2n+1,1} &= \frac{\pi}{2^{4n+1}} \frac{(2n)!\,(2n+2)!}{n!\,[(n+1)!]^2}, \end{aligned} \tag{2.33}$$

with $I_{2n+1,0} = I_{2n,1} = 0$ for integers n. We solve the integral of Eq. (2.31) following a similar approach as in section (2.2), where a discretization through a set of N equally spaced points is used, so that $\theta_i = (i + 1/2)\kappa$, with $i = 0, \ldots, N-1$ and $\kappa = 1/N$. Finally, normalizing the density of charge carriers to $n^{\infty} = -V/2\pi eD$ (*i.e.*, the density in each of the infinite plates of a capacitor with a voltage difference V and a plate separation $D/2$), we find

$$\frac{n(\theta_i)}{n^{\infty}} = 4\pi \sum_{i'=0}^{N-1} \left[M^{-1}\right]_{ii'}, \tag{2.34}$$

with

$$M_{ii'} = \begin{cases} \sum_{n=0}^{\infty} I_{2n,0} \dfrac{I_{i'}^n}{\theta_i^{2n+1}}, & i' < i, \\ \sum_{n=0}^{\infty} I_{2n,0} L_i^n, & i' = i, \\ \sum_{n=0}^{\infty} I_{2n,0} K_{i'}^n \theta_i^{2n}, & i' > i, \end{cases} \tag{2.35}$$

where the coefficients

$$
\begin{aligned}
I_{i'}^{n} &= \int_{i'/N}^{(i'+1)/N} \theta'^{2n+1} \mathrm{d}\theta', \\
L_{i}^{n} &= \frac{1}{\theta^{2n+1}} \int_{i/N}^{(i+1/2)/N} \theta'^{2n+1} \mathrm{d}\theta' + \theta^{2n} \int_{(i+1/2)/N}^{(i+1)/N} \frac{\mathrm{d}\theta'}{\theta'^{2n}}, \\
K_{i'}^{n} &= \int_{i'/N}^{(i'+1)/N} \frac{\mathrm{d}\theta'}{\theta'^{2n}},
\end{aligned}
\tag{2.36}
$$

admit straightforward closed-form solutions. The charge carriers density profile obtained with this fine-element method agrees [90] with the purely analytical profile expected $n(\theta)/n^{\infty} = (4/\pi)/\sqrt{1-\theta^2}$ [121]. Moreover, the effective capacitance density $C = Q/V$ from the total charge $Q = \left|\int \rho(\mathbf{R}) \mathrm{d}^2\mathbf{R}\right| = (\pi e D^2/2) \int_0^1 \theta\, n(\theta)\, \mathrm{d}\theta$ yields $C = 0.33D$ [90], which is in good agreement with the analytical result $C = D/\pi \approx 0.32D$ [121]. In particular, this method converges for $l \sim 50$ terms in the Legendre polynomials, and $N \sim 2000$ discretization points along the radial distance of the disk.

For the calculation of n, we can express $n(\mathbf{R}) = h(\mathbf{R}) \big/ [\pi(D/2)^2]$, where $h(\mathbf{R})$ is a dimensionless envelope function related to the occupation function as follows $f(\mathbf{R}) = \sqrt{h(\mathbf{R})} \big/ \langle \sqrt{h(\mathbf{R})} \rangle$. In absence of external fields, considering (i) the azimuthal symmetry $m = 0, 1$ of the potential, (ii) the Drude model for the conductivity where $\sigma(\mathbf{R}, \omega) = \sigma(\omega) f(\mathbf{R})$, and (iii) the Coulomb expansion in Legendre polynomials presented in Eq. (2.30), we can express the electrostatic potential for the disk given in Eq. (1.34) as

$$
\Phi(\theta, \omega) = \eta(\omega) \int_0^{\infty} \mathrm{d}\theta' \frac{\theta'}{\theta_>} g_m \left(\frac{\theta_<}{\theta_>} \right) \left[\Phi'' f + \Phi' \left(f' + \frac{f}{\theta'} \right) - \frac{m^2 f}{\theta'^2} \Phi \right]. \tag{2.37}
$$

Here, we use that $\Phi'(R, \omega) = \partial \Phi(R, \omega)/\partial R$, the parameter $\eta(\omega)$ is given by Eq. (1.36) with $\varepsilon_1 = \varepsilon_2 = 1$, and

$$
g_m(\mu) = \sum\nolimits_{l=0}^{\infty} \mu^l I_{l,m}, \tag{2.38}
$$

with $I_{l,m}$ taken from Eq. (2.32).

In order to get the plasmon frequencies, we discretize the self-consistent potential of Eq. (2.37) in the same manner as above for obtaining the charge carrier

distribution, so that we finally get again an eigensystem [90] with real eigenvalues η_j''. The plasmon frequencies of each mode become $\omega_{\rm p}^{\rm Drude} \approx \omega_0''/\sqrt{-\eta_j''} - {\rm i}\gamma/2$, where $\omega_0'' = (e/\hbar)\sqrt{2\langle|E_{\rm F}|\rangle/\pi D}$ is the normalization frequency used in this case, then the relation between these eigenvalues and the ones presented in section (1.5.4) is $\eta_j'' = 2\eta_j$.

Remarkably, the occupation function $f(\mathbf{R})$ is discontinuous at the disk edge as observed in the upper inset of Fig. 2.8(b), thus leading to a divergence of $f'(\mathbf{R})$. We numerically avoid this issue by introducing a small Gaussian smoothing of width Δ in $f(\mathbf{R})$ through the substitution

$$f(\theta) \longleftarrow \frac{\int_0^{\theta_{\rm max}} {\rm d}\theta' f(\theta')\, {\rm e}^{\frac{-(\theta-\theta')^2}{\Delta^2}}}{\int_0^{\theta_{\rm max}} {\rm d}\theta'\, {\rm e}^{\frac{-(\theta-\theta')^2}{\Delta^2}}}. \tag{2.39}$$

We take the upper integration limit as $\theta_{\rm max} = 1 + 3\Delta$, where $\Delta = 10^{-3}$ is the converged value that we find for all the doping configurations in the $\Delta \to 0$ limit [90]. Furthermore, the discretization intervals in Eqs. (2.34)-(2.38) need to be redefined by setting $\kappa = (1 + 3\Delta)/N$.

In Fig. 2.8 we compare the plasmon induced charge densities of a uniformly doped nanodisk [panel (a)] with inhomogeneous doping under uniform potential V [panel (b)]. The induced charge densities are again obtained from the self-consistent potential using Eq. (1.14). We observe that for the two modes studied $m = 0$ (black curves) and $m = 1$ (red curves), a piling up near the disk edges is observed. This is combined with a close resemblance between both doping configurations which turns into similar plasmon frequencies [see Fig. 2.10]. Taking into account these features, although from the upper inset of Fig. 2.8(b) we observe that the spatial distribution of the doping is remarkably different, we can conclude that the doped nanodisk under uniform potential is qualitatively well described as a uniformly doped nanodisk with the same value of $\langle|E_{\rm F}|\rangle$. Experimentally, the doping via a uniform potential can be achieved through small leads compared to D.

On the other hand, for the uniform doping case (*i.e.*, disks connected to a transparent conductive layer in a top-gate configuration [71]), we know from section (1.5.2) that the $m = 0$ mode cannot couple with external light. For its excitation, we need either (i) a highly reflecting metallic element (*e.g.*, a gold sphere) that enhances the

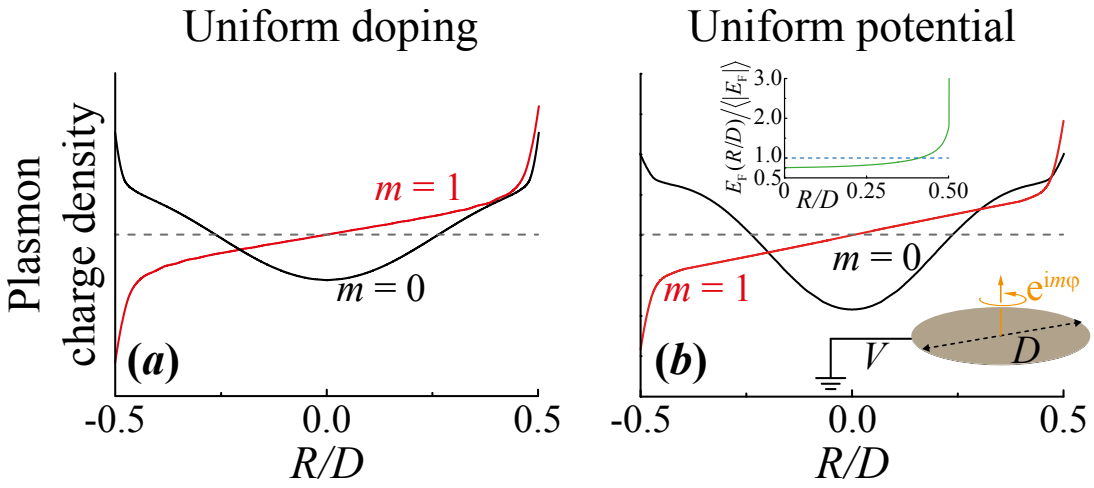

Figure 2.8: Induced charge density of a graphene nanodisk of diameter D under uniform doping and inhomogeneous doping by a uniform potential. (a) Induced charge density of the uniformly doped graphene corresponding to the lowest-order dipolar (red curve) and monopolar modes (black curve), with $m = 1$ and $m = 0$ azimuthal symmetries, respectively. (b) Induced charge density at the plasmon frequency of the same modes as in panel (a). The upper inset displays the Fermi energy profile along the radial distance normalized to its average value. The green solid curve corresponds to the uniform potential case while the blue dashed line represents the uniform doping case. The lower inset shows a sketch of the geometry studied. The figure is adapted from Ref. [90].

coupling with light impinging parallel to the nanodisk surface [90], or (ii) an optical emitter placed close to the disk in its axis of symmetry and oriented parallel to the surface [31, 90].

Finally, for the dipolar mode we have from the blue solid line of Fig. 2.10 that $\omega_{\mathrm{p}}^{\mathrm{Drude}}/\omega_0'' = 2.621$, or equivalently, $\eta_1 \approx -0.073$. This value is in excellent agreement with converged BEM calculations [90]. Moreover, considering that the dipolar mode is dominant, we observe that the eigenvalue fits the purely analytical value given in section (1.5.4) $\sum_j \eta_j = -2/3\pi^2 \approx -0.068$. These results highlight the accuracy and validity of our model.

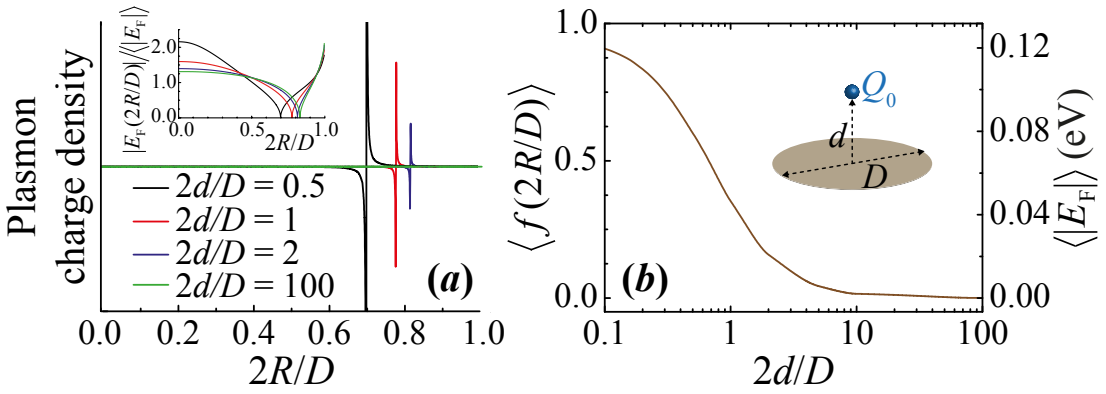

Figure 2.9: Plasmons in a neutral graphene nanodisk exposed to a neighboring external point charge Q_0. (a) Plasmon induced charge density for $m = 1$ azimuthal symmetry and different distance-to-radius ratio $2d/D$. The upper inset illustrates the profile of $|E_{\rm F}\,(2R/D)\,|$ normalized to the average value. We plot $|E_{\rm F}|$ because of the local response is nearly insensitive to the sign of $E_{\rm F}$. (b) Evolution of the average Fermi energy with $2d/D$. We plot in the left axis the average occupation function $\langle f\,(2R/D)\rangle$, from which the average Fermi energy is obtained as $\langle|E_{\rm F}|\rangle = (2\hbar v_{\rm F}/D)\,\sqrt{|Q_0/e|}\langle f\,(2R/D)\rangle$. The right axis corresponds to $\langle|E_{\rm F}|\rangle$ for $D = 10\,$nm and $Q_0 = -e$. The inset shows a sketch of the geometry. The figure is adapted from Ref. [90].

2.3.2 Disks doped by an external point charge

A sketch of the second inhomogeneous doping configuration here considered is depicted in the inset of Fig. 2.9(b). We consider now a point charge Q_0 placed along the symmetry axis of a neutral graphene nanodisk at a distance d. The point charge can be introduced experimentally through tipped gates (*e.g.*, two facing tips at opposite polarity with the nanodisk placed in the middle point). Thus, the charge carriers redistribute their position owing to the external charge field. In order to get their spatial distribution, the potential V described in Eq. (2.29) has to be supplemented by the potential created by the external charge, which results in

$$V = \frac{Q_0}{\sqrt{R^2+d^2}} + \int_{R'<D/2} {\rm d}^2\mathbf{R}'\,\frac{[-en(R')]}{|\mathbf{R}-\mathbf{R}'|}. \tag{2.40}$$

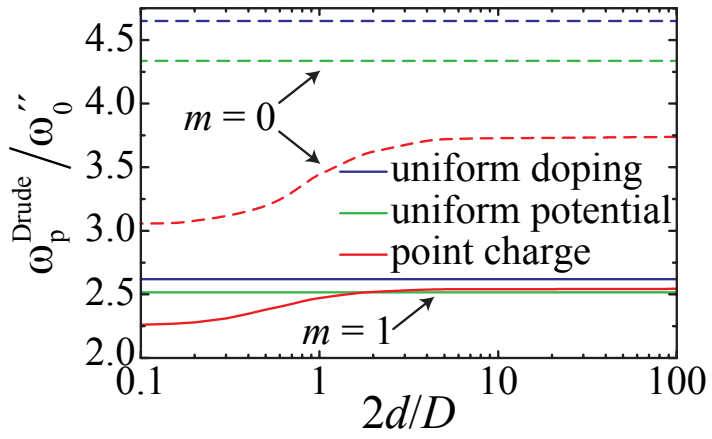

Figure 2.10: Graphene-disk plasmon frequencies for three different doping configurations. Evolution of the plasmon frequency with distance-to-radius ratio $2d/D$ for the doping configurations studied in this section. The plasmon frequency $\omega_{\mathrm{p}}^{\mathrm{Drude}}$ is given relative to $\omega_0'' = (e/\hbar)\sqrt{2\langle|E_{\mathrm{F}}|\rangle/\pi D}$ for both $m = 1$ (solid curves) and $m = 0$ (dashed curves) azimuthal symmetries. The figure is adapted from Ref. [90].

We follow a similar discretization procedure as in the previous section in order to solve this equation, but now we have an extra variable V, which is fixed by the additional constraint that the total doping charge on the disk is zero, $\int_0^1 \theta\, n(\theta)\, \mathrm{d}\theta = 0$. This expression, in combination with the analogous of Eq. (2.34),

$$n(\theta_i) = \frac{4}{eD^2} \sum\nolimits_{i'=0}^{N-1} \left[M^{-1}\right]_{ii'} \left[\frac{Q_0}{\sqrt{\theta_{i'}^2 + (2d/D)^2}} - \frac{DV}{2}\right], \tag{2.41}$$

permits us to calculate the charge carriers density profile $n(\mathbf{R})$. Furthermore, the induced charge densities and the plasmon frequencies are calculated in the same manner as the uniform potential doping case.

We observe from the inset of Fig. 2.9(a) that the charge carriers density is distributed into two regions of opposite sign separated by a circular boundary. This translates into dipolar plasmons that are strongly confined to the points of vanishing carrier concentration as shown in panel (a), similar to those that were discussed above in section (2.2.3). When the external charge is approaching the disk, the plasmon follows the junction displacement towards the disk center. Remarkably, from

Fig. 2.10, we observe that the dipolar plasmon frequency (red solid curve) for $d > D$ slightly differs from the uniform doping configuration for the same value of $\langle|E_{\rm F}|\rangle$ (blue solid line). However, substantial corrections appear when $2d < D$.

In Fig. 2.9(b), we plot on the left axis the evolution of the average occupation function with the distance-to-radius ratio. Interestingly, for a $D = 10\,\text{nm}$ nanodisk exposed to a single electron ($Q_0 = -e$) placed at a distance $d = 1.5\,\text{nm}$, we achieve $\langle|E_{\rm F}|\rangle = 0.1\,\text{eV}$, that corresponds to $\langle|n|\rangle \approx 0.75 \times 10^{12}\,\text{cm}^{-2}$. Moreover, from Fig. 2.10, we get a dipolar plasmon energy $\sim 0.2\,\text{eV}$, which belongs to the range of acceptance $\hbar\omega_{\rm p}^{\rm Drude} < 2E_{\rm F}$ for TM modes described in section (1.5.2). Consequently, a single distant electron (or a singly charged ion) is enough to trigger the creation of a plasmon in a neutral graphene nanodisk, thus suggesting a method for optically sensing the presence of neighboring atoms. Finally, we observe from the red dashed curve of Fig. 2.10, that the plasmon frequency of the monopolar mode is remarkably different to the one of the uniform doping configuration, and this behavior is more relevant when $2d < D$.

2.4 Plasmons in periodically doped graphene

We have asserted in section (1.5.2) that SPPs cannot be directly excited by external light in uniformly doped extended graphene due to the momentum mismatch. However, there are alternative methods to overcome this problem. The most common strategies involve the use of prisms (*e.g.*, high-index dielectrics in the well-known Otto [122] and Kretschmann [123] configurations), scattering from topological defects [124], attenuated total reflection (ATR) [125], or periodically doped systems [88, 103, 126, 127, 128, 129].

In the latter, a periodic doping provides the missing momentum needed by external light to excite a SPP [130] since the momentum of the plasmon is conserved up to a reciprocal lattice vector $\mathbf{G}$ due to the Bloch theorem [18]. In other words, when extended graphene is under the effect of a weak periodic potential $\Phi(\mathbf{r}, \omega)$, a plasmonic band structure appears in the first Brillouin zone (1BZ) so that it is possible for the external light to excite directly the SPPs of the upper bands. This situation is studied in Fig. 2.11 where we represent the 1BZ of an extended graphene layer doped by a square-arranged potential with a certain lattice period a that fulfills the condition

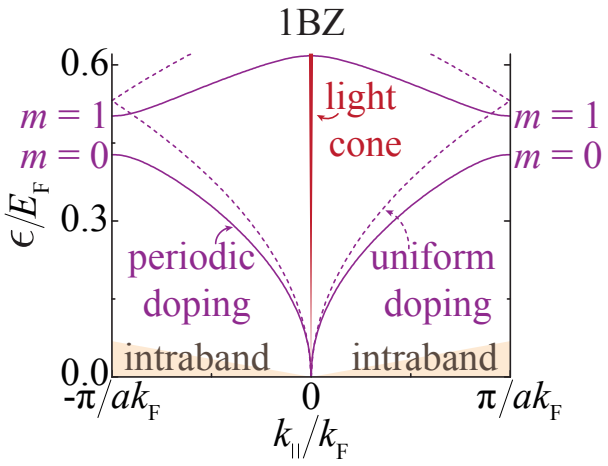

Figure 2.11: First Brillouin zone of periodically doped extended graphene showing its optical dispersion. The periodicity of the square-arranged doping is a. The solid curves represent the folded plasmon bands of the monopolar ($m = 0$) and dipolar modes ($m = 1$), respectively. At the edges of the 1BZ, a gap opens. The dashed curves correspond to the same modes but for uniformly doped extended graphene. The orange folded triangle at the bottom corresponds to the region of e-h pairs intraband transitions. The figure is adapted from Ref. [103].

$\lambda \gg a \gg \lambda_F$, with λ as the external light wavelength. The dashed curves correspond to the plasmonic bands of uniformly doped extended graphene, where the folded lowest band (*i.e.*, monopolar mode, $m = 0$) evolves as Eq. (1.27) with $\varepsilon_1 = \varepsilon_2 = 1$. Since we use the Drude model for the conductivity, we reproduce here the same behavior as in the lower left corner of Fig. 1.8(b) for small parallel wave vectors. The small folded branch touching the edge of the 1BZ corresponds to the dipolar mode, and its plasmon frequency evolves as $\omega_{\rm spp}^{\rm Drude} = -2\pi {\rm i}\, \sigma^{\rm Drude}(\omega)|k_\parallel - mG|$, with $G = 2\pi/a$ and $m = 1$ (the integer m determines the multipole order, *e.g.*, $m = 2$ is the quadrupole, $m = 3$ the hexapole, etc.). Additionally, the solid curves act for the periodic doping case. Here, we observe a clear plasmon energy shift, and as predicted theoretically [18], a band gap of amplitude $2|\Phi_{\mathbf{G}}(\omega)|$ [*i.e.*, Fourier transform of the potential $\Phi_{\mathbf{G}}(\omega) = a^{-2}\int_{\rm unit\,cell} {\rm d}^2\mathbf{R}\, {\rm e}^{-{\rm i}\mathbf{G}\cdot\mathbf{R}}\, \Phi(\mathbf{R},\omega)$] is opened at the edge of the 1BZ. Remarkably, the plasmonic bands are perpendicular to these edges, leading to the creation of Van Hove singularities [21]. Finally, we observe now that the light cone can match the dipolar band (also upper bands) so that a SPP can be excited.

2.4.1 Periodic doping by point charges

In this section, we particularly describe the periodic doping of self-standing extended graphene through a square array of point charges of either equal [see Fig. 2.12(a)] or alternating [see Fig. 2.12(b)] sign, placed at a certain distance d above the extended graphene. Due to the periodicity, we can restrict our study to one unit cell with characteristic size a, and a similar scaling law to that presented in section (1.5.4) can be used here since $\lambda \gg a$. Assuming the Drude model [see Eq. (1.16)], the periodicity of the structure allows us to write the conductivity as Fourier series as

$$\sigma(\mathbf{R},\omega) = \sum\nolimits_{\mathbf{G}} \sigma_{\mathbf{G}}(\omega)\, \mathrm{e}^{\mathrm{i}\,\mathbf{G}\cdot\mathbf{R}}, \tag{2.42}$$

where the $\sigma_{\mathbf{G}}(\omega)$ coefficients are independent of the position.

The potential in the real space can be expanded using the same formalism

$$\Phi(\mathbf{r},\omega) = \sum\nolimits_{\mathbf{G}'} \Phi_{\mathbf{G}'}(\omega)\, \mathrm{e}^{\mathrm{i}\left(\mathbf{G}'+\mathbf{k}_{\parallel}\right)\cdot\mathbf{R} - |\mathbf{G}'+\mathbf{k}_{\parallel}||z|}, \tag{2.43}$$

where the dependence on $\mathbf{k}_{\parallel}$ comes from the external potential. Implementing Eqs. (2.42) and (2.43) into Eq. (1.34), and considering that graphene is in the $z = 0$ plane, the self-consistent potential can be rewritten in the Fourier space as

$$\Phi_{\mathbf{G}}(\omega) = \Phi^{\mathrm{ext}}_{\mathbf{G}}(\omega) + \sum\nolimits_{\mathbf{G}'} \frac{(\mathbf{G}+\mathbf{k}_{\parallel})\cdot(\mathbf{G}'+\mathbf{k}_{\parallel})}{|\mathbf{G}+\mathbf{k}_{\parallel}|} \left[\frac{-2\pi\mathrm{i}\sigma_{\mathbf{G}-\mathbf{G}'}(\omega)}{\omega}\right] \Phi_{\mathbf{G}'}(\omega). \tag{2.44}$$

Before solving the former equation, we need to know the profile of the doping charge carrier density n under our specific doping configurations. We proceed by (i) using the method of charge images [111], (ii) expressing the Coulomb potential as

$$\frac{1}{r} = \int \frac{\mathrm{d}^2\mathbf{Q}}{(2\pi)^2}\, \frac{2\pi}{Q}\, \mathrm{e}^{\mathrm{i}\mathbf{Q}\cdot\mathbf{R} - Q|z|}, \tag{2.45}$$

and (iii) performing the sum over charges via the identity

$$\sum\nolimits_i \mathrm{e}^{\mathrm{i}\mathbf{Q}\cdot\mathbf{R}_i} = \frac{(2\pi)^2}{a^2}\sum\nolimits_{\mathbf{G}} \delta\left(\mathbf{Q}-\mathbf{G}\right), \tag{2.46}$$

where the sum on the left runs over 2D lattice sites $\mathbf{R}_i$ and δ is the Dirac delta function. We find that the screening charge carrier density per unit cell reduces to

$$n(\mathbf{R}) = \frac{|Q_0/e|}{a^2} h(\mathbf{R}), \tag{2.47}$$

where the envelope function $h(\mathbf{R})$ is defined as

$$h(\mathbf{R}) = \frac{|Q_0/e|}{a^2}\sum\nolimits_{\mathbf{G}''} \mathrm{e}^{\mathrm{i}\mathbf{G}''\cdot\mathbf{R}-Gd}\left[1-\mathrm{e}^{\mathrm{i}(G''_x+G''_y)a/2}\right]. \tag{2.48}$$

Here, we consider that the 2D origin $R = 0$ is taken below one of the positive charges. The factor 1 inside the square bracket stays for the positive charge, and the complex exponential accounts the effect of the negative charge at the center of the unit cell. Since $|E_{\mathrm{F}}(\mathbf{R})| = \hbar v_{\mathrm{F}}\sqrt{\pi|n(\mathbf{R})|}$, we conveniently define the occupation function

$$f(\mathbf{R}) = \sqrt{|h(\mathbf{R})|} = \sum\nolimits_{\mathbf{G}''} f_{\mathbf{G}''}\,\mathrm{e}^{\mathrm{i}\mathbf{G}''\cdot\mathbf{R}}, \tag{2.49}$$

where the coefficients $f_{\mathbf{G}''}$ present the next expression

$$f_{\mathbf{G}''} = \frac{1}{a^2}\int_{\text{unit cell}} \mathrm{d}^2\mathbf{R}\,\mathrm{e}^{-\mathrm{i}\mathbf{G}''\cdot\mathbf{R}}\sqrt{|h(\mathbf{R})|}. \tag{2.50}$$

Considering that $\mathbf{G}'' = \mathbf{G}-\mathbf{G}'$, we can rewrite the second fraction of Eq. (2.44) as follows

$$\frac{-2\pi\mathrm{i}\sigma_{\mathbf{G}-\mathbf{G}'}(\omega)}{\omega} = \frac{a}{2\pi}\frac{\omega_0'''^2}{\omega(\omega+\mathrm{i}\gamma)}\frac{f_{\mathbf{G}-\mathbf{G}'}}{f_0}, \tag{2.51}$$

where $\omega_0''' = (e/\hbar)\sqrt{4\pi\langle|E_{\mathrm{F}}|\rangle/a}$ is the normalization frequency of the system used here. Moreover, we establish $f_0 = \langle|E_{\mathrm{F}}|\rangle/E_{\mathrm{F}}^{\infty}$ with

$$E_{\mathrm{F}}^{\infty} = \hbar v_{\mathrm{F}}\sqrt{\pi|Q_0/e|/a^2} \tag{2.52}$$

as the Fermi energy obtained in the equal-sign doping case in the limit $d \gg a$. Furthermore, we define the function $\Psi_{\mathbf{G}}(\omega) = \sqrt{|\mathbf{G}+\mathbf{k}_{\|}|}\,\Phi_{\mathbf{G}}(\omega)$ so that Eq. (2.44)

reduces to a system of equations

$$\Psi_{\mathbf{G}}(\omega) = \Psi_{\mathbf{G}}^{\mathrm{ext}}(\omega) + \frac{\omega_0'''^2}{\omega(\omega + \mathrm{i}\gamma)} \sum\nolimits_{\mathbf{G}'} N_{\mathbf{G}\mathbf{G}'}\, \Psi_{\mathbf{G}'}(\omega), \tag{2.53}$$

where we have defined the real, symmetric, and dimensionless matrix

$$N_{\mathbf{G}\mathbf{G}'} = \frac{a}{2\pi} \sum\nolimits_{\mathbf{G}'} \frac{(\mathbf{G} + \mathbf{k}_\parallel) \cdot (\mathbf{G}' + \mathbf{k}_\parallel)}{\sqrt{|\mathbf{G} + \mathbf{k}_\parallel|\, |\mathbf{G}' + \mathbf{k}_\parallel|}} \frac{f_{\mathbf{G}-\mathbf{G}'}}{f_0}. \tag{2.54}$$

Using the same procedure as in the previous sections of this chapter, if we set $\Phi^{\mathrm{ext}}(\omega) \approx 0$, we need to solve an eigensystem [103] whose real eigenvalues η_j''' permit us to find the plasmonic bands, since $\omega_{\mathrm{spp}}^{\mathrm{Drude}} \approx \omega_0'''/\sqrt{\eta_j'''} - \mathrm{i}\gamma/2$.

We plot in Figs. 2.12(c),(d) the $k_\parallel$-resolved plasmonic bands for the equal-sign doping (panel (c)) and alternating-sign doping (panel (d)) along a representative path of the 1BZ [see lower inset in panel (d)]. We plot the bands for diverse values of the d/a ratio, which determines the amplitude of the periodic doping modulation. In panel (c), the plasmonic bands evolve from those of uniformly doped extended graphene (blue dashed curves) to match perpendicularly the edges of the 1BZ showing up band gaps (X and M points) for small values of d/a (*e.g.*, the green curves where $d/a = 0.1$). In panel (d), the two lowest plasmonic bands display a flat range that extends from X to M. Remarkably, under this doping configuration, the normalized SPP frequency $\omega_{\mathrm{spp}}^{\mathrm{Drude}}/\omega_0'''$ is independent of d/a, unless $d \ll a$. This behavior is produced by the vanishing of $\langle |E_{\mathrm{F}}| \rangle$ with increasing d/a due to sign cancellations in the doping potential [103]. In this limit, the doping charge carrier density $n(x, y) = [4|Q_0/e|/a^2] \{\exp(-2\pi d/a)\} [\cos(2\pi x/a) + \cos(2\pi y/a)]$ presents a perfect harmonic profile. Finally, we observe that higher-order bands are nearly dispersionless over the entire 1BZ.

In Figs. 2.12(e),(f) we depict the near-field intensity for selected SPP modes normalized to the maximum value of each case. The near-field is obtained from the potential components in the parallel wave vector space as

$$\mathbf{E}(\mathbf{r}, \omega) = -\nabla \Phi(\mathbf{r}, \omega) = -\nabla \sum\nolimits_{\mathbf{G}} \int_{1\mathrm{BZ}} \frac{\mathrm{d}^2 \mathbf{k}_\parallel}{(2\pi)^2}\, \mathrm{e}^{\mathrm{i}(\mathbf{G}+\mathbf{k}_\parallel)\cdot\mathbf{R} - |\mathbf{G}+\mathbf{k}_\parallel|\,|z|}\, \Phi_{\mathbf{G}}(\omega), \tag{2.55}$$

for the $z = 0$ plane, where graphene lies. The multiple panels of Fig. 2.12(e) represent

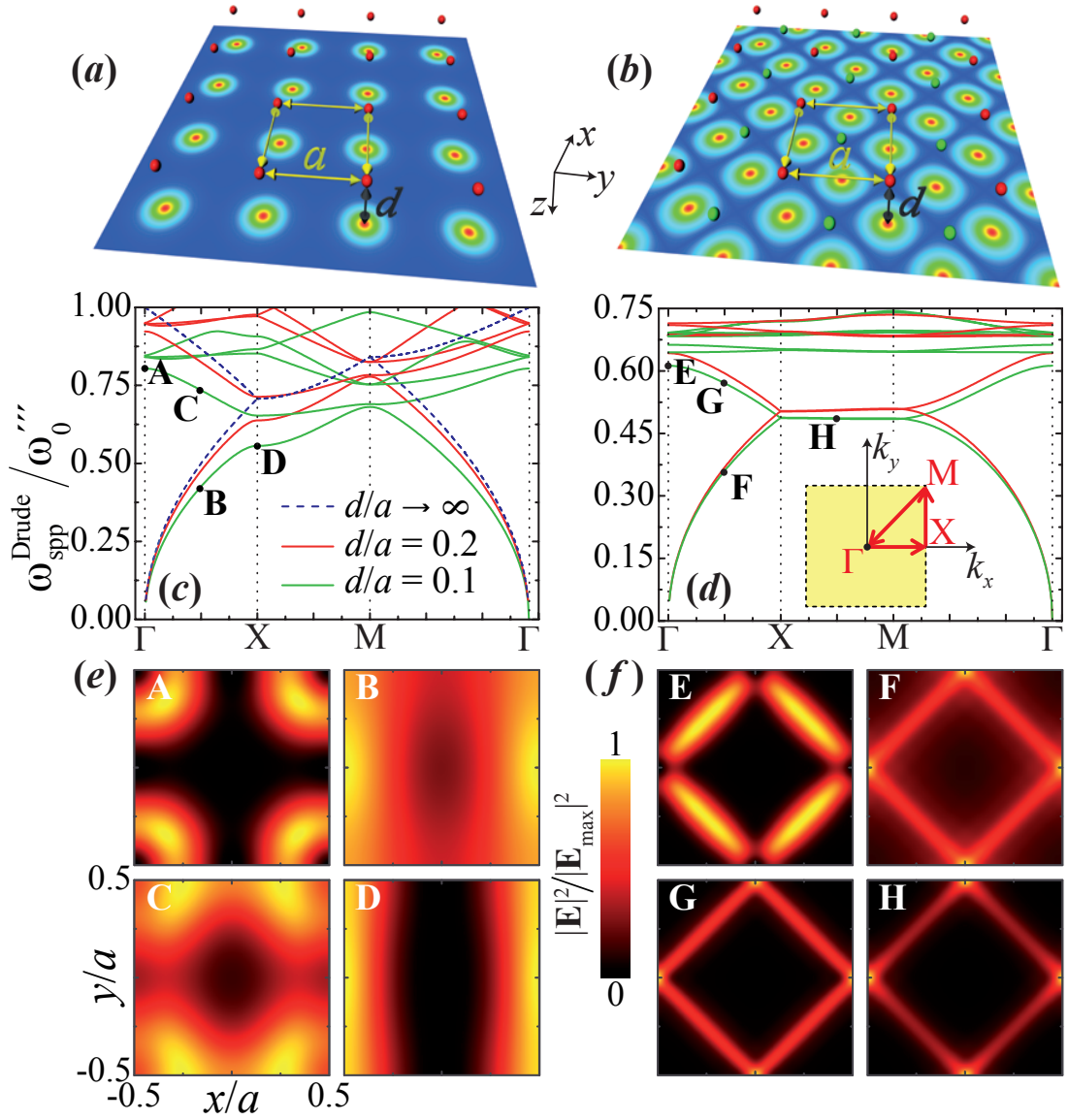

Figure 2.12: Plasmonic bands in periodically doped graphene by point charges. (a),(b) Sketches of the two different doping configurations considered. In panel (a), the doping is produced by a square array of equal-sign point charges $Q_0 = e$ (red spheres) with periodicity a, and placed at a distance d over the graphene layer (note that panels (c) and (e) correspond to the equal-sign doping while panels (d) and (f) to alternating-sign doping). In panel (b), we alternate the sign by introducing negative charges $Q_0 = -e$ (green spheres) in the center of each square lattice. In both schemes the graphene layer is assumed to be at $z = 0$ height and schematically represented by its Fermi level. (c),(d) Plasmonic bands along the 1BZ [see inset of panel (d)] for different values of the ratio d/a. The SPP frequency ω_{spp}^{Drude} is normalized to $\omega_0''' = (e/\hbar)\sqrt{4\pi\langle|E_F|\rangle/a}$. (e),(f) Parallel component of the graphene near-field intensity at some representative SPP modes along the unit cell area (see plot of point C) for a ratio $d/a = 0.1$. The figure is adapted from Ref. [103].

the unit cell area corresponding to the equal-sign doping. Here, we assume that a positive charge is placed over each corner of the plots. The SPP at A is a dipolar mode excited under normal incident light; B represents a plasmon moving along the ΓX direction; C is similar to B, but with a node along ΓM because it belongs to the second band and it has to be orthogonal to B; finally, D behaves similarly to B, but since it has a spatial period $2a$ along ΓX, its intensity possesses maxima at the vertical sides of the unit cell.

In the case of alternating-sign doping [see Fig. 2.12(f)], a negative charge is added at the center of each plot. Here, the near-field intensities possess a strong localization in the regions of vanishing doping charge [*i.e.*, $\pm x = \pm y = (m + 1/2)a$, with m being an integer]. This behavior is similar to the trapping of graphene plasmons in ribbons and disks already mentioned in sections (2.2.3) and (2.3.2). Therefore, we can interpret that the dispersionless response of the upper plasmonic bands is produced by the strong localization of the SPPs at the regions of vanishing n. In all these results, we have assumed that the decay rate is $\gamma = 0.01\omega_0'''$.

2.4.2 Local density of optical states

If we place an optical emitter (*e.g.*, molecules and quantum dots) close to a graphene layer, the plasmonic response of the latter can be substantially modified, giving rise to changes in the radiative decay rate [131, 132] of the emitter. This phenomenon is quantified through a modulation in the local density of optical states (LDOS), which measures the intensity of the normalized photon modes as function of the position and energy [133, 134]. The radiative decay rate of an optical emitter placed at $\mathbf{r}_0$ is [135] $\gamma_{\rm r}(\omega) = (4\pi^2\omega\,|\mathbf{p}(\omega)|^2/\hbar) \times \mathrm{LDOS}(\mathbf{r}_0, \omega)$, where $\mathbf{p}(\omega)$ and ω are its transition dipole and emission frequency, respectively. Besides, the $\mathrm{LDOS}(\mathbf{r}_0, \omega)$ is obtained from the electric field $\mathbf{E}$ acting back at the position of the optical emitter as [26]

$$\mathrm{LDOS}(\mathbf{r}_0, \omega) = \sqrt{\frac{(\varepsilon_1 + \varepsilon_2)}{2}}\left[\mathrm{LDOS}_0(\omega) + \mathrm{LDOS}^{\rm ind}(\mathbf{r}_0, \omega)\right], \tag{2.56}$$

where ε_1 (ε_2) is the permittivity above (below) graphene,

$$\mathrm{LDOS}_0(\omega) = \frac{\omega^2}{3\pi^2 c^3} \tag{2.57}$$

is the value in vacuum projected along a certain Cartesian direction, and

$$\mathrm{LDOS}^{\mathrm{ind}}(\mathbf{r}_0,\omega)=\frac{1}{2\pi^2\omega\,p^2(\omega)}\,\mathrm{Im}\{\mathbf{E}(\mathbf{r}_0,\omega)\cdot\mathbf{p}^*(\omega)\}. \tag{2.58}$$

is the induced component. Thereby, as the plasmons of doped graphene trigger an enhancement of the induced electric field, large values of the LDOS can be achieved due to an increase in the interaction with nearby optical emitters. Remarkably, if we only consider graphene as the optical emitter itself, Eq. (2.58) is negligible [31], and thus, we recover the expression given in Eq. (1.32) for $\gamma_{\mathrm{r}}(\omega)$.

An alternative way of achieving high values of $\gamma_{\mathrm{r}}(\omega)$ for optical emitters is via a periodic doping which leads to divergences in the LDOS associated with Van Hove singularities. Here, we study this possibility by considering the interaction of our periodically extended graphene layer with an external optical emitter placed at a height z_0. Using a similar fashion as the total potential given in Eq. (2.55), we conveniently rewrite the expression of the external potential considering (i) Eq. (2.45), and (ii) $\Phi^{\mathrm{ext}}(\mathbf{r},\omega)=-\mathbf{p}(\omega)\cdot\nabla\,(1/|\mathbf{r}-\mathbf{r}_0|)$, so that in the graphene plane we find

$$\Phi^{\mathrm{ext}}(\mathbf{R},\omega)=\sum\nolimits_{\mathbf{G}}\int_{1\mathrm{BZ}}\frac{\mathrm{d}^2\mathbf{k}_\parallel}{(2\pi)^2}\,\mathrm{e}^{\mathrm{i}\left(\mathbf{G}+\mathbf{k}_\parallel\right)\cdot\mathbf{R}}\,\Phi^{\mathrm{ext}}_{\mathbf{G}}(\omega), \tag{2.59}$$

where

$$\Phi^{\mathrm{ext}}_{\mathbf{G}}(\omega)=-2\pi\left[\mathrm{i}\frac{\left(\mathbf{G}+\mathbf{k}_\parallel\right)}{|\mathbf{G}+\mathbf{k}_\parallel|}\cdot\mathbf{p}(\omega)+\mathrm{sign}(z_0)\,p_z(\omega)\right]\mathrm{e}^{-\mathrm{i}\left(\mathbf{G}+\mathbf{k}_\parallel\right)\cdot\mathbf{R}_0-|\mathbf{G}+\mathbf{k}_\parallel||z_0|}. \tag{2.60}$$

Furthermore, we can also set

$$\mathrm{LDOS}^{\mathrm{ind}}=\int_{1\mathrm{BZ}}\mathrm{d}^2\mathbf{k}_\parallel\,\mathrm{LDOS}^{\mathrm{ind}}(\mathbf{k}_\parallel). \tag{2.61}$$

Thus, we solve separately each fixed $\mathbf{k}_\parallel$ component so that Eq. (2.53) remains

$$\begin{aligned}\Psi_{\mathbf{G}}(\omega)&=\left[1-\frac{\omega_0'''^2}{\omega(\omega+\mathrm{i}\gamma)}N_{\mathbf{G}\mathbf{G}'}\right]^{-1}\Psi^{\mathrm{ext}}_{\mathbf{G}}(\omega)\\&=\sum\nolimits_j\left[\Psi^{\dagger}_{\mathbf{G},j}(\omega)\cdot\Psi^{\mathrm{ext}}_{\mathbf{G}}(\omega)\right]\left[1-\frac{\omega_0'''^2/\eta_j'''}{\omega(\omega+\mathrm{i}\gamma)}\right]^{-1}\Psi_{\mathbf{G},j}(\omega),\end{aligned} \tag{2.62}$$

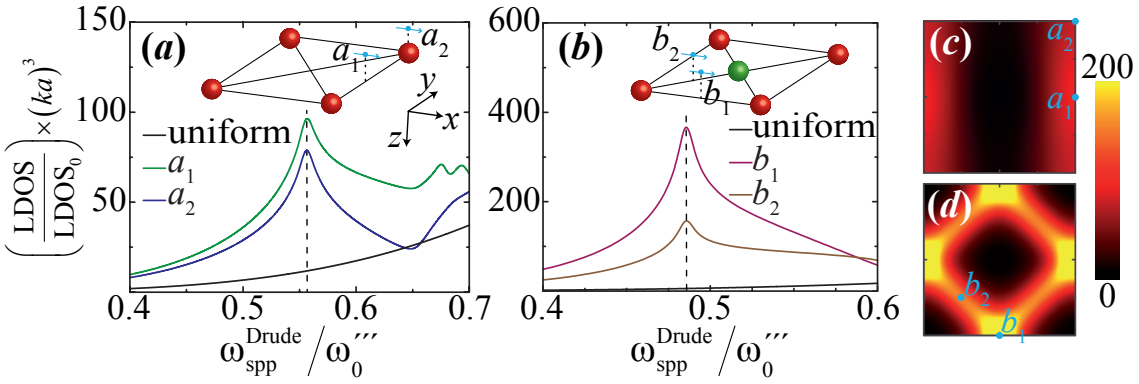

Figure 2.13: Enhancement of the local density of optical states (LDOS) in periodically doped graphene by point charges. (a),(b) LDOS under the two configurations of Figs. 2.12(a),(b) for $d/a = 0.1$. The optical emitters (blue arrows) are placed in the plane of the doping charges and their orientations and positions are described in the insets. The black solid curves correspond to uniformly doped graphene. The vertical dashed lines indicate exactly the monopolar frequencies at the edge of the 1BZ where the band gaps open [*e.g.*, in panel (a), it corresponds to the point D of Fig. 2.12(c)]. (c),(d) In-plane evolution of the LDOS for the peak frequencies of panels (a) and (b). The figure is adapted from Ref. [103].

where the sum in the second row extends over orthonormalized eigenstates of the matrix $N_{\mathbf{G}\mathbf{G}'}$ [*i.e.*, it fulfills the conditions displayed on Eq. (1.39)]. Inserting Eq. (2.55) into Eq. (2.58), and using Eq. (2.62), we finally find

$$\mathrm{LDOS}^{\mathrm{ind}}(\mathbf{k}_\parallel) = \frac{1}{4\pi^3\omega\, p^2(\omega)} \sum\nolimits_j \left|\Psi^{\dagger}_{\mathbf{G},j}(\omega)\cdot\Psi^{\mathrm{ext}}_{\mathbf{G}}(\omega)\right|^2 \mathrm{Im}\left\{\frac{\omega_0'''^2/\eta_j'''}{\omega_0'''^2/\eta_j''' - \omega(\omega+\mathrm{i}\gamma)}\right\}. \tag{2.63}$$

From this expression, we directly calculate the LDOS using Eq. (2.61) through a discretization of the 1BZ where a mesh of 200×200 points in $\mathbf{k}_\parallel$ is enough to achieve converged results.

Fig. 2.13 illustrates the evolution in the LDOS with the ratio $\omega_{\mathrm{spp}}^{\mathrm{Drude}}/\omega_0'''$ once we place an optical emitter close to the periodically doped structures presented in Figs. 2.12(a),(b). Here, we assume that the optical emitter is suspended in the same plane as the doping charges ($d/a = 0.1$), and we study the different positions and orientations presented in the insets of Figs. 2.13(a),(b). For the equal-sign doping

[*i.e.*, panel (a)], we observe a divergence in the LDOS (see vertical black dashed line) associated with a Van Hove singularity at the saddle point where the first band crosses the X value of the parallel wave vector [*i.e.*, D point in Fig. 2.12(c)]. Remarkably, an even more pronounced singularity is related with the first flat band in the XM region with the alternating-sign doping as depicted in Fig. 2.13(b). In comparison with the uniformly doped case (black solid curves) for the same level of $\langle |E_{\mathrm{F}}| \rangle$, we find an enhancement of a factor ~ 8 in panel (a) and ~ 64 in panel (b).

In Figs. 2.13(c),(d) we show the dependence of the LDOS on the lateral position that fully confirms the symmetry of the plasmonic bands contributing to the singularities: for equal-sign doping, the LDOS map [see Fig. 2.13(c)] follows the near-field intensity at the saddle point D in Fig. 2.12(e), which is dominated by components along x, just like the orientation of the optical emitter; besides, for alternating-sign doping, the LDOS divergence extends over the entire region of vanishing doping, following the same behavior of the SPP mode at the point H as observed in Fig. 2.12(f). The graphene decay rate used here is again $\gamma = 0.01\omega_0'''$.

2.5 Conclusions

In the first section of this chapter, we have introduced a new practical method to describe accurately the electrostatic plasmonic response of interacting uniformly doped graphene nanoribbons based on the plasmon wave function of an individual island (*i.e.*, magnitude proportional to the induced charge density associated with the plasmon). We have shown that our model constitutes a natural extension of the dipole-dipole interacting model but with a better degree of accuracy, especially at short distances between the edges of the nanostructures. Although we have limited our analysis to different arrangements of graphene nanoribbons (*e.g.*, dimers, arrays, and bilayer arrays), our model can be easily adapted to complex 2D geometries of other 2D plasmonic materials and also incorporate more plasmon modes in each nanostructure.

In the second section, we have investigated the classical effects of inhomogeneities in diverse doping distributions in graphene nanoribbons. In particular, we have focused on three different electrostatic doping configurations: backgated ribbons, co-planar ribbon pairs placed at opposite potentials, and individual ribbons subject

to a uniform electric field. In the first two cases, we have found that the plasmon frequencies and the induced charge densities are very similar to those of uniformly doped nanoribbons for the same value of the average Fermi energy $\langle|E_{\mathrm{F}}|\rangle$. However, when a uniform electric field is used to dope graphene, an interesting scenario opens where plasmons present very different characteristics, *e.g.*, distinct plasmonic dispersion to the uniformly doped case and induced charge densities piling up near the center of the ribbon. This charge accumulation can offer an additional handle to engineer graphene plasmon modes. Our study is based on the interaction of multiple dipoles spread all over the ribbon area, and can be straightforwardly extended to other doping configurations of graphene nanoribbons or different geometries of even diverse 2D plasmonic materials which could be useful for the design of future optoelectronic devices.

In section (2.3), we have continued with the classical study of electrostatic inhomogeneous doping, but focused on graphene nanodisks. We have found again that the plasmon frequency and the induced charge density for inhomogeneous doping under a uniform potential behave similarly as in the uniform doping case for the same value of $\langle|E_{\mathrm{F}}|\rangle$. Conversely, different behavior is observed when we have neutral nanodisks exposed to a neighboring external charge. We have found regions inside the nanodisks with a huge concentration of induced charge density near to the points of vanishing doping, in a similar manner as the ribbons under uniform electric field described in section (2.2.3). Moreover, here the plasmon frequencies differ considerably from the uniform doping configuration, particularly for the monopolar mode and more remarkably when the distance between the external charge and the disk is smaller than the disk radius. Remarkably, we have shown that a single electron is sufficient to excite a plasmon so that this doping configuration could enable the optical sensing of atoms and ions.

Finally, we have explored in section (2.4) a new way of doping electrostatically extended graphene through a periodic distribution of equally-signed or alternately-signed point charges. Under these patterned conditions, we have observed that the radiative decay rate of an optical emitter close to graphene can be boosted via the divergences in the LDOS associated with Van Hove singularities of the plasmonic bands. The radiated energy is almost entirely converted into graphene SPPs, which are eventually dissipated inelastically as heat or by the creation of e-h pairs.

Chapter 3

Quantum nonlocal effects in nanoribbons

As introduced in section (1.4.2), the plasmonic response of doped graphene is influenced by nonlocal and quantum finite-size effects when the characteristic size of the island is $\lesssim \lambda_F$, and therefore, classical electromagnetism loses its validity. More specifically, upon the inclusion of a quantum-mechanical TB-RPA description, substantial differences in the LSP (renamed as "plasmon" for simplicity throughout this chapter) frequencies and broadening appear up to sizes of $\sim 10\,\mathrm{nm}$ in nanoribbons and $\sim 20\,\mathrm{nm}$ in nanodisks [40]. Besides, the broadening of the resulting plasmon is very sensitive to the type of edge termination [*i.e.*, armchair (AC) or zigzag (ZZ); see right inset of Fig. 3.1]. Following the mentioned in section (1.5.3), ZZ-edged nanostructures possess a band of zero-energy modes containing surface states populating the edge termination (*i.e.*, electronic edge states) [20]. Thus, when plasmons dissipate, if their energy is higher than the Fermi level [101], a strong quenching emerges due to coupling with these zero-energy edge states [40, 80, 84].

In this chapter, we study quantum nonlocal effects observable in the lowest-order dipolar plasmons sustained by individual and interacting graphene nanoribbons. For our purpose, we use the quantum TB-RPA model presented in section (1.4.2) and consider $D = 6\,\mathrm{nm}$ wide self-standing uniformly-doped nanoribbons at $T = 300\,\mathrm{K}$ where we distinguish between AC or ZZ edge terminations. Besides, we compare our results with classical full-numerical calculations following the description given in

section (2.1), where the edge configuration is irrelevant. Remarkably, the dielectric response of the carbon layer in this classical approach is taken from the local-RPA approximation [see Eq. (1.18)]. We show that quantum nonlocal effects can occur in individual nanoribbons and affect the hybridization of plasmons in co-planar parallel dimers [41] and arrays for small edge-to-edge separations. These results, in combination with other interesting properties studied in this chapter, support the idea of the implementation of graphene nanoribbons as electro-optical modulators and switchers in the NIR regime.

3.1 Individual nanoribbons

We start by analyzing plasmons in individual nanoribbons, as depicted in Fig. 3.1. Here, we plot the extinction cross-section under normal incidence normalized to the graphene area for light polarized perpendicular to the nanoribbon edges (see left inset). This magnitude is obtained from the polarizability as the sum of the expressions given in Eq. (1.30). We compare the results from the quantum-mechanical model (*i.e.*, blue and red curves) with the numerical solutions of full-retarded Maxwell's equations (*i.e.*, black curves) obtained with BEM [see section (1.4.1)].

We study three different doping levels $E_{\mathrm{F}} = 0.4, 1$, and $1.5\,\mathrm{eV}$, with a constant intrinsic decay rate of $\hbar\gamma = 20\,\mathrm{meV}$. We observe that classical plasmons are generally redshifted but in excellent quantitative agreement with the results from our quantum TB-RPA model when the plasmon energy is below the Fermi level (*i.e.*, $E_{\mathrm{F}} = 1\,\mathrm{eV}$ and $1.5\,\mathrm{eV}$). If this condition is not satisfied (*i.e.*, $E_{\mathrm{F}} = 0.4\,\mathrm{eV}$), plasmons in ZZ-edged nanoribbons (blue curves) are strongly quenched by the excitation of the edge states mentioned above. Moreover, for the AC termination (red curves), the plasmons are slightly blueshifted and broadened by the effect of nonlocalities. This behavior is reproducible over a large range of doping levels, with Fig. 3.1 acting as a representative example.

Additionally, the plasmon frequencies increase with E_{F} following the approximate behavior given in section (1.5.4) for the nanoribbons $\hbar\omega_{\mathrm{p}} \approx 4e\sqrt{[2/(\varepsilon_1+\varepsilon_2)]\,E_{\mathrm{F}}/\pi D}$, where we assume as dominant the lowest-order dipolar mode, and $\varepsilon_1 = \varepsilon_2 = 1$. Although this expression is derived assuming the Drude model, within the local-RPA approach the plasmon energies are just slightly redshifted, as plotted in Fig. 1.9(a).

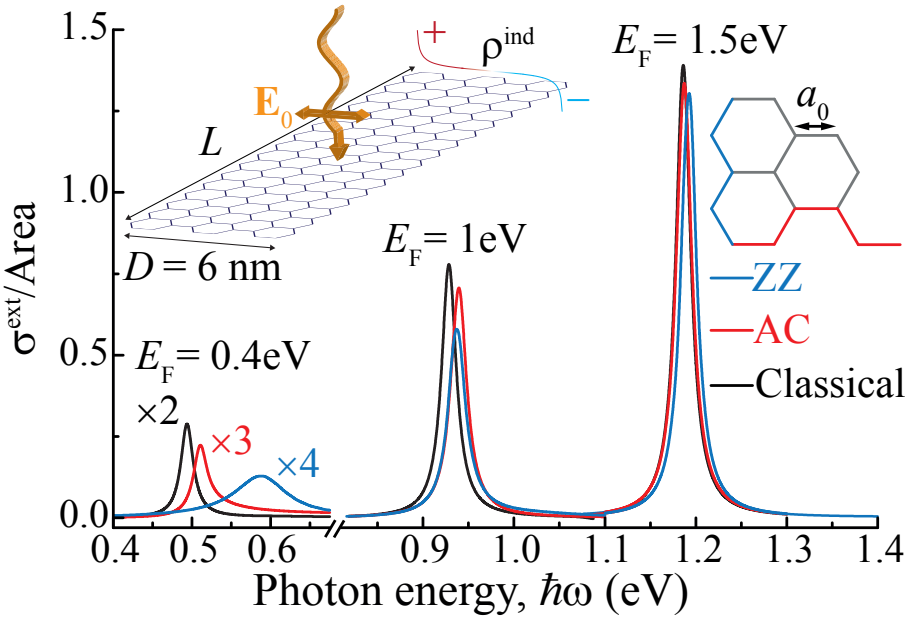

Figure 3.1: Comparison between quantum and classical plasmons sustained by individual graphene nanoribbons. We plot the normal-incidence extinction cross-section normalized to the graphene area of a self-standing nanoribbon (width $D = 6\,\text{nm}$ and intrinsic decay rate $\hbar\gamma = 20\,\text{meV}$) for several values of the Fermi energy E_F. These results are obtained using (i) classical theory (black curves) using BEM [see section (1.4.1)] with the local-RPA conductivity [see Eq. (1.18)], and (ii) a quantum TB-RPA model [see section (1.4.2)]. In this quantum formalism, we find a solution for either zigzag (blue curves) or armchair (red curves) edges as illustrated in the right inset, where $a_0 = 1.421\,\text{Å}$ is the carbon-to-carbon bond distance [see section (1.3.2)]. We focus on the lowest-order dipolar mode (see induced charge density in the left inset), which is excited by light polarized across the ribbon. The figure is adapted from Ref. [101].

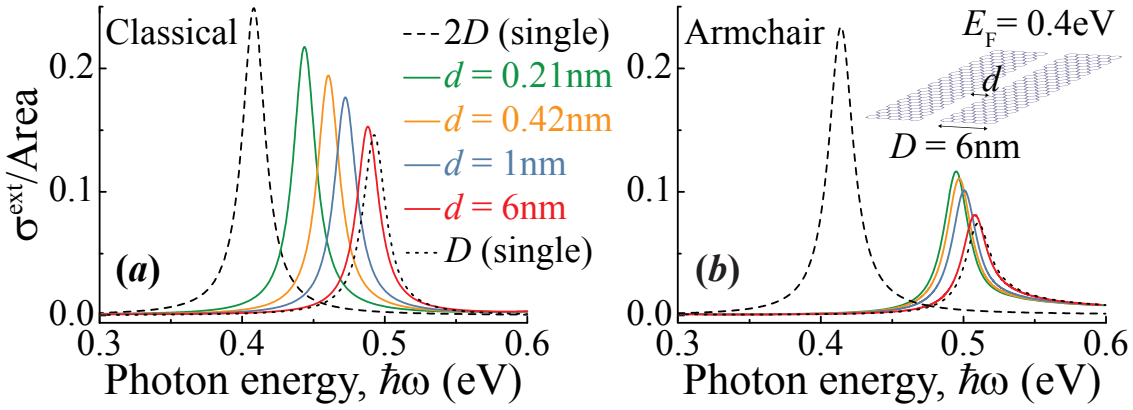

Figure 3.2: Normal-incidence classical (a) and AC-edged quantum TB-RPA (b) calculations of the extinction cross-sections of nanoribbon dimers. The width, Fermi energy, and intrinsic decay rate are $D = 6\,\text{nm}$, $E_\text{F} = 0.4\,\text{eV}$, and $\hbar\gamma = 20\,\text{meV}$, respectively. Each spectrum corresponds to different carbon-to-carbon edge separations d as shown in the inset of panel (b) [see Fig. 3.3(b) for the relation of this parameter to the edge-to-edge distance in the classical model]. The spectra for individual nanoribbons of widths D and $2D$ are depicted as dotted and dashed curves, respectively. The light polarization is the same as in Fig. 3.1. The figure is adapted from Ref. [101].

3.2 Dimers of co-planar nanoribbons

We know from section (2.1) that two doped co-planar parallel nanoribbons separated a carbon-to-carbon (C-C) edge distance d can interact, thus producing significant changes in the plasmonic response of the whole system. We study this scenario in Fig. 3.2 with a dimer of identical nanoribbons of width $D = 6\,\text{nm}$ and Fermi level $E_\text{F} = 0.4\,\text{eV}$. Here we compare classical simulations [panel (a)] with quantum-nonlocal AC-edged calculations [panel (b)]. For the latter, the implementation of a finite number of nanoribbons in our quantum TB-RPA model is straightforward. In the case of dimers (and also more generally for an array), we use the 1D periodicity of the graphene atomic lattice is order to reduce the calculation to a finite number of sites (l and l' indices) within a unit cell [41]. The single-ribbon susceptibility is the same as in Eq. (1.20), but we need to supplement the Coulomb interaction $v_{ll'}$ with the sum of all interactions of site l with the equivalent l' sites in other

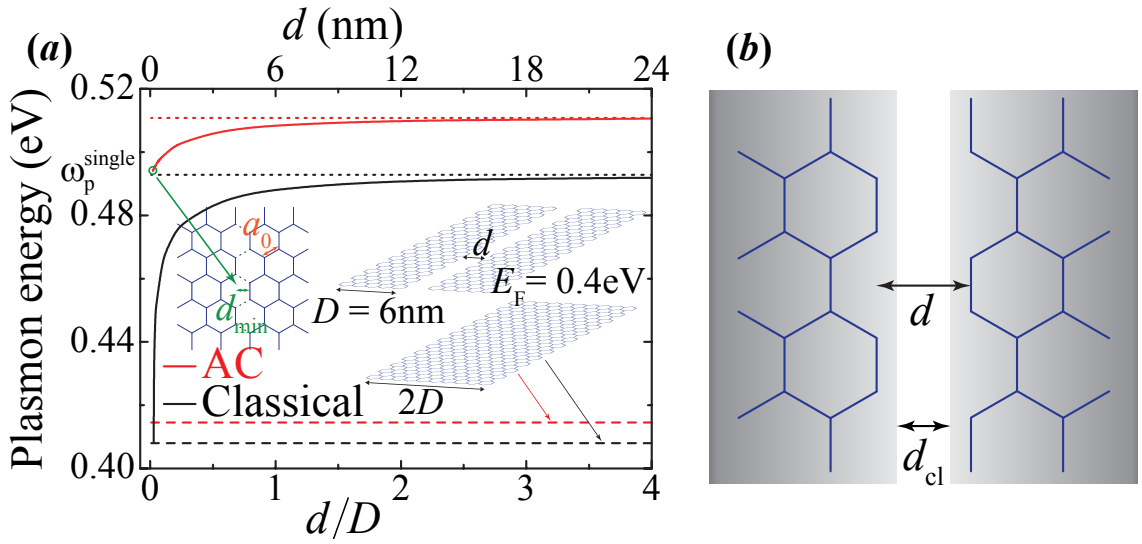

Figure 3.3: Evolution of the plasmon energy with the separation distance in co-planar armchair-edged dimers of graphene nanoribbons. (a) We represent the plasmon peak energies of Fig. 3.2 as a function of the carbon-to-carbon edge distance d using classical and quantum-mechanical (for AC nanoribbons) models. The classical calculations [*i.e.*, the black solid curve also plotted in Fig. 2.3(a)] converge well to the double-width-ribbon (see lower right inset) limit for $d \ll D$ (black dashed line), in contrast to the quantum TB-RPA curve, which predicts a substantial energy gap. The left inset illustrates the nearest separation $d_{\rm min} = \sqrt{3}a_0/2$ considered for the quantum AC calculations. (b) Scheme of the notation used for the separation distance between nanoribbons; classical calculations are performed with a separation given by $d_{\rm cl} = d - d_{\rm min}$. The figure is adapted from Ref. [101].

ribbons. The resulting effective polarizability per unit length ($L \to \infty$) is then given by $\widetilde{\alpha}(\omega)/L = \sum_l x_l\, \rho_l^{\rm ind}(\omega) / \left(E_0\, b\right)$, where the sum extends over the noted unit cell of length b along the nanoribbon, x_l is the distance across it, $\rho^{\rm ind}(\omega)$ is the induced charge density, and E_0 is the external electric field per unit area used in our formalism (*i.e.*, $\Phi_l^{\rm ext} = -x_l E_0$).

From Fig. 3.2 we observe at first glance that, accordingly to the results presented in Fig. 2.2(a), the interaction is attractive leading to redshifts. However, the sequence of spectra clearly shows that the discrepancy between classical and quantum calculations boosts at short distances d between the nanoribbons. This is consistent with the intuitive idea that the influence of nonlocal effects is higher at

short distances [136]. As part of this behavior, we find from panel (a) that classical simulations of the dimer converge smoothly to the double-width single-ribbon limit (black dashed curve), in contrast to quantum calculations. This singular effect is more remarkable in Fig. 3.3(a), where we plot the evolution of the dimer plasmon energy with d. As we see, a sizeable jump appears between the plasmon of an AC single-ribbon with double-width and the dimer separated the minimum possible distance $d_{\rm min} = \sqrt{3}a_0/2$ (with $a_0 = 1.421\,\text{Å}$ as the C-C bond distance) when a row of C-C bonds is removed (*i.e.*, the TB hopping between electrons of different ribbons is set to zero). These removed bonds are depicted within dashed lines in the left inset of Fig. 3.3(a). Interestingly, the classical calculations for the dimers [same black solid curve as in Fig. 2.2(a)], match the double-width nanoribbon plasmon at very small distances.

Incidentally, since the nanoribbon edges are generally passivated with hydrogens, and considering the C-H and H-H bond distances, we estimate that only carbon-to-carbon edge distances $\gtrsim 0.3\,\text{nm}$ are realistic, with well-separated and non-tunneling electronic states in each nanoribbon. We include smaller distances for tutorial purposes and, in particular, $d_{\rm min}$ in AC nanoribbons to study the effect of removing one row of C-C bonds, as discussed above. The relation between the separation distances d for both the classical and quantum calculations is explained in the caption of Fig. 3.3(b).

3.3 Arrays of co-planar nanoribbons

We compare in Fig. 3.4 the absorbance for normal-incidence light of a co-planar array of nanoribbons with AC [panels (a) and (b)] and ZZ edges [panels (c) and (d)], respectively. The absorbance is here calculated assuming s polarization, whereas the reflection coefficient of the array is obtained from Eq. (2.12), and it can be safely reduced to $\widetilde{r}_s \approx (2\pi \mathrm{i} k/a)\,[\widetilde{\alpha}(\omega)/L]$, where $a = D + d$ is the period of the array.

The resulting spectra for diverse periodicities exhibit again a high sensitivity to ZZ edges when the plasmon energies are above the Fermi level, leading to a significant reduction of absorption and increasing plasmon broadening [cf. panels (a) and (c)]. At higher doping [panels (b) and (d)], plasmon broadening is limited to the intrinsic damping (*i.e.*, $\hbar\gamma = 20\,\text{meV}$) in both AC and ZZ ribbon arrays. Interestingly, the

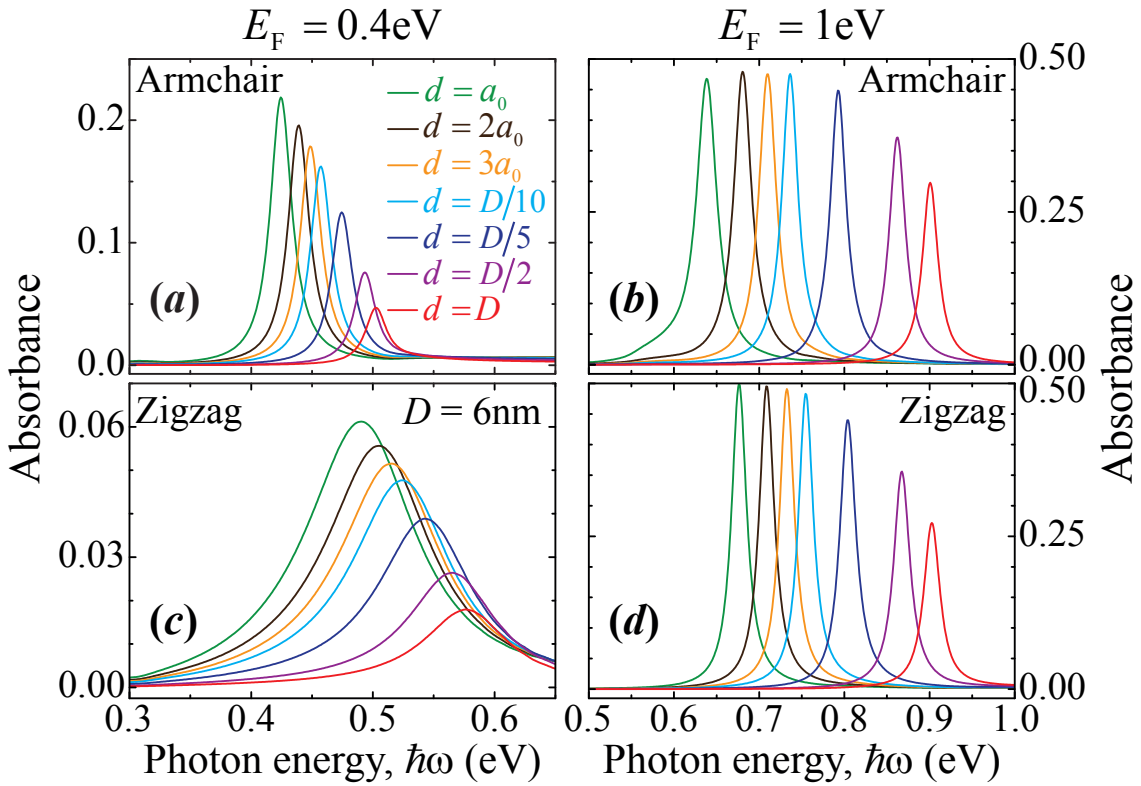

Figure 3.4: Absorbance under normal incidence of s polarized light [see Eq. (2.14)] by a co-planar array of graphene nanoribbons with AC [panels (a) and (b)] and ZZ [panels (c) and (d)] edges calculated from our quantum TB-RPA model for two different Fermi energies (see upper labels) and various carbon-to-carbon edge separations d. The nanoribbon width and intrinsic decay rate are the same as in Fig. 3.1. The figure is adapted from Ref. [101].

inter-ribbon interaction is smaller with ZZ edges, as revealed by the larger redshift in AC nanoribbons at narrow separations d. In all cases, equivalently to the classical results presented in section (2.1), these energy shifts are larger than in dimers [cf. for example Figs. 3.2(b) and 3.4(a)]. Remarkably, the maximum possible absorption of 50% is reached with ZZ edges in panel (d) at separations of the order of the C-C bond distance.

3.4 Conclusions

In this chapter we have shown that quantum nonlocal effects in narrow graphene nanoribbons exhibit the following general properties: (i) plasmons are quenched by ZZ edges, and they decay through excitation of electronic edge states, when the energy of the formers are above the Fermi level; (ii) quantum nonlocal effects (generally identified as blueshifts) increase with decreasing nanoribbon width, although a classical electromagnetic description produces reasonable results for individual nanoribbons of widths down to a few nanometers; (iii) nonlocal effects are important in interacting nanoribbons at short separations, leading to substantial blueshifts in the lowest-order dipolar plasmons of closely spaced dimers, in contrast to classical theory, which predicts a smooth convergence towards the double-width nanoribbon; (iv) remarkably, the removal of a single row of atoms produces a dramatic increase in the plasmon energy, observed both in dimers and in arrays; and (v) our realistic quantum-mechanical calculations yield plasmon energies that are pushed up to the NIR regime for nanoribbon widths of a few nanometers, similar to those that can be synthesized by chemical self-assembly [108].

Our results provide a solid theoretical background for understanding the plasmonic response of single and interacting graphene nanoribbons, where important quantum nonlocal effects must be considered in the design of potential device applications in the NIR regime.

Chapter 4

Nonlinear optical effects

Nonlinear optics studies the phenomena related with the nonlinear response of a material to an external electric field [137]. In the case of doped graphene nanostructures, due to its unique electronic band structure, a strong nonlinear optical response [75, 77, 138, 139, 140, 141, 142, 143, 144, 145, 146] can emerge exceeding that of conventional nonlinear materials. Moreover, nonlinearities can be further enhanced by interband e-h transitions, finite temperatures, and LSPs (renamed as "plasmons" for simplicity) [78, 80, 81, 147, 148, 149, 150, 151].

In previous chapters, all the results have been obtained under the assumption of a linear optical response. Now, we study in detail the nonlinear optical response of doped graphene nanostructures which can act as plasmon-driven nonlinear enhancers. We start our analysis by briefly explaining the properties of three of the main nonlinear processes: second-harmonic generation (SHG), third-harmonic generation (THG), and Kerr effect. Then, we concentrate on describing the classical nonlinear conductivities and polarizabilities of doped graphene through the Boltzmann transport equation (BTE), where only intraband transitions are considered [18, 75, 81, 144, 147, 152], and we compare our results with a quantum-mechanical approach that implements nonlocal, finite-size, and edge-termination effects in combination with interband transitions. Finally, we show that these features play an important role in the nonlinear response observable in the plasmons sustained on nanostructures with a characteristic size $D \sim 10 - 20\,\mathrm{nm}$.

4.1 Description of nonlinear optical effects

In doped graphene, the dipole moment per unit area or polarization $\mathbf{P}(\omega)$ depends on the external ac field $\mathbf{E}^{\rm ext}(\omega) = \mathbf{E}_0\,(\mathrm{e}^{-\mathrm{i}\omega t} + \mathrm{e}^{\mathrm{i}\omega t})$ associated with an incident monochromatic plane wave at frequency ω as [137]

$$\begin{aligned}\mathbf{P}(\omega) &= \chi^{(1)}(\omega)\,\mathbf{E}^{\rm ext}(\omega) + \chi^{(2)}(\omega)\,\mathbf{E}^{\rm ext\,2}(\omega) + \chi^{(3)}(\omega)\,\mathbf{E}^{\rm ext\,3}(\omega) + \ldots \\ &\equiv \mathbf{P}^{(1)}(\omega) + \mathbf{P}^{(2)}(\omega) + \mathbf{P}^{(3)}(\omega) + \ldots,\end{aligned} \tag{4.1}$$

where the quantity $\chi^{(1)}(\omega)$ is known as the linear susceptibility, while $\chi^{(2)}(\omega)$, and $\chi^{(3)}(\omega)$ are the second- and third-order susceptibilities, respectively. Additionally, we name $\mathbf{P}^{(1)}(\omega) = \chi^{(1)}(\omega)\,\mathbf{E}^{\rm ext}(\omega)$ as the linear polarization, which is related to conventional (linear) optics, with $\mathbf{P}^{(2)}(\omega) = \chi^{(2)}(\omega)\,\mathbf{E}^{\rm ext\,2}(\omega)$ and $\mathbf{P}^{(3)}(\omega) = \chi^{(3)}(\omega)\,\mathbf{E}^{\rm ext\,3}(\omega)$ as the second- and third-order nonlinear polarizations. If we define the areal density of carbon atoms in graphene as [80] $n_{\rm C} = 3.8 \times 10^{15}\,\mathrm{cm}^{-2}$, we can express directly the nth-order polarizability as $\alpha^{(n)}(\omega) = n_{\rm C}\,\chi^{(n)}(\omega)$. The conversion factors from esu (electrostatic units) to SI of $\alpha^{(n)}(\omega)$ are given in Table 4.1.

Remarkably, the nonlinear physical processes derived from $\mathbf{P}^{(2)}(\omega)$ are different to those arising from $\mathbf{P}^{(3)}(\omega)$. Moreover, second-order nonlinearities cannot occur in centrosymmetric nanostructures [137] (*i.e.*, systems with an inversion symmetry center). Finally, we need to *quantize* the effects of nonlinear processes in doped graphene. If we take $\chi^{(1)}(\omega)$ of the order of unity, we find [153] $\chi^{(2)}(\omega) \approx 10^{-5}\,\mathrm{esu}$ and $\chi^{(3)}(\omega) \approx 10^{-8}\,\mathrm{esu}$, which are much higher than the predicted values in standard nonlinear materials [137] [$\chi^{(2)}(\omega) \approx 10^{-8}\,\mathrm{esu}$ and $\chi^{(3)}(\omega) \approx 10^{-15}\,\mathrm{esu}$].

Polarizability	**esu**	**SI**
$\alpha^{(1)}(\omega)$	$1\,\mathrm{cm}^3$	$1.113 \times 10^{-16}\,\mathrm{C}^2\,\mathrm{m}^{\,2}\,\mathrm{J}^{\,-1}$
$\alpha^{(2)}(\omega)$	$1\,\mathrm{cm}^5\,\mathrm{statC}^{\,-1}$	$3.711 \times 10^{-21}\,\mathrm{C}^3\,\mathrm{m}^{\,3}\,\mathrm{J}^{\,-2}$
$\alpha^{(3)}(\omega)$	$1\,\mathrm{cm}^7\,\mathrm{statC}^{\,-2}$	$1.238 \times 10^{-25}\,\mathrm{C}^4\,\mathrm{m}^{\,4}\,\mathrm{J}^{\,-3}$

Table 4.1: Polarizability unit conversion factors (esu, electrostatic units).

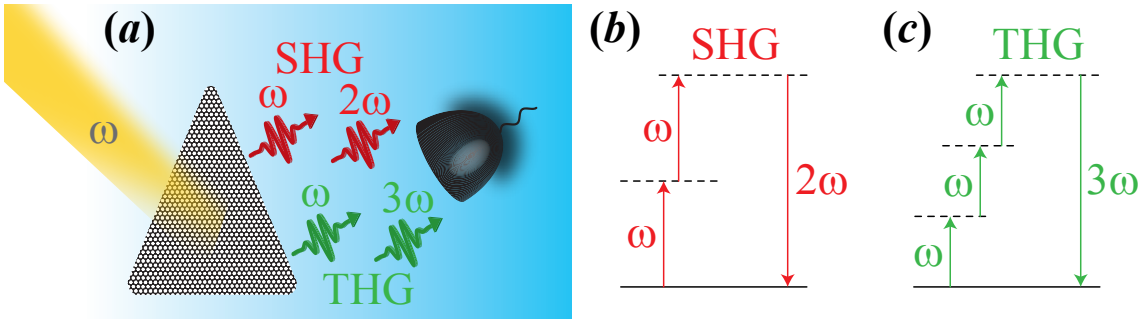

Figure 4.1: Second- and third-harmonic generation by a graphene nanoisland. (a) Scheme of the geometry for the SHG (red arrows) and THG (green arrows). Here, a graphene nanoisland is illuminated by a high-intensity laser beam at frequency ω (yellow beam) and the resulting emitted harmonic waves are collected by the photon detector. (b),(c) Energy-level diagram describing the SHG [panel (b)] and THG processes [panel (c)], respectively. The solid horizontal line represents the ground state while the dashed lines correspond to virtual states. The figure is adapted from Ref. [81].

4.1.1 Second-harmonic generation

We start our general analysis of the nonlinear effects by qualitatively describing the second-harmonic generation process. According to Eq. (4.1), the modulus of the second-order polarization can be rewritten as

$$P^{(2)}(\omega) = 2\chi_0^{(2)}(\omega)E_0^2 + \chi_{2\omega}^{(2)}(\omega)E_0^2\left(\mathrm{e}^{-2\mathrm{i}\omega t} + \mathrm{e}^{2\mathrm{i}\omega t}\right). \tag{4.2}$$

The first term after the equal sign corresponds to a contribution at zero frequency (detailed in the subindex of the susceptibility), which does not lead the re-emission of any photon. Thus, a static electric field may arise inside graphene. This process is known as "optical rectification". On the other hand, the second term after the equal sign corresponds to a contribution at the double frequency of the incident light, so that a photon at the second-harmonic frequency 2ω can be generated. The corresponding energy-level diagram is depicted in Fig. 4.1(b). Here, two photons at frequency ω impinging over a triangular graphene nanoisland [see Fig. 4.1(a)] are converted into a photon of frequency 2ω in a single quantum-mechanical process with two virtual states involved. Besides the generation of a second-harmonic, the main

re-emission of photons from graphene occurs at frequency ω due to the dominant linear response. Interestingly, this nonlinear optical mechanism is commonly used in lasers for doubling the frequency of their fundamental mode such as in solid-state lasers (*e.g.*, Nd:YAG lasers operate at $\lambda = 1064\,\text{nm}$ and by SHG we can obtain the typical green-colored emission at 532 nm).

4.1.2 Third-harmonic generation and Kerr effect

Now we focus on the full expression of the third-order polarization. For simplicity, in this case we consider a monochromatic external ac field $\mathbf{E}^{\text{ext}}(\omega) = \mathbf{E}_0 \cos(\omega t)$. Therefore, we have

$$P^{(3)}(\omega) = \frac{1}{4}\chi^{(3)}_{3\omega}(\omega)E_0^3 \cos(3\omega t) + \frac{3}{4}\chi^{(3)}_{\omega}(\omega)E_0^3 \cos(\omega t). \tag{4.3}$$

Analogously to what it is detailed in section (4.1.1), the first term in Eq. (4.3) after the equal sign corresponds to a contribution at frequency 3ω. Namely, three photons at frequency ω are destroyed, and a third-harmonic is generated. Fig. 4.3(c) describes the energy-level diagram of the process.

On the other hand, the second term after the equal sign in Eq. (4.3) corresponds to a contribution at the same harmonic of the incident light. This nonlinear term contributes to the variation of the refractive index $n = \sqrt{\varepsilon}$ of the graphene nanostructure at high intensities. This process is commonly known as ac Kerr effect [154]. Hence, if we only consider the first-harmonic terms up to third-order, the graphene polarization from Eq. (4.1) at the incident frequency ω reads

$$\mathbf{P}_{\omega}(\omega) \approx \left[\chi^{(1)}_{\omega}(\omega) + \frac{3}{4}\chi^{(3)}_{\omega}(\omega)E_0^2\right]\mathbf{E}_0 \cos(\omega t). \tag{4.4}$$

If we take into account the relation given in Eq. (1.15) between the dielectric function ε and the local graphene conductivity $\sigma(\omega) = -\mathrm{i}\omega\chi(\omega)$, with $\chi(\omega) = \chi^{(1)}_{\omega}(\omega) + (3/4)\chi^{(3)}_{\omega}(\omega)E_0^2$, we can find straightforwardly the relation

$$n(\omega) \approx n_0(\omega) + \frac{3\pi}{2t\, n_0(\omega)}\chi^{(3)}_{\omega}(\omega)E_0^2, \tag{4.5}$$

where t is the graphene thickness and $n_0(\omega) = \sqrt{1 + 4\pi\chi^{(1)}_\omega(\omega)/t}$ is the linear refractive index. We observe that third-order nonlinearities introduce a linear dependence of the refractive index with the intensity of the external field.

4.2 Classical nonlinear optical conductivities

In this section we present an easy to handle way to obtain the nonlinear conductivities in graphene within the framework of classical electrodynamics [see section (1.4.1)]. More specifically, we assume the electrostatic where the characteristic size of our nanostructure fulfills $D \ll \lambda$. We use a unified approach based upon the BTE valid for extended graphene which describes the evolution of the doping carrier distribution function $f^{(n)}_{\mathbf{k}}(\mathbf{R}, t)$ of nth-order at position $\mathbf{R}$ and momentum $\mathbf{k}$. Within this theory $\mathbf{k}$ and $\mathbf{R}$ obey the classical equations of motion: $\dot{\mathbf{R}} = \mathbf{v}_{\mathbf{k}} = (1/\hbar)\partial\epsilon_{\mathbf{k}}/\partial\mathbf{k}$, and $\hbar\dot{\mathbf{k}}(\mathbf{R}, t) = -e\mathbf{E}(\mathbf{R}, t)$, where $\mathbf{E}(\mathbf{R}, t)$ is the sum of the external field $\mathbf{E}^{\text{ext}}(t)$ and the induced field $\mathbf{E}^{\text{ind}}(\mathbf{R}, t)$ generated by the extra charge carriers [see section (1.5.2)]. We focus in energy scales $\lesssim 1\,\text{eV}$, then the linearization of the graphene dispersion relation around the Dirac points given in Eq. (1.7) is fulfilled. Besides, we assume a temperature $T = 0$ and incident photon energies $\lesssim 2E_{\text{F}}$, so that interband e-h transitions can be neglected. Combining all the former conditions, the doping carrier dynamics are described by [153]

$$\frac{\partial}{\partial t} f^{(n)}_{\mathbf{k}}(\mathbf{R}, t) - \frac{e}{\hbar}\mathbf{E}(\mathbf{R}, t)\cdot\nabla_{\mathbf{k}} f^{(n)}_{\mathbf{k}}(\mathbf{R}, t) \pm v_{\text{F}}\hat{\mathbf{k}}\cdot\nabla_{\mathbf{R}} f^{(n)}_{\mathbf{k}}(\mathbf{R}, t) = \frac{-1}{\tau}\left[f^{(n)}_{\mathbf{k}}(\mathbf{R}, t) - f^{(0)}_{k}(\epsilon_k)\right] \tag{4.6}$$

where the right-hand side corresponds to scattering mechanisms, $f^{(0)}_{k}(\epsilon_k)$ is the Fermi-Dirac distribution [see Eq. (1.21)], and τ is the graphene relaxation time. Eq. (4.6) fully describes the microscopic dynamics of the doping carriers on which other macroscopic quantities are strongly related. For example, the surface current in graphene upon illumination of the external ac field given in section (4.1) can be expressed as [81]

$$\mathbf{J}^{(n)}(\mathbf{R}, t) = -e g_v g_s \int \frac{\mathrm{d}^2\mathbf{k}}{(2\pi)^2}\mathbf{v}_{\mathbf{k}}\, f^{(n)}_{\mathbf{k}}(\mathbf{R}, t). \tag{4.7}$$

where $g_v = g_s = 2$ are the valley and spin degeneracies. The nonlinear set of Eqs. (4.6) and (4.7) can be solved perturbatively in the Fourier space by expanding the wave

vector k in order to get the relation between $\mathbf{J}^{(n)}(\omega)$ and $\mathbf{E}(\omega)$ (*i.e.*, the linear and nonlinear conductivities). Interestingly, at zeroth-order expansion in k, the first-order or linear surface current remains

$$\mathbf{J}^{(1)}_{\omega}(\omega) = \frac{\mathrm{i}e^2}{\pi\hbar^2}\frac{E_{\mathrm{F}}}{\omega + \mathrm{i}\tau^{-1}}\mathbf{E}(\omega), \tag{4.8}$$

from which the local linear conductivity directly arises coinciding with that from the Drude model [see Eq. (1.16)].

For the second-order current, this model does not allow us to consider the effect of the fundamental frequency. However, in order to get the expression for the second-harmonic we have that the zeroth-order expansion in k vanishes [81], so that the dominant term is the first-order term which corresponds to a nonlocal contribution (*i.e.*, the current depends on the electric field gradient). Thus, we can find a expression for the second-harmonic (see Ref. [81] for a detailed derivation) given by

$$\begin{aligned} J^{(2)}_{2\omega,i}(\omega) &= \sigma^{(2)}_{2\omega,ijkl}(\omega)E_j(\omega)\nabla_k E_l(\omega) \\ &= \frac{3\mathrm{i}e^3 v_{\mathrm{F}}^2}{8\pi\hbar^2\left(\omega + \mathrm{i}\tau^{-1}\right)^3}\left[\frac{5}{3}\delta_{ij}\delta_{kl} - \delta_{ik}\delta_{jl} + \frac{1}{3}\delta_{il}\delta_{jk}\right]E_j(\omega)\nabla_k E_l(\omega), \end{aligned} \tag{4.9}$$

where $ijkl$ denote in-plane vector indexes, and δ_{ij} is the Kronecker delta. As a clarifying example, in the $z = 0$ graphene plane, for an ac electric field polarized along the $i \equiv x$ direction, we have

$$J^{(2)}_{2\omega,x}(\omega) = \frac{3\mathrm{i}e^3 v_{\mathrm{F}}^2}{8\pi\hbar^2\left(\omega + \mathrm{i}\tau^{-1}\right)^3}\left[E_x\left(\frac{\partial E_x}{\partial x} + \frac{5}{3}\frac{\partial E_y}{\partial y}\right) + E_y\left(\frac{1}{3}\frac{\partial E_x}{\partial y} - \frac{\partial E_y}{\partial x}\right)\right], \tag{4.10}$$

where for simplicity we omit the frequency dependence of the electric field components.

Similarly, we can calculate the contributions to the THG and Kerr effect. Here, the third-order currents are local (*i.e.*, the spatial variations in $f^{(3)}_{\mathbf{k}}(\mathbf{R}, t)$ are negligible). In the case of third-harmonic current we have [153]

$$J^{(3)}_{3\omega}(\omega) = \sigma^{(3)}_{3\omega}(\omega)E^3(\omega) = \frac{3\mathrm{i}e^4 v_{\mathrm{F}}^2}{4\pi\hbar^2 E_{\mathrm{F}}(\omega + \mathrm{i}\tau^{-1})(2\omega + \mathrm{i}\tau^{-1})(3\omega + \mathrm{i}\tau^{-1})}E^3(\omega), \tag{4.11}$$

and for the Kerr effect, the current reads [153]

$$J_{\omega}^{(3)}(\omega) = \sigma_{\omega}^{(3)}(\omega)E^{3}(\omega) = \frac{9\mathrm{i}e^{4}v_{\mathrm{F}}^{2}}{4\pi\hbar^{2}E_{\mathrm{F}}(\omega+\mathrm{i}\tau^{-1})(-\omega+\mathrm{i}\tau^{-1})(2\omega+\mathrm{i}\tau^{-1})}E^{3}(\omega). \quad (4.12)$$

Remarkably, the two former equations slightly differ from a previous study [146]. In fact, by neglecting the scattering term in Eq. (4.6), and redefining the external ac field as $\mathbf{E}^{\mathrm{ext}}(t) = \int_{-\infty}^{\infty} \mathrm{d}\omega\, \mathbf{E}_0 \exp(-\mathrm{i}\omega t + t/\tau)$, we recover the purely intraband expressions given in Ref. [146].

4.3 Classical nonlinear optical polarizabilities

The versatility of the electrostatic scaling law presented in section (1.5.4) enables us to directly obtain simple expressions for the nonlinear polarizabilities similar to that in Eq. (1.43) for the linear polarizability. First, we generalize the continuity equation from Eq. (1.14) considering nonlinearities at order n for the harmonic s as

$$\rho_{s\omega}^{\mathrm{ind}(n)}(\mathbf{R},\omega) = \frac{-\mathrm{i}}{s\omega}\nabla\cdot\mathbf{J}_{s\omega}^{(n)}(\mathbf{R},\omega). \quad (4.13)$$

We start by analyzing the second-order nonlinear polarizability for SHG processes. Here, we assume polarization along the in-plane direction i over a doped graphene nanostructure with size D and by implementing Eq. (4.10) into Eq. (4.13), we have

$$\rho_{2\omega,i}^{\mathrm{ind}\ (2)}(\omega) = -\eta_{2\omega}^{(2)}(\omega)\, D\, \nabla_i \left\{ \left[\frac{5}{3}\delta_{ij}\delta_{kl} - \delta_{ik}\delta_{jl} + \frac{1}{3}\delta_{il}\delta_{jk} \right] E_j(\omega)\nabla_k E_l(\omega) \right\}, \quad (4.14)$$

where we define, in an analogous manner to Eq. (1.36), the second-order parameter

$$\eta_{2\omega}^{(2)}(\omega) = \frac{\mathrm{i}}{2\omega D}\frac{3\mathrm{i}e^{3}v_{\mathrm{F}}^{2}}{8\pi\hbar^{2}\left(\omega+\mathrm{i}\tau^{-1}\right)^{3}}. \quad (4.15)$$

If we now consider (i) the dimensionless coordinate $\theta = i/D$, (ii) the change of variables given in Eq. (1.38), (iii) the approximation of dominant lowest-order dipolar mode $j = 1$ [see section. (1.5.4)], and (iv) Eqs. (2.3) and (2.4) for a single nanostruc-

ture ($l = 1$), we can express the second-order dipole moment as

$$p^{(2)}_{2\omega,\theta}(\omega) = -\eta^{(2)}_{2\omega}(\omega)\, D^2 d_1^2(\omega)\, \xi_2, \tag{4.16}$$

where

$$\xi_2 = \frac{1}{D\, d_1^2(\omega_1)} \int i\, \mathrm{d}^2\mathbf{R}\, \nabla_i \left\{ \left[\frac{5}{3}\delta_{ij}\delta_{kl} - \delta_{ik}\delta_{jl} + \frac{1}{3}\delta_{il}\delta_{jk} \right] E_j(\omega_1) \nabla_k E_l(\omega_1) \right\}, \tag{4.17}$$

is a dimensionless coefficient obtained at the frequency of the lowest-order mode ω_1. Analogously to the fitting coefficients η_1 and ξ_1 presented in section (1.5.4), ξ_2 only depends on the specific geometry considered and can be calculated once and for all specific sizes, doping level, and dielectric environment. Finally, implementing Eq. (4.16) into Eq. (4.1), we attain an electrostatic scaling-law for the second-order polarizability

$$\alpha^{(2)}_{2\omega}(\omega) = \frac{-\eta^{(2)}_{2\omega}(\omega)\, D^2 \xi_1^2 \xi_2}{\left[1 - \eta(\omega)/\eta_1\right]^2}, \tag{4.18}$$

where $\eta(\omega)$ is given by Eq. (1.36). Note that for nanoribbons, the second-order polarizability is per unit length, where $L \to \infty$ is the ribbon length, so that on the right-hand side of Eq. (4.18), the dependence with D is linear. Furthermore, under our assumptions of negligible interband e-h transitions and $T = 0$, we have ${\alpha_{2\omega}}^{(2)}(\omega) \propto D^2 E_{\mathrm{F}}^{-1}$.

Using the same formalism, at third-order the polarizability readily leads to

$$\alpha^{(3)}_{s\omega}(\omega) = \frac{\eta^{(3)}_{s\omega}(\omega)\, D^3 \xi_1^3 \xi_3}{\left[1 - \eta(\omega)/\eta_1\right]^3}, \tag{4.19}$$

where $\eta^{(3)}_{s\omega}(\omega) = \mathrm{i}\sigma^{(3)}_{s\omega}(\omega)/s\omega$ encloses the dependence on the nonlinear conductivity for $s = 1$ (Kerr) and $s = 3$ (THG), respectively. Moreover, we have ${\alpha_{s\omega}}^{(3)}(\omega) \propto D^{5/2} E_{\mathrm{F}}^{-3/2}$ and the dimensionless coefficient

$$\xi_3 = \frac{1}{D^2\, d_1^3(\omega_1)} \int i\, \mathrm{d}^2\mathbf{R}\, \left\{ \nabla_i E_i^3(\omega_1) \right\}. \tag{4.20}$$

4.4 Comparison classical-quantum nonlinear effects

In this section we compare the classical nonlinear response of nanostructured doped graphene using the formalism presented in sections (4.2) and (4.3) with a quantum-mechanical TB-RPA treatment similar to that given in section (1.4.2) and explained in detail elsewhere [153] that includes interband e-h transitions, in combination with finite-size, nonlocal, and edge effects at a temperature $T = 300\,\mathrm{K}$. Here, we focus our study on self-standing triangular graphene nanoislands with $D \sim 10\,\mathrm{nm}$ although more extended results for bigger sizes and even for other geometries like nanoribbons are detailed in Ref. [153]. The choice of a triangular shape permits us to use straightforwardly the electrostatic scaling law formalism for the classical linear, second- and third-order nonlinear polarizabilities [see Eqs. (1.43), (4.18), and (4.19)] and also to study islands containing either AC or ZZ edges [see Fig. 4.2(b)]. Furthermore, we compare the contributions to the lowest-order dipolar mode sustained by the graphene island excited by normal-incident illumination with an electric ac field polarized as the yellow arrow in Fig. 4.2(a).

For the classical calculations, the fitting coefficients η_1, ξ_1, ξ_2, and ξ_3 are computed once using the commercial finite-difference code COMSOL®. We assume a local dielectric function [see Eq. (1.15)] where the linear conductivity is obtained from the Drude model [see Eq. (1.16)] and the graphene thickness $t = 0.5\,\mathrm{nm}$ is well converged with respect to the $t \to 0$ limit. For our triangular nanoislands we find $\eta_1 \approx -0.093$, $\xi_1 \approx 0.541$, $\xi_2 \approx 0.117 - \mathrm{i}0.006$, and $\xi_3 \approx 0.916 + \mathrm{i}0.022$. In the case of nanoribbons, we have [153] $\eta_1 \approx -0.071$ and $\xi_1 \approx 0.951$ for linear order [which are in good agreement with the purely analytical values presented in section (1.5.4) and also with those given in section (2.1)], and $\xi_3 \approx 1.297 + \mathrm{i}0.0362$. Note that since the nanoribbon is a centrosymmetrical structure, $\alpha^{(2)}_{2\omega}(\omega) = 0$.

The spectra shown in Figs. 4.2(c)-(f) display the evolution of the dipolar plasmon assuming either a linear [panel (c)] or nonlinear [panels (d)-(f)] optical response for different doping levels E_F of the graphene nanoisland [see the color code in panel (c)]. The intrinsic damping rate is $\hbar\gamma = 50\,\mathrm{meV}$. At first glance, we observe in these four panels that, unlike the case of nanoribbons shown in Fig. 3.1, for low doping the

classical plasmons (filled curves) are blueshifted in comparison with the ones from the quantum model (solid curves for AC and dashed curves for ZZ edges). This is because in the classical approach we are assuming only intraband e-h transitions and also $T = 0$ (*i.e.*, Drude model for the linear response), and thus, they present the same behavior as in Fig. 1.9(a). In Fig. 4.2(c) we plot the linear absorption cross-section [see Eq. (1.30)] normalized to the triangle area. At low levels of doping when $\hbar\omega_{\rm p} > E_{\rm F}$ we find dramatic differences between the classical and quantum curves, similarly to the results observed in Chapter 3 for nanoribbons. Moreover, we also find that ZZ curves are more quenched than in the AC-edged case due to the presence of electronic edge-states. However, despite the enhancement of $E_{\rm F}$, the spectra of ZZ-edged nanotriangles preserve a remarkable smaller amplitude.

The results of the second-order nonlinear polarizability associated with SHG are plotted in Fig. 4.2(d). We observe that classical theory clearly underestimates the nonlinear response compared with the quantum-mechanical treatment, which implies that nonlocal and finite-size effects dominate in the SHG. This happens because the classical description relies only on nonlocal effects over extended graphene. Conversely, the quantum approach is not limited by this geometrical handicap and also accounts for the responses of both fundamental and second-harmonic frequencies, which significantly enhances the SHG [80].

Finally, the third-order nonlinear polarizabilities regarding THG and Kerr effect are depicted in Figs. 4.2(e) and (f), respectively. For the THG, we find reasonable agreement between classical and quantum approaches, especially at high levels of doping. However, for the Kerr effect the classical curves are significantly smaller except for very low doping. Remarkably, both for THG and Kerr effect, the ZZ-edged nanoislands are strongly quenched at any doping level. This behavior is not found in nanoribbons at high levels of doping [153], where the ZZ spectra converge to the AC-edged curves. Furthermore, the slightly better agreement between classical and quantum calculations for THG in comparison to SHG can be explained by the fact that the main contribution to the third-order conductivity is local. Finally, in the Kerr effect, the four oscillating waves at the fundamental frequency can be enhanced by the graphene plasmon. This enhancement is not considered in the classical description, resulting in a significantly weaker Kerr effect.

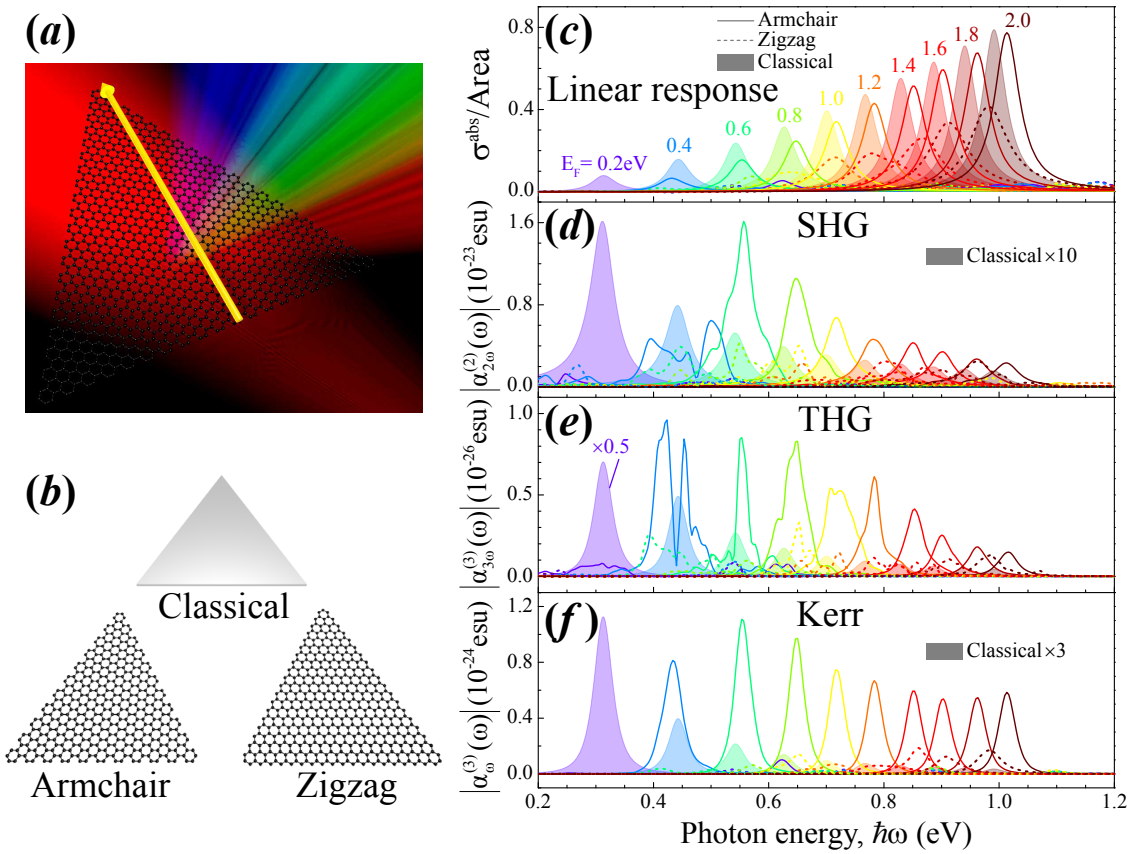

Figure 4.2: Linear and nonlinear plasmonic response of equilateral graphene nanotriangles. (a) Geometry of the nanoisland considered where the light polarization is indicated by a yellow arrow. (b) Scheme of the edge terminations considered in the quantum-mechanical model –AC (left) and ZZ (right)–, and the uniform slab used in the classical results (center). (c-f) Spectra of the linear polarizability (c), and nonlinear polarizabilities for SHG (d), THG (e), and Kerr effect (f), as obtained from the quantum model for AC (solid curves) and ZZ (dashed curves) edge terminations, compared with classical results (filled curves). The different Fermi energies considered here are numerically colored following the code given in panel (c). In all cases, the size and intrinsic decay rate are $D \sim 10\,\text{nm}$ and $\hbar\gamma = 50\,\text{meV}$, respectively. The figure is adapted from Ref. [153].

4.5 Conclusions

In this chapter, we have observed that doped graphene is a very nonlinear material with plasmons producing extraordinary nonlinear optical effects. We have started a detailed study of these nonlinear effects by describing the physical relevance of three important processes: SHG, THG, and Kerr effect. The strength of these nonlinear processes in doped graphene is remarkably higher than in standard nonlinear materials which assesses the potential versatility of doped graphene for nonlinear optical devices.

In section (4.2) we have obtained the expressions of the classical second-, third-harmonic, and Kerr effect conductivities using the BTE. Under this formalism, we have only considered intraband e-h transitions over extended graphene layers at $T = 0$. For the second-harmonic (resulting from a nonlocal contribution), our expression matches previous results found in the literature, while for the (local) third-harmonic and Kerr effect we properly introduce scattering mechanisms in the BTE and then, different expressions are attained. Moreover, using these nonlinear conductivities, in section (4.3) we have extended the electrostatic scaling law formalism given in Chapter 1 to get simple expressions for the nonlinear polarizabilities.

Finally, in section (4.4), we have compared the classical nonlinear model approach with a quantum-mechanical one that includes interband e-h transitions, as well as nonlocal and finite-size effects, where doped AC- and ZZ-edged triangular nanoislands are considered. Although we have focused on sizes $D \sim 10\,\text{nm}$, these effects cannot be easily ignored up to larger dimensions ($D \sim 20\,\text{nm}$) or in other geometries like nanoribbons [153]. Interestingly, we have found that the classical approach clearly underestimates the SHG and Kerr effect except for low levels of doping, while for the THG a reasonable agreement is observed. We thus conclude that a quantum-mechanical description predicts a significantly higher nonlinear response of doped graphene, which could be useful for future nonlinear optical devices.

Chapter 5

Molecular sensing with graphene

Structural vibrations in molecules produce infrared spectral features that can be regarded as specific barcodes, therefore allowing the resolution of their chemical identity. However, since the size of the molecules is much smaller than the optical wavelength of the incident light, their interaction is extremely weak. Fortunately, as mentioned in Chapter 1, the tight confinement and large field enhancement produced by graphene LSPs (renamed as "plasmons" for simplicity) offer a solution to increase this interaction. By exposing certain target molecules to these graphene plasmons, the former greatly improve their ability to absorb or inelastically scatter light in the NIR regime in order to change their roto-vibrational energy [see Appendix C for more details]. This is the underlying principle of the spectroscopy techniques known as surface-enhanced infrared absorption (SEIRA) [155] and surface-enhanced Raman scattering (SERS) [156, 157]. These techniques permit a full characterization of the roto-vibrational molecular structure with a sensitivity that goes down to the single molecule detection limit [158, 159, 160]. Besides, the very broad absorption band ranging from THz to NIR frequencies [34, 64, 83, 161] and strong field confinement convert doped graphene as an ideal platform for spectrometer-free sensing and chemical identification of molecules as a function of the graphene doping level. This is because the molecular roto-vibrational transitions lie in the NIR where doped graphene nanostructures with characteristic size in the range of tens to hundreds of

nanometers support intense plasmons [162].

In this chapter, we study in detail the great potential of graphene plasmons for SEIRA and SERS. We focus on the detection of molecules nearby self-standing graphene nanodisks. Based on realistic numerical simulations of the graphene nanodisks, we show that the recorded signal integrated over a broadband spectral range is sufficient to provide chemical identification when it is examined as a function of the graphene doping level $E_{\rm F}$. Interestingly, our results pave the way for the development of cost-effective revolutionary sensors capable of identifying spectral signatures of molecules without using spectrometers and laser sources.

5.1 SEIRA

This spectroscopy technique discovered in 1980 [163] exploits the induced electric field enhancement exerted by a plasmonic nanostructure in order to increase by $\sim 10-1000$ times the intensity of infrared absorption by a molecule [163, 164, 165]. Here, we consider a single generic molecule of pyridine (C_5H_5N) placed at a short distance h over a uniformly doped graphene nanodisk with diameter $D = 300\,\text{nm}$ and externally illuminated by a normal plane wave with associated electric field $\mathbf{E}_0$ as depicted in Fig. 5.1(a). The classical response of the graphene nanodisk is obtained from the full-numerical solutions of Maxwell's equations using BEM [see section (1.4.1)]. We assume that the dielectric function of graphene is given by Eq. (1.15) for a thickness $t = 0.1\,\text{nm}$, whereas the graphene conductivity is taken from the local-RPA model at $T = 300\,\text{K}$ [see Eq. (1.18)]. The relaxation time τ is estimated from the dc Drude model [see last paragraph of section (1.4.1)]. Remarkably, this parameter ultimately determines the energy resolution $\hbar\tau^{-1}$ that characterizes spectrometer-free sensing of molecular resonances [*i.e.*, the sensing resolution is determined by the plasmon quality factor $Q = \omega_{\rm p}\tau$, and this is in turn proportional to the graphene mobility, as shown in Fig. 5.3(b)]. Moreover, we observe from Fig. 5.1(b), where we plot the absorption cross-section of the disk normalized to its area [see Eq. (1.30)] for $E_{\rm F} = 0.4\,\text{eV}$ and $\mu = 2000\,\text{cm}^2/(\text{V s})$, that the disk plasmons are clearly resolvable exhibiting a dominant, low-energy feature of dipolar character (see inset). In Fig. 5.1(c) we represent the absorption spectrum of pyridine. For simplicity, the available experimental data of the electric polarizability of the molecule

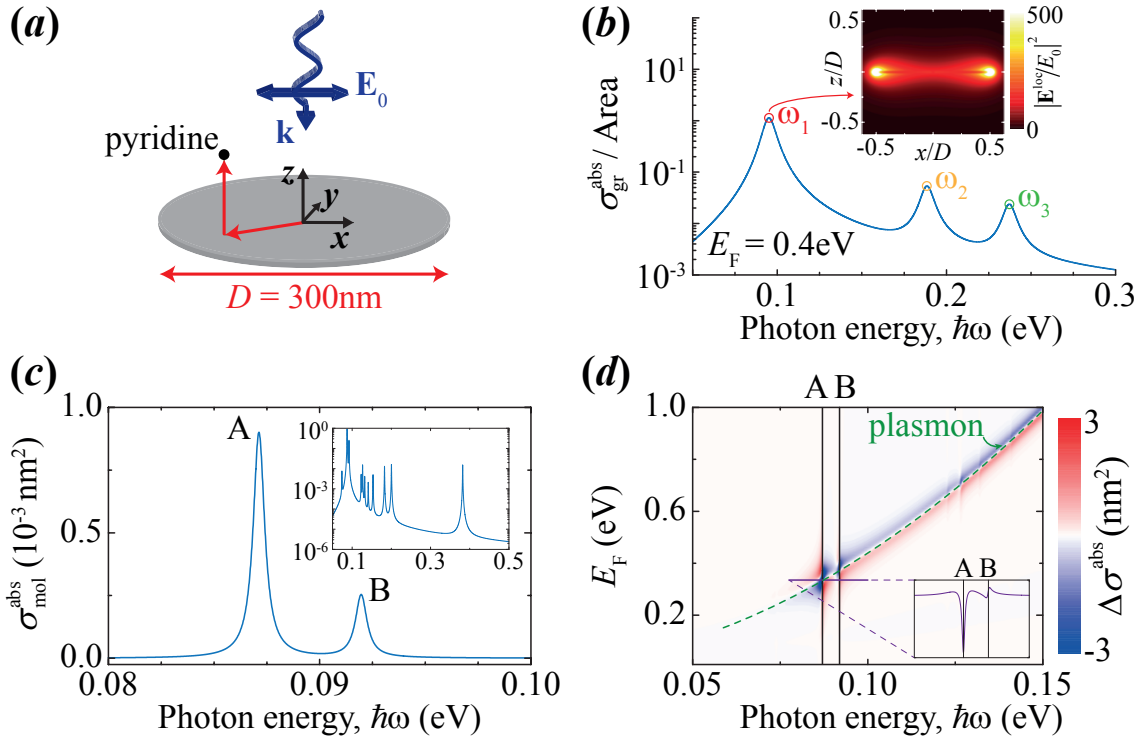

Figure 5.1: Surface-enhanced infrared absorption (SEIRA) spectroscopy with graphene plasmons. (a) Sketch of the structure here considered, consisting of a self-standing uniformly doped graphene nanodisk with diameter $D = 300\,\mathrm{nm}$ and a single pyridine molecule on top. (b) Absorption cross-section spectrum of the nanodisk normalized to the graphene area for a Fermi energy $E_\mathrm{F} = 0.4\,\mathrm{eV}$ and mobility $\mu = 2000\,\mathrm{cm}^2/(\mathrm{V\,s})$. The inset shows the near-field intensity of the lowest-energy dipolar plasmon in the $x-z$ plane. (c) Absorption cross-section of a pyridine molecule. (d) Change in the absorption cross-section induced the pyridine molecule placed near the nanodisk edge at $\mathbf{r}_0 = (150, 0, 1)\,\mathrm{nm}$ [see axes in panel (a)], as a function of the photon and graphene Fermi energies. The inset shows a line scan along a segment in the region where the main molecular absorption features A and B cross the lowest-order dipolar disk plasmon (green dashed curve). The figure is adapted from Ref. [93].

[166] is fitted to a sum of Lorentzians as

$$\alpha_{\rm mol}(\omega) = \frac{1}{\hbar^2}\sum\nolimits_j \frac{\kappa_j}{\omega_j^2 - \omega(\omega + {\rm i}\gamma)}, \tag{5.1}$$

where κ_j and ω_j are fitting parameters (see complete data in Table 1 of Ref. [93]), and we assume a fixed bandwidth (intrinsic damping) $\hbar\gamma = 0.7\,{\rm meV}$. We observe from Fig. 5.1(c) that two of these Lorentzians (modes $j = 2, 3$) dominate the spectral range at photon energies $\hbar\omega_{\rm A} \approx 0.087\,{\rm eV}$ and $\hbar\omega_{\rm B} \approx 0.092\,{\rm eV}$, respectively. In any case, the polarizability is very small $\alpha_{\rm mol} \approx 10^{-22}\,{\rm cm}^3$.

Upon normal-incidence illumination, the pyridine molecule placed at the position $\mathbf{r}_0$ experiences a total enhanced local field $\mathbf{E}^{\rm loc}(\mathbf{r}_0,\omega) = \mathbf{E}_0 + \mathbf{E}^{\rm ind}(\mathbf{r}_0,\omega) + \mathbf{E}^{\rm self}(\mathbf{r}_0,\omega)$, given by the superposition of $\mathbf{E}_0$, the field induced by the graphene nanodisk $\mathbf{E}^{\rm ind}(\mathbf{r}_0,\omega)$, and the self-induced field of the molecule $\mathbf{E}^{\rm self}(\mathbf{r}_0,\omega)$. The latter is negligibly small for most molecules, so that it is disregarded in what follows. Assuming dominant the absorption process over scattering made by the graphene nanodisk [see Fig. 1.9(a)], the absorption cross-section obtained from the optical theorem [26] of the whole system formed by the molecule and graphene is given by the superposition

$$\sigma^{\rm abs}_{\rm gr+mol}(\omega) \approx \frac{4\pi}{k}{\rm Im}\left\{[f_0(\omega) + f_1(\omega)]\,\hat{n}\cdot\frac{\mathbf{E}_0^*}{E_0^2}\right\}. \tag{5.2}$$

Here, $f_0(\omega)$ is the far-field amplitude only with graphene, $f_1(\omega)$ is the far-field amplitude only with the molecule, and $\hat{n}$ is the direction of the incident polarization. Taking into account that the dipole moment of the molecule is $p_{\rm mol}(\omega) = \alpha_{\rm mol}(\omega)E^{\rm loc}(\omega)$ and $f_1(\omega) = k^2 p_{\rm mol}(\omega)$, we find straightforwardly that the shift on the absorption cross-section of the molecule or SEIRA cross-section is

$$\Delta\sigma^{\rm abs}(\omega) = \sigma^{\rm abs}_{\rm gr+mol}(\omega) - \sigma^{\rm abs}_{\rm gr}(\omega) = 4\pi k{\rm Im}\{\alpha_{\rm mol}(\omega)\}\left|\frac{\mathbf{E}^{\rm ind}(\mathbf{r}_0,\omega)}{E_0}\right|^2, \tag{5.3}$$

where we approximate the increase in the local field intensity as $|\mathbf{E}^{\rm ind}(\mathbf{r}_0,\omega)/E_0|^2$. We observe from Eq. (5.3) that the inclusion of graphene permits a linear enhancement of $\Delta\sigma^{\rm abs}(\omega)$ with the induced intensity, and this behavior is in turn more remarkable when the impinging radiation is on resonance with the plasmon frequency.

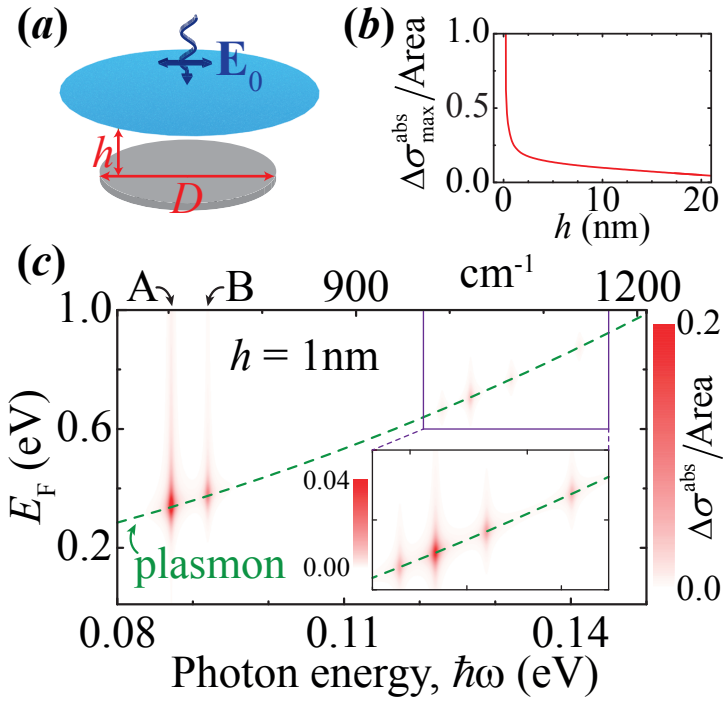

Figure 5.2: Doping dependence in the absorption cross-section of molecules in SEIRA spectroscopy. We represent in panel (c) the SEIRA cross-section normalized to the graphene disk area ($\Delta\sigma^{\rm abs}$/Area) produced by the interaction of a layer of pyridine molecules with the graphene disk considered in Fig. 5.1. The molecules are placed at a distance $h = 1\,$nm above the graphene plane [see panel (a)] with a density of one molecule per nm^2 and covering an area that extends well beyond the nanodisk edge. The lower-right inset in the panel (c) shows a zoom of a high-photon-energy region in which weaker pyridine resonances are observable. Panel (b) shows the h dependence of the absorption cross-section for photon and Fermi energies corresponding to the absolute maximum of $\Delta\sigma^{\rm abs}$/Area. The figure is adapted from Ref. [93].

In Fig. 5.1(d) we plot $\Delta\sigma^{\rm abs}(\omega)$ for a pyridine molecule placed at $\mathbf{r}_0 = (150, 0, 1)\,$nm over the edge of the graphene nanodisk ($z = 0$ plane), with a conservative value of the mobility $\mu = 2000\,{\rm cm}^2/({\rm V\,s})$. We observe that $\Delta\sigma^{\rm abs}(\omega)$ is clearly enhanced along the dipolar plasmon (green dashed) curve of the graphene nanodisk, which shifts in energy with varying doping level since $\hbar\omega_{\rm p} \propto E_{\rm F}^{1/2}$. Interestingly, $\Delta\sigma_{\rm abs}(\omega)$ experiencies an enhancement of $\sim 10^3$ with respect to the absorption cross-section of the isolated molecule.

In practical applications, one is interested in sensing a small concentration of molecules placed over a range of distances from the graphene nanodisk. Here, we consider a circular monolayer of pyridine molecules with diameter $D_{\rm mol} = 450\,$nm and a density of $n_{\rm mol} = 1\,{\rm molecule/nm}^2$ separated a distance $h = 1\,$nm from graphene [see Fig. 5.2(a)]. The change in the SEIRA cross-section is simply given now by

$$\Delta\sigma^{\rm abs}(\omega) = 4\pi n_{\rm mol}\, k{\rm Im}\{\alpha_{\rm mol}(\omega)\}\int_{\mathcal{S}} {\rm d}^2\mathbf{r}_0 \left|\frac{\mathbf{E}^{\rm ind}(\mathbf{r}_0,\omega)}{E_0}\right|^2, \tag{5.4}$$

where the integral is extended over the surface layer $\mathcal{S}$ of pyridine molecules. The resulting values normalized to the graphene area are shown in Fig. 5.2(c) as a function of the photon energies and $E_{\rm F}$. The important message from this plot is that there is a one-to-one correlation between the molecular resonant photon energies and $E_{\rm F}$ at which the dipolar plasmon overlaps with those resonances. More precisely, this leads to peaks in $\Delta\sigma^{\rm abs}(\omega)$ at $E_{\rm F} \approx 0.34$ and $0.39\,$eV, corresponding to the molecular resonances of energies $\hbar\omega_{\rm A} \approx 0.087\,$eV and $\hbar\omega_{\rm B} \approx 0.092\,$eV, respectively.

In Fig. 5.2(b) we plot the maximum values of $\Delta\sigma^{\rm abs}(\omega)$ as a function of the separation distance h. We observe that the results are qualitatively similar over distances up to a few nanometers from the graphene, and therefore, the technique should be robust against the uncertainty in the exact location of the molecules, provided their separation is in the $\lesssim 10\,$nm range.

The above mentioned one-to-one correlation between molecular resonances and $E_{\rm F}$ suggests that it is possible to obtain spectral information by recording the absorption as a function of $E_{\rm F}$, rather than $\hbar\omega$. Indeed, upon illumination by spectrally broad sources (*e.g.*, an infrared lamp), this graphene-based sensor device can discriminate resonant photon energies by examining the Fermi levels at which the measured (spectrally unresolved) absorbed power is peaked. The plasmons of the

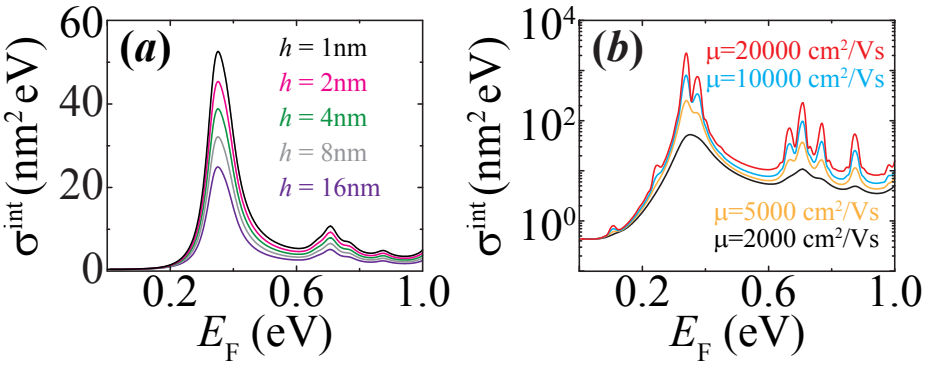

Figure 5.3: Molecular sensitivity of the doping-dependent frequency-integrated absorption in SEIRA spectroscopy. We analyze the integral over NIR photon energies $(0-1\,\mathrm{eV})$ of the SEIRA cross-section (*i.e.*, $\sigma^{\mathrm{int}} = \hbar\int_0^1 \mathrm{d}\omega\,\Delta\sigma^{\mathrm{abs}}$) produced by a layer of pyridine molecules as a function of E_{F} for (a) several molecule-graphene distances with fixed graphene mobility $\mu = 2000\,\mathrm{cm}^2/(\mathrm{V\,s})$, and (b) fixed distance $h = 1\,\mathrm{nm}$ and different values of μ. The figure is adapted from Ref. [93].

graphene nanodisk act as amplifiers of the incident light at gate-controlled photon energies. We illustrate this concept by calculating the integral over IR photon energies $(0-1\,\mathrm{eV})$ of the SEIRA cross-section, $\sigma^{\mathrm{int}} = \hbar\int_0^1 \mathrm{d}\omega\,\Delta\sigma^{\mathrm{abs}}$. In Fig. 5.3(a) we plot the results for several molecule-layer/graphene distances which suggest that the sensor can perform similarly well up to a distance $\lesssim 10\,\mathrm{nm}$. Additionally, we explore in Fig. 5.3(b) a range of feasible graphene mobilities ranging from the conservative value that we use in Fig. 5.1, to higher-quality graphene. Although the former is already capable of giving sufficient molecule-specific information to resolve the presence of pyridine molecules, we note that currently attainable high-quality graphene enables further discrimination of weak vibrational features (*e.g.*, it allows us to resolve the A and B resonances, which are separated by $\sim 5\,\mathrm{meV}$). We thus conclude that the spectral resolution of this spectrometer-free technique is limited by the intrinsic graphene plasmon damping $\sim \hbar\tau^{-1}$.

In all the previous results, we have assumed for simplicity that the target molecules are not adsorbed near the graphene nanodisk so that the optical properties of the latter do not change. A variation in E_{F} due to the molecules can be a serious problem that might limit the applicability of our proposed sensing technique as it adds an element of uncertainty in the determination of the graphene Dirac point [see sec-

tion (1.3.2)]. We anticipate several possible strategies to deal with this uncertainty: (i) the entire spectrum changes when moving E_{F}, and therefore, it should be sufficient to resolve spectral distances associated with the molecular features; (ii) in many practical situations, one is interested in discriminating between a certain finite number of different detected molecules, then the proposed sensor can be calibrated for each of them; and (iii) the possible charge transfer between the molecule and graphene can be drastically reduced by the addition of a thin transparent insulating layer, which according to Fig. 5.3(a) can have a thickness of several nanometers without causing a serious reduction in sensing capabilities. These strategies can be also extended to the SERS spectroscopy that we present below.

5.2 SERS

This spectroscopy technique based on the Raman scattering [see Appendix C] was first used in 1974 [167] precisely with pyridine molecules. The authors observed reversible Raman-shifts originated from the direct adsorption of the molecules onto a layer of a plasmonic material (silver in this case) by applying an external potential. Raman scattering is a nonlinear second-order process proportional both to the incident light intensity and to the emission from the inelastically frequency-shifted transition dipole [168]. Unfortunately, owing to the non-resonant nature of this effect, the cross-sections of single Raman-active molecules are very small ($\sim 10^{-26}\,\mathrm{cm}^2$). Therefore, similarly to SEIRA, an enhancement in the local field intensity provided by a plasmonic layer is needed in order to increase the intensity of the Raman signal.

In our case, we follow a similar procedure as in section (5.1), and we use the dipolar plasmon of the graphene nanodisk in order to amplify the Raman signal of a certain generic molecule at position $\mathbf{r}_0$. Remarkably, we supplement the system with a resonant silicon cavity [169] that amplifies the intensity of the incident pump light with energy $\hbar\omega_{\mathrm{pump}} = 0.422\,\mathrm{eV}$ (*i.e.*, the emission line of an Er:YAG laser) [see Fig. 5.4(a)]. The SERS enhancement with respect to the isolated molecule is given by

$$\mathrm{EF}_{\mathrm{SERS}} = \left| \frac{\mathbf{E}^{\mathrm{ind}}(\mathbf{r}_0, \omega_{\mathrm{pump}})}{E_0} \right|^2 \left| \frac{\mathbf{p}^{\mathrm{tot}}(\mathbf{R}, \omega_1)}{p_0(\omega_1)} \right|^2 , \tag{5.5}$$

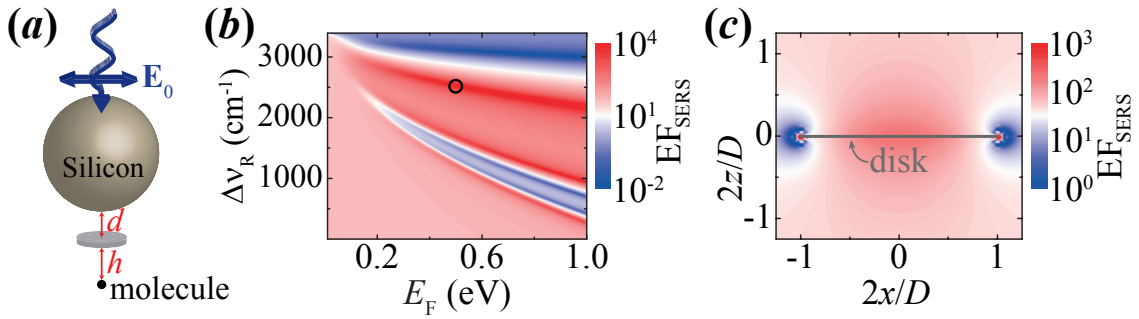

Figure 5.4: Surface-enhanced Raman scattering (SERS) with graphene plasmons. (a) Sketch of the system under consideration, consisting of a silicon sphere (diameter 1530 nm, $\varepsilon_{\mathrm{Si}} = 12$) placed at a distance $d = 9\,\mathrm{nm}$ above a graphene disk (diameter $D = 300\,\mathrm{nm}$), which is in turn placed at a distance $h = 1\,\mathrm{nm}$ above a Raman active molecule. The system is illuminated with a 0.422 eV light plane wave (*i.e.*, $\lambda \approx 2.94\,\mu\mathrm{m}$) that is resonant with a mode of the sphere (*i.e.*, the sphere works as a nanofocuser, similarly to previous designs [169]). (b) SERS enhancement factor $\mathrm{EF_{SERS}}$ (relative to an isolated molecule), as a function of Raman-shift $\Delta\nu_{\mathrm{R}}$ and graphene Fermi energy E_{F} for a molecule placed along the symmetry axis. (c) SERS enhancement as a function of the position of the molecule relative to the graphene disk for doping and Raman shift conditions corresponding to the open circle in panel (b). The figure is adapted from Ref. [93].

where ω_1 is the final frequency of the molecule after the Raman transition [see Eq. (C.2)]. Moreover, $\mathbf{E}^{\mathrm{ind}}(\mathbf{r}_0, \omega_{\mathrm{pump}})$ is the induced field at the incident light frequency, mainly controlled by the silicon cavity, whereas $\mathbf{p}^{\mathrm{tot}}(\mathbf{R}, \omega_1) = \mathbf{p}_0(\omega_1) + \mathbf{p}^{\mathrm{ind}}(\mathbf{R}, \omega_1)$ is the total superposition of the free-molecule Raman transition dipole moment $\mathbf{p}_0(\omega_1)$, and the dipole induced by the molecule on the surrounding structure $\mathbf{p}^{\mathrm{ind}}(\mathbf{R}, \omega_1)$. For simplicity, in our calculation of $\mathbf{E}^{\mathrm{ind}}(\mathbf{r}_0, \omega_{\mathrm{pump}})$ we only consider the silicon cavity and neglect the graphene nanodisk. This happens because the Mie resonant quality factor of the silicon sphere is so high that the non-resonant effect of the graphene nanodisk can be neglected. Similarly, we obtain $\mathbf{p}^{\mathrm{ind}}(\mathbf{R}, \omega_1)$ as the dipole induced on the graphene nanodisk placed at $\mathbf{R}$ without taking into account the silicon cavity. This is possible since the graphene nanodisk supports resonant plasmons at the Raman-shifted frequency $\hbar\omega_1$. Thus, as graphene appears on resonance with the final roto-vibrational energy of the molecule, we can neglect the effect of the silicon sphere. Furthermore, like in SEIRA, we neglect the self-induced

polarization of the molecule.

In Fig. 5.4(b) we plot the enhancement factor $\mathrm{EF}_{\mathrm{SERS}}$ as a function of the molecule Raman-shift $\Delta\nu_{\mathrm{R}}$ and E_{F} for the system depicted in Fig. 5.4(a), with an edge-to-edge distance between the silicon sphere and the nanodisk $d = 9\,\mathrm{nm}$, and a separation between the molecule and the nanodisk $h = 1\,\mathrm{nm}$. Under these conditions, the silicon cavity produces an enhancement of $|\mathbf{E}^{\mathrm{ind}}(\mathbf{r}_0, \omega_{\mathrm{pump}})/E_0|^2 \approx 2200$. The important message of this plot is that if we fix $\Delta\nu_{\mathrm{R}}$, for each value of E_{F} we have a different value of $\mathrm{EF}_{\mathrm{SERS}}$, and there is a specific one for which $\mathrm{EF}_{\mathrm{SERS}}$ is maximum (particularly here $\sim 10^4$). Furthermore, the actual value strongly depends on the molecule position relative to the nanodisk [see Fig. 5.4(c)], yielding again qualitatively similar performance for molecule-graphene distances in the $\lesssim 10\,\mathrm{nm}$ region.

5.3 Conclusions

In this chapter, we have presented a new infrared sensing strategy that avoids the use of costly and inefficient optical elements (*e.g.*, spectrometers and laser sources) and simply involves infrared lamps and electrical doping of graphene through an externally-applied gate voltage. We have shown the ability of graphene nanodisks to resolve the chemical identity of adsorbed molecules from the measurement of broadband-integrated absorption and Raman scattering signals enhanced by the electrically tunable plasmons of this material. Their narrowness is sufficient to resolve the frequency of the molecular resonances in the integrated intensity as a function of the controlled doping level. This control is an important practical aspect of our proposed sensor. We contemplate a gating device in which a bottom gate is combined with a contact for the graphene. Electrical connectivity could be provided by a thin transparent insulating layer, as recently used to demonstrate active control of the plasmons sustained on the graphene nanodisk [71]. Alternatively, we expect similar results for graphene nanoribbons, whose plasmon frequencies and characteristics for transversal polarization are similar to those of the nanodisks, with the additional advantage that the former structures can be contacted in a region far from the active sensing area.

Remarkably, the large confinement and induced intensity amplification associated with graphene plasmons leads to SEIRA and SERS intensity enhancements

reaching $\sim 10^3$ and $\sim 10^4$, respectively, which foster the use of graphene to improve traditional sensing techniques based on spectrally resolved infrared absorption and Raman scattering. The roto-vibrational energy resolution of the proposed sensing scheme is determined by the spectral width of graphene plasmons (*i.e.*, it is essentially limited by the plasmonic quality factor of the material) and can reach a few meV under currently realistic conditions.

In summary, graphene plasmons provide a versatile platform for sensing, thus opening new possibilities for exploiting their large electro-optical tunability, and in particular, the realization of label-free chemical identification without the involvement of spectrometers and laser sources.

Chapter 6

Conclusions

In this thesis, we have realized an in-depth study of the plasmonic response of graphene under different novel conditions. We have focused on theoretical concepts that could be useful for the design of future graphene plasmonic devices. We thus proceed to summarize in this final chapter the overall conclusions of our work.

In Chapter 1, we have concisely introduced the general properties of graphene. We have started with a brief review of its history and the most common techniques of synthesis. Afterwards, we have studied its peculiar optoelectronic properties resulting from the singular linear band structure. Additionally, we have classically described the different types of surface Dirac plasmons that graphene, either within a finite geometry (LSPs) or as an extended layer (SPPs), can sustain under uniform doping conditions. Finally, we have presented a general electrostatic scaling law to find directly the classical LSP frequencies of a given graphene nanostructure as a function of its doping level, characteristic size, and dielectric environment.

In Chapter 2, we have studied the classical behavior of graphene Dirac plasmons under diverse geometric schemes, as well as under realistic inhomogeneous doping configurations. First, we have derived a novel method based on the plasmon wave function of an individual uniformly doped nanoribbon to study the interaction of multiple nanoislands. Remarkably, our model possesses a better degree of accuracy than the typical dipole-dipole interacting model. Later, we have shown how the inhomogeneities in the doping distribution affect the LSPs sustained on graphene nanoribbons, nanodisks, and the SPPs of extended layers. Specifically, we find

that for a nanoribbon doped with a uniform electric field, the plasmonic dispersion differs with respect to the uniform doping case, with the induced charge density piling up near the center of the nanoribbon. Furthermore, we have observed that doping with a single electron is sufficient to excite a LSP in nanodisks, whose energy considerably differ from those under a uniform doping. Finally, we have noticed that a periodic doping of extended graphene induces the creation of plasmon bands. Besides, we observed that a periodic doping through a distribution of equally-signed or alternately-signed point charges boosts the radiative emission of an optical emitter in the vicinity of graphene by taking advantage of the Van Hove singularities.

In Chapter 3, we have shown the importance of quantum nonlocal effects in narrow nanostructures. In particular, we have focused on graphene nanoribbons, whose lowest-order dipolar LSPs are remarkably quenched when their energies are above the Fermi level. We have used a quantum mechanical model based on a TB-RPA approach where we can distinguish between AC and ZZ edges, so that we could observe that nonlocal effects are important in interacting nanoribbons at short separations, leading to substantial blueshifts in the LSPs. Finally, we have found that the removal of a single row of carbon atoms induces a dramatic increase in the LSP energy, observed both in co-planar dimers and arrays of nanoribbons.

In Chapter 4, we have shown the remarkable nonlinear response of LSPs in doped graphene. Combining the electrostatic scaling formalism presented in Chapter 1 and the BTE, we have obtained simple expressions for the conductivities and polarizabilities related with three important nonlinear processes: SHG, THG, and Kerr effect. Finally, we have compared the plasmonic response of graphene nanotriangles using a classical and a quantum-mechanical model. Interestingly, the classical approach clearly underestimates the SHG and Kerr effect in narrow ribbons and small islands except for low levels of doping, whereas for the THG we find a reasonable agreement.

Finally, in Chapter 5, we have introduced a new NIR sensing technique that only requires infrared lamps and doped graphene nanodisks, thus allowing us to resolve the chemical identity of the molecules adsorbed near the disk. We have observed that the energy resolution of the roto-vibrational modes expected from our technique is determined by the spectral width of graphene LSPs. Interestingly, due to the large confinement and induced intensity amplification associated with LSPs, we have reached enhancements of $\sim 10^3$ and $\sim 10^4$ in SEIRA and SERS, respectively.

Appendix A

Effect of the dielectric environment on graphene

In this appendix, we discuss the electrostatic response of an extended 2D graphene layer placed in the interface between two different dielectric media (permittivity ε_1 on top and ε_2 below). For our purpose, we calculate the electrostatic potential created by an external point charge Q_0 over graphene. We assume that graphene lies on the $z = 0$ plane with the charge placed on top at a distance d. We aim at solving the equations given by the third expression of Eq. (1.11) and $\mathbf{E}(\mathbf{r}) = -\nabla\Phi(\mathbf{r})$ (the frequency dependence is avoided for simplicity).

If we assume negligible the conductivity of graphene, the electric field at its boundaries satisfies the conditions

$$\lim_{z\to 0^+} \begin{pmatrix} \varepsilon_1 E_z \\ E_x \\ E_y \end{pmatrix} = \lim_{z\to 0^-} \begin{pmatrix} \varepsilon_2 E_z \\ E_x \\ E_y \end{pmatrix}. \tag{A.1}$$

We apply the method of charge images [111], so that in the region $z > 0$ the electrostatic potential can be written as the sum of two terms: the potential generated by the real charge Q_0 placed at d, and the one generated by the image charge Q_0' at $d' = -d$ [see Fig. A.1]. On the other hand, in the region $z < 0$, the potential depends on the one induced by an image charge Q_0'' localized at $d'' = d$. Therefore,

we can claim that

$$\begin{aligned}\Phi(z>0) &= \frac{1}{\varepsilon_1}\left(\frac{Q_0}{R_1}+\frac{Q_0'}{R_2}\right),\\ \Phi(z<0) &= \frac{1}{\varepsilon_2}\frac{Q_0''}{R_1},\end{aligned} \tag{A.2}$$

with $R_1 = \sqrt{x^2+(z-d)^2}$ and $R_2 = \sqrt{x^2+(z+d)^2}$. We change to cylindrical coordinates $\left(i.e., \nabla = \partial_\rho\,\hat{\rho} + \rho^{-1}\partial_\theta\,\hat{\theta} + \partial_z\,\hat{z}\right)$, then the electrostatic electric field can be expressed as

$$\begin{aligned}E_z(z>0) &= \frac{1}{\varepsilon_1}\left\{\frac{Q_0(z-d)}{\left[\rho^2+(z-d)^2\right]^{3/2}}+\frac{Q_0'(z+d)}{\left[\rho^2+(z+d)^2\right]^{3/2}}\right\},\\ E_z(z<0) &= \frac{1}{\varepsilon_2}\left\{\frac{Q_0''(z-d)}{\left[\rho^2+(z-d)^2\right]^{3/2}}\right\},\\ E_\rho(z>0) &= \frac{1}{\varepsilon_1}\left\{\frac{Q_0\rho}{\left[\rho^2+(z-d)^2\right]^{3/2}}+\frac{Q_0'\rho}{\left[\rho^2+(z+d)^2\right]^{3/2}}\right\},\\ E_\rho(z<0) &= \frac{1}{\varepsilon_2}\left\{\frac{Q_0''\rho}{\left[\rho^2+(z-d)^2\right]^{3/2}}\right\}.\end{aligned} \tag{A.3}$$

If we impose now the continuity conditions given in Eq. (A.1), we straightforwardly find that $Q_0 - Q_0' = Q_0''$, and $\left(Q_0+Q_0'\right)/\varepsilon_1 = Q_0''/\varepsilon_2$. Combining these two expressions we obtain

$$\begin{aligned}Q_0' &= Q_0\left(\frac{\varepsilon_1-\varepsilon_2}{\varepsilon_1+\varepsilon_2}\right),\\ Q_0'' &= Q_0\left(\frac{2\varepsilon_2}{\varepsilon_1+\varepsilon_2}\right).\end{aligned} \tag{A.4}$$

Restricted to the graphene plane ($z=0$), we have that $R_1 = R_2 = \sqrt{\rho^2+d^2} \equiv R$. Therefore, the electrostatic potential remains

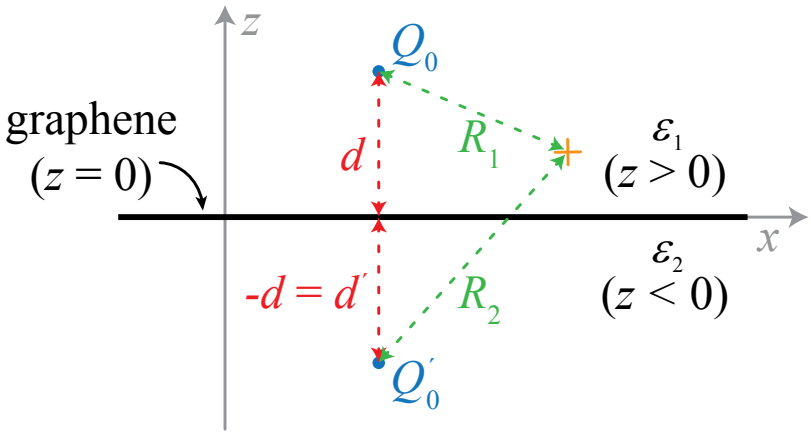

Figure A.1: Scheme of the system used for calculating the electrostatic potential at a certain point (orange cross) in the $z > 0$ region caused by an external point charge Q_0 (upper blue dot) placed at a certain distance d over the graphene plane ($z = 0$). The graphene layer acts as an interface between two different dielectric media with permittivities ε_1 and ε_2. We apply the method of charge images [111], so that we need to consider the potential generated by the real charge Q_0 and the image charge Q'_0 placed at $d' = -d$.

$$\begin{aligned} \Phi(z \to 0^+) &= \frac{1}{\varepsilon_1} \frac{Q_0 + Q'_0}{R}, \\ \Phi(z \to 0^-) &= \frac{1}{\varepsilon_2} \frac{Q''_0}{R}. \end{aligned} \tag{A.5}$$

If we implement Eq. (A.4) into Eq. (A.5), and we consider continuous the electrostatic potential at the boundary, we finally find that

$$\Phi(z = 0) = \frac{2}{\varepsilon_1 + \varepsilon_2} \frac{Q_0}{R}. \tag{A.6}$$

This expression contains the dependence of graphene on the dielectric environment which is extensively used in all the electrostatic calculations made throughout this thesis.

Appendix B

Derivation of the LSP resonance frequency from the electrostatic scaling law

In this appendix, we derive the LSP frequency given in Eq. (1.47) from the electrostatic scaling law formalism. Implementing the Drude model conductivity [see Eq. (1.16)] into Eq. (1.36), we have

$$\eta(\omega) = \frac{-e^2}{\pi}\frac{2}{(\varepsilon_1+\varepsilon_2)}\frac{E_{\mathrm{F}}}{D}\frac{1}{\hbar^2\omega^2}\frac{1}{(1+\mathrm{i}\gamma/\omega)}. \tag{B.1}$$

For $\eta \equiv \eta_j$ (the subindex j corresponds to different eigenstates or electromagnetic modes) we can express the LSP frequency as

$$\omega_{\mathrm{p}}^{\mathrm{Drude}} = \frac{e}{\hbar}\sqrt{\left[\frac{2}{\varepsilon_1+\varepsilon_2}\right]\left[\frac{1}{-\pi\eta_j}\right]\left[\frac{E_{\mathrm{F}}}{D}\right]}\,\frac{1}{\sqrt{1+\mathrm{i}\gamma/\omega_{\mathrm{p}}^{\mathrm{Drude}}}}. \tag{B.2}$$

If we safely assume that $\gamma \ll \omega_{\mathrm{p}}^{\mathrm{Drude}}$, we can use the approximation $1/\sqrt{1+\delta} \simeq 1-\delta/2$, where we name $\delta = \gamma/\omega_{\mathrm{p}}^{\mathrm{Drude}}$. Thus, considering the definition given in Eq. (1.48), we can rewrite Eq. (B.2) as

$$\omega_{\mathrm{p}}^{\mathrm{Drude}} \approx \omega_j^{\mathrm{Drude}}\left(1-\frac{\mathrm{i}\gamma/2}{\omega_{\mathrm{p}}^{\mathrm{Drude}}}\right). \tag{B.3}$$

This expression can be reformulated as a second-order polynomial equation $x = y(1 - a/x)$, with $x \equiv \omega_{\mathrm{p}}^{\mathrm{Drude}}$, $y \equiv \omega_j^{\mathrm{Drude}}$, and $a \equiv \mathrm{i}\gamma/2$. We can directly find the solution

$$x = \frac{y}{2}\left[1 + \sqrt{1 - \frac{4a}{y}}\right] \approx \frac{y}{2}\left[2 - \frac{2a}{y}\right] = y - a, \tag{B.4}$$

where we have used the approximation $\sqrt{1-\kappa} \simeq 1 - \kappa/2$, being $\kappa = (4a/y) \ll 1$. Therefore, after recovering the proper variables, we finally obtain the expression of the LSP frequency in the electrostatic regime shown in Eq. (1.47)

$$\omega_{\mathrm{p}}^{\mathrm{Drude}} \approx \omega_j^{\mathrm{Drude}} - \mathrm{i}\gamma/2. \tag{B.5}$$

Remarkably, for nanostructures with characteristic size comparable to the incident light wavelength, retardation effects become important and the final LSP frequency is redshifted [see Fig. 1.9(a)].

Appendix C

Infrared absorption and Raman scattering

It is known from Quantum Mechanics that an electron bound to an atom possesses only certain energy levels corresponding to its electronic states. For example, for a hydrogen atom, the electronic energy levels are determined by [170] $\epsilon_n^{\mathrm{el}} = -13.6/n^2\,\mathrm{eV}$ where $n = 1, 2, 3\ldots$ is the principal quantum number. The bound energy is expressed as a negative number because we need that much energy to unbind the electron from the hydrogen nucleus. Due to this quantization of the energy levels, for radiative electronic transitions the electron can only absorb photons with energies exactly matching the gap between two different electronic states. The energy of these photons typically falls in the visible and UV regimes.

In the case of molecules, the scheme of energy levels is more complicated. In addition to electronic transitions, we need to consider that the constituting atoms can vibrate with respect to the "equilibrium distance", and the whole molecule can rotate with respect to its mass center. Hence, the internal energy of the molecule ϵ^{int} under the Born-Oppenheimer approximation [171] is given by the superposition of the electronic, vibrational, and rotational energies as

$$\epsilon^{\mathrm{int}} = \epsilon^{\mathrm{el}} + \epsilon^{\mathrm{vib}} + \epsilon^{\mathrm{rot}}. \tag{C.1}$$

A schematic representation of the electronic, vibrational, and rotational energy levels

is shown in Fig. C.1(a). Here, we observe that an electronic state of a generic molecule (purple curve) possess multiple vibrational energy levels (red horizontal lines), and among them, multiple rotational levels (green horizontal lines in the inset) show up with a much smaller difference of energy. Radiative vibrational transitions may occur by the absorption of photons in the NIR while, for rotational transitions, the required photon energies fall in the far IR and microwave regimes. Remarkably, in a vibrational transition, the molecule can also change its rotational energy level, giving rise to the roto-vibrational transition spectrum.

Here, we focus on the vibrational transitions of a generic molecule. The way a molecule vibrates is called a vibrational mode. For molecules containing N atoms, there are $3N-5$ vibrational modes for linear samples, whereas for nonlinear ones $3N-6$ degrees of freedom arise. We know that when a photon interacts with a molecule with the appropriate energy, it can be absorbed so that the molecule gets excited to a higher vibrational energy. This process is called infrared absorption, and the schematic representation of the transition between the two vibrational energy levels involved is depicted within a vertical blue arrow in Fig. C.1(a).

When we consider that after a certain relaxation time, the molecule decays back to a lower energy level emitting a second photon, then the process is called light scattering. Interestingly, this second photon does not need to be equally energetic as the initial photon. When the molecule returns to the original energy level from a virtual state, the emitted and absorbed photons present the same energy. We name this process as elastic or Rayleigh scattering, which strongly depends on the size of the target molecule and, as an example, it is the responsible of the blue color of the sky [172]. In Fig. C.1(b) we show the energy-level diagram of the process.

On the other hand, if the molecule decays back to a roto-vibrational energy level different to the one it originated from, the emitted and absorbed photons may have different energy. In this case, we talk about inelastic or Raman scattering [172] which is typically very weak (~ 1 of 10^7 photons). When the final roto-vibrational level of the molecule presents a higher energy than the initial level, this means that the emitted photon is shifted to a lower frequency (redshift); namely, it presents a Stokes Raman-shift [see blue arrows on the left in Fig. C.1(c)]. In the case of a final less energetic roto-vibrational energy level, the emitted photon is shifted to a higher frequency (blueshift) and presents anti-Stokes Raman-shift [see blue arrows

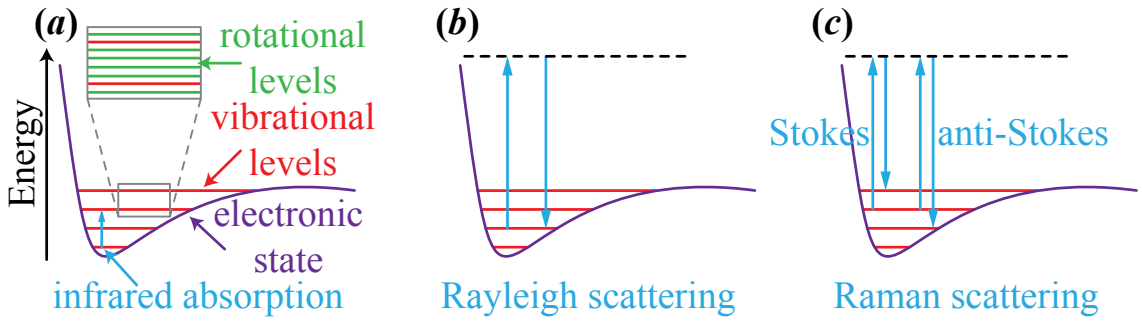

Figure C.1: Energy-level diagram of infrared absorption, Rayleigh scattering, and Raman scattering. (a) Sketch of the infrared absorption of a photon by a generic molecule that undergoes a transition (blue vertical arrow) from a lower energetic vibrational energy level to a higher one (red horizontal lines). The purple curve corresponds to the electronic energy of the molecule while the inset represents the rotational energies (green horizontal lines) lying between each vibrational energy level. (b) Elastic or Rayleigh scattering of a molecule. The molecule is excited up to a virtual state (black dashed line) and decays back to the same vibrational energy level emitting a photon with the same energy as the incident photon. (c) Inelastic or Raman scattering of a molecule. Here, the molecule decays back to a vibrational level with higher (lower) energy than the original level thus producing Stokes (anti-Stokes) Raman scattering.

on the right in Fig. C.1(c)]. Usually, in spectroscopy these shifts are expressed in cm^{-1} using the relation

$$\Delta\nu_{\mathrm{R}}(\mathrm{cm}^{-1}) = \hbar(\omega_{\mathrm{pump}} - \omega_1) \times \left(8065.544\,\mathrm{cm}^{-1}\,\mathrm{eV}^{-1}\right), \tag{C.2}$$

where $\hbar\omega_{\mathrm{pump}}$ is the incident or pump photon energy (in eV), and $\hbar\omega_1$ is the energy of the photon emitted by the molecule (also in eV). Thus, positive values of $\Delta\nu_{\mathrm{R}}$ correspond to Stokes shifts, and negative values to anti-Stokes ones.

List of publications and contributions to conferences

The research performed during the development of this thesis has led to the following publications and contributions to international conferences:

Articles on which the thesis is based

1. J. D. Cox, I. Silveiro, and F. J. García de Abajo.
   Quantum effects in the nonlinear response of graphene plasmons.
   (submitted, September 2015).

2. M. T. Manzoni, I. Silveiro, F. J. García de Abajo, and D. E. Chang.
   Second-order quantum nonlinear optical processes in single graphene nanostructures and arrays.
   New J. Phys., **17(8)**, 083031 (2015).

3. I. Silveiro, J. M. Plaza Ortega, and F. J. García de Abajo.
   Plasmon wave function of graphene nanoribbons.
   New J. Phys., **17(8)**, 083013 (2015).

4. A. Marini, I. Silveiro, and F. J. García de Abajo.
   Molecular sensing with tunable graphene plasmons.
   ACS Photonics, **2(7)**, 876–882 (2015).

5. I. Silveiro, J. M. Plaza Ortega, and F. J. García de Abajo.
   Quantum nonlocal effects in individual and interacting graphene nanoribbons.
   Light, Science and Applic., **4**, e241 (2015).

6. I. Silveiro and F. J. García de Abajo.
   Plasmons in inhomogeneously doped neutral and charged graphene nanodisks.
   Appl. Phys. Lett., **104**, 131103 (2014).

7. I. Silveiro, A. Manjavacas, S. Thongrattanasiri, and F. J. García de Abajo. Plasmonic energy transfer in periodically doped graphene. *New J. Phys.*, **15**, 033042 (2013).

8. S. Thongrattanasiri, I. Silveiro, and F. J. García de Abajo. Plasmons in electrostatically doped graphene. *Appl. Phys. Lett.*, **100**, 201105 (2012).

Contributions to international conferences

Oral contributions

1. Graphene Optics Workshop 2015–Optics of Graphene and 2D Materials. Exeter, UK.
   Second-order nonlinearities in single graphene nano-structures and arrays.
   M. T. Manzoni, I. Silveiro, F. J. García de Abajo, and D. E. Chang. September, 2015.

2. SPIE Optics and Photonics. San Diego, California, USA.
   Infrared spectroscopy with tunable graphene plasmons.
   A. Marini, I. Silveiro, and F. J. García de Abajo. August, 2015.

3. 7th International Conference on Surface Plasmon Photonics (SPP7). Jerusalem, Israel.
   Plasmon wave function of graphene nanoribbons.
   I. Silveiro, J. M. Plaza Ortega, and F. J. García de Abajo. June, 2015.

4. ImagineNano 2015. Bilbao, Spain.
   Quantum nonlocal effects in individual and interacting graphene nanoribbons.
   I. Silveiro, J. M. Plaza Ortega, and F. J. García de Abajo. March, 2015.

5. Nanometa 2015. Seefeld in Tirol, Austria.
   Quantum nonlocal effects in individual and interacting graphene nanoribbons.
   I. Silveiro, J. M. Plaza Ortega, and F. J. García de Abajo. January, 2015.

6. SPIE Optics and Photonics. San Diego, California, USA.
   Plasmons in inhomogeneously doped neutral and charged graphene nanodisks.
   I. Silveiro and F. J. García de Abajo. August, 2014.

7. SPIE Optics and Photonics. San Diego, California, USA.
   Quantum nonlocal effects in individual and interacting graphene nanoribbons.
   I. Silveiro, J. M. Plaza Ortega, and F. J. García de Abajo. August, 2014.

Poster contributions

1. 7th International Conference on Surface Plasmon Photonics (SPP7). Jerusalem, Israel.
   Quantum nonlocal effects in individual and interacting graphene nanoribbons.
   I. Silveiro, J. M. Plaza Ortega, and F. J. García de Abajo. June, 2015.

2. 7th International Conference on Surface Plasmon Photonics (SPP7). Jerusalem, Israel.
   Molecular Sensing with Tunable Graphene Plasmons.
   A. Marini, I. Silveiro, and F. J. García de Abajo. June, 2015.

3. ImagineNano 2015. Bilbao, Spain.
   Quantum nonlocal effects in individual and interacting graphene nanoribbons.
   I. Silveiro, J. M. Plaza Ortega, and F. J. García de Abajo. March, 2015.

4. Nanometa 2015. Seefeld in Tirol, Austria.
   Plasmons in inhomogeneously doped neutral and charged graphene nanodisks.
   I. Silveiro and F. J. García de Abajo. January, 2015.

5. Nanometa 2015. Seefeld in Tirol, Austria.
   Plasmon wave function of graphene nanoribbons.
   I. Silveiro, J. M. Plaza Ortega, and F. J. García de Abajo. January, 2015.

6. Nanolight Conference. Benasque, Huesca, Spain.
   Plasmons in inhomogeneously doped neutral and charged graphene nanodisks.
   I. Silveiro, J. M. Plaza Ortega, and F. J. García de Abajo. March, 2014.

7. Graphene Nanophotonics. Benasque, Huesca, Spain.
   Plasmonic energy transfer in periodically doped graphene.
   I. Silveiro, A. Manjavacas, S. Thongrattanasiri, and F. J. García de Abajo. March, 2013.

8. International Topical Meeting on Nanophotonics and Metamaterials. Seefeld in Tirol, Austria.
   Plasmonic energy transfer in periodically doped graphene.
   I. Silveiro, A. Manjavacas, S. Thongrattanasiri, and F. J. García de Abajo. January, 2013.

9. 12th International Conference on Near-Field Optics, Nanophotonics and Related Techniques (NFO12). San Sebastián, Spain.
   Plasmons in periodically doped graphene.
   I. Silveiro, A. Trügler, S. Thongrattanasiri, and F. J. García de Abajo. September, 2012.

Communications

1. Nanolight Conference. Benasque, Huesca, Spain. March, 2012.
2. XXI Curso de Introducción a la Investigación en Óptica. Instituto de Óptica Daza de Valdés (CSIC), Madrid, Spain. April, 2011.

Bibliography

[1] H. Petroski. *The pencil: a history of design and circumstance.* A. A. Knopf, New York, 1989.

[2] H. A. Taylor Jr. *Graphite, Natural.* John Wiley & Sons, Inc., 2000.

[3] H. W. Kroto, J. R. Heath, S. C. O'Brien, R. F. Curl, and R. E. Smalley. C_{60}: Buckminsterfullerene. *Nature*, 318:162–163, 1985.

[4] Z. Yoshida and E. Osawa. Aromaticity. *Chemical Monograph Series 22. Kyoto: Kagaku-dojin.*, pages 174–8, 1971.

[5] A. Chuvilin, U. Kaiser, E. Bichoutskaia, N. A. Besley, and A. N. Khlobystov. Direct transformation of graphene to fullerene. *Nature Chemistry*, 2:450–453, 2010.

[6] S. Iijima. Helical microtubules of graphitic carbon. *Nature*, 354:56–58, 1991.

[7] K. S. Novoselov, A. K. Geim, S. V. Morozov, D. Jiang, Y. Zhang, S. V. Dubonos, I. V. Grigorieva, and A. A. Firsov. Electric field effect in atomically thin carbon films. *Science*, 306:666–669, 2004.

[8] K. S. Novoselov, D. Jiang, F. Schedin, T. J. Booth, V. V. Khotkevich, S. V. Morozov, and A. K. Geim. Two-dimensional atomic crystals. *Proc. Natl. Academ. Sci.*, 102:10451–10453, 2005.

[9] Y. Zhang, Y. W. Tan, H. L. Stormer, and P. Kim. Experimental observation of the quantum Hall effect and Berry's phase in graphene. *Nature*, 438:201–204, 2005.

[10] K. S. Novoselov, A. K. Geim, S. V. Morozov, D. Jiang, M. I. Katsnelson, I. V. Grigorieva, S. V. Dubonos, and A. A. Firsov. Two-dimensional gas of massless Dirac fermions in graphene. *Nature*, 438:197–200, 2005.

[11] C. Berger, Z. Song, X. Li, X. Wu, N. Brown, C. Naud, D. Mayou, T. Li, J. Hass, A. N. Marchenkov, E. H. Conrad, P. N. First, and W. A. de Heer. Electronic confinement and coherence in patterned epitaxial graphene. *Science*, 312:1191–1196, 2006.

[12] P. R. Wallace. The band theory of graphite. *Phys. Rev.*, 71:622–634, 1947.

[13] S. Reich, J. Maultzsch, C. Thomsen, and P. Ordejón. Tight-binding description of graphene. *Phys. Rev. B*, 66:035412, 2002.

[14] S. Phark, J. Borme, A. L. Vanegas, M. Corbetta, D. Sander, and J. Kirschner. Direct observation of electron confinement in epitaxial graphene nanoislands. *ACS Nano*, 5:8162–8166, 2011.

[15] R. S. Deacon, K. C. Chuang, R. J. Nicholas, K. S. Novoselov, and A. K. Geim. Cyclotron resonance study of the electron and hole velocity in graphene monolayers. *Phys. Rev. B*, 76:081406(R), 2007.

[16] P. A. M. Dirac. The quantum theory of the electron. *Proceedings of the Royal Society of London A: Mathematical, Physical and Engineering Sciences*, 1928.

[17] A. Marini, S. Longhi, and F. Biancalana. Optical simulation of neutrino oscillations in binary waveguide arrays. *Phys. Rev. Lett.*, 113:150401, 2014.

[18] N. W. Ashcroft and N. D. Mermin. *Solid State Physics*. Harcourt College Publishers, New York, 1976.

[19] J. P. Hobson and W. A. Nierenberg. The statistics of a two-dimensional, hexagonal net. *Phys. Rev.*, 89:662–662, 1953.

[20] A. H. Castro Neto, F. Guinea, N. M. R. Peres, K. S. Novoselov, and A. K. Geim. The electronic properties of graphene. *Rev. Mod. Phys.*, 81:109–162, 2009.

[21] L. Van Hove. The occurrence of singularities in the elastic frequency distribution of a crystal. *Phys. Rev.*, 89:1189–1193, 1953.

[22] A. K. Geim and K. S. Novoselov. The rise of graphene. *Nat. Mater.*, 6:183–191, 2007.

[23] K. Zou, X. Hong, D. Keefer, and J. Zhu. Deposition of high-quality HfO_2 on graphene and the effect of remote oxide phonon scattering. *Phys. Rev. Lett.*, 105:126601, 2010.

[24] C. R. Dean, A. F. Young, I. Meric, C. Lee, L. Wang, S. Sorgenfrei, K. Watanabe, T. Taniguchi, P. Kim, K. L. Shepard, and J. Hone. Boron nitride substrates for high-quality graphene electronics. *Nat. Nanotech.*, 5:722–726, 2010.

[25] K. I. Bolotin, K. J. Sikes, Z. Jiang, M. Klima, G. Fudenberg, J. Hone, P. Kim, and H. L. Stormer. Ultrahigh electron mobility in suspended graphene. *Sol. State Commun.*, 146:351–355, 2008.

[26] L. Novotny and B. Hecht. *Principles of Nano-Optics*. Cambridge University Press, New York, 2006.

[27] F. J. García de Abajo and A. Howie. Retarded field calculation of electron energy loss in inhomogeneous dielectrics. *Phys. Rev. B*, 65:115418, 2002.

[28] S. A. Maier. *Plasmonics: Fundamentals and Applications*. Springer, New York, 2007.

[29] F. J. García de Abajo and A. Manjavacas. Plasmonics in atomically thin materials. *Faraday Discussions*, 178:87–107, 2015.

[30] F. J. García de Abajo. Graphene plasmonics: Challenges and opportunities. *ACS Photonics*, 1:135–152, 2014.

[31] F. H. L. Koppens, D. E. Chang, and F. J. García de Abajo. Graphene plasmonics: A platform for strong light-matter interactions. *Nano Lett.*, 11:3370–3377, 2011.

[32] D. Pines and P. Nozières. *The Theory of Quantum Liquids*. W. A. Benjamin, Inc., New York, 1966.

[33] L. Hedin and S. Lundqvist. Effects of electron-electron and electron-phonon interactions on the one-electron states of solids. Volume 23 of *Solid State Physics*, pages 1 – 181. Academic Press, 1970.

[34] B. Wunsch, T. Stauber, F. Sols, and F. Guinea. Dynamical polarization of graphene at finite doping. *New J. Phys.*, 8:318, 2006.

[35] E. H. Hwang and S. Das Sarma. Dielectric function, screening, and plasmons in two-dimensional graphene. *Phys. Rev. B*, 75:205418, 2007.

[36] M. Polini, R. Asgari, G. Borghi, Y. Barlas, T. Pereg-Barnea, and A. H. MacDonald. Plasmons and the spectral function of graphene. *Phys. Rev. B*, 77:081411(R), 2008.

[37] L. A. Falkovsky and A. A. Varlamov. Space-time dispersion of graphene conductivity. *Eur. Phys. J. B*, 56:281, 2007.

[38] M. Jablan, H. Buljan, and M. Soljačić. Plasmonics in graphene at infrared frequencies. *Phys. Rev. B*, 80:245435, 2009.

[39] P. B. Johnson and R. W. Christy. Optical constants of the noble metals. *Phys. Rev. B*, 6:4370–4379, 1972.

[40] S. Thongrattanasiri, A. Manjavacas, and F. J. García de Abajo. Quantum finite-size effects in graphene plasmons. *ACS Nano*, 6:1766–1775, 2012.

[41] J. Christensen, A. Manjavacas, S. Thongrattanasiri, F. H. L. Koppens, and F. J. García de Abajo. Graphene plasmon waveguiding and hybridization in individual and paired nanoribbons. *ACS Nano*, 6:431–440, 2012.

[42] G. Gensterblum, J. J. Pireaux, P. A. Thiry, R. Caudano, J. P. Vigneron, P. Lambin, A. A. Lucas, and W. Krätschmer. High-resolution electron-energy-loss spectroscopy of thin films of C_{60} on Si(100). *Phys. Rev. Lett.*, 67:2171–2174, 1991.

[43] Y. Saito, H. Shinohara, and A. Ohshita. Bulk plasmons in solid C_{60}. *Jpn. J. Appl. Phys.*, 30:1068–1070, 1991.

[44] R. Kuzuo, M. Terauchi, and M. Tanaka. Electron energy-loss spectra of carbon nanotubes. *Jpn. J. Appl. Phys.*, 31:1484–1487, 1992.

[45] O. Stéphan, D. Taverna, M. Kociak, K. Suenaga, L. Henrard, and C. Colliex. Dielectric response of isolated carbon nanotubes investigated by spatially resolved electron energy-loss spectroscopy: From multiwalled to single-walled nanotubes. *Phys. Rev. B*, 66:155422, 2002.

[46] M. K. Kinyanjui, C. Kramberger, T. Pichler, J. C. Meyer, P. Wachsmuth, G. Benner, and U. Kaiser. Direct probe of linearly dispersing 2d interband plasmons in a free-standing graphene monolayer. *Europhys. Lett.*, 97(5):57005, 2012.

[47] V. Myroshnychenko, J. Rodríguez-Fernández, I. Pastoriza-Santos, A. M. Funston, C. Novo, P. Mulvaney, L. M. Liz-Marzán, and F. J. García de Abajo. Modelling the optical response of gold nanoparticles. *Chem. Soc. Rev.*, 37:1792–1805, 2008.

[48] F. J. García de Abajo, A. Asenjo-García, and M. Kociak. Multiphoton absorption and emission by interaction of swift electrons with evanescent light fields. *Nano Lett.*, 10:1859–1863, 2010.

[49] V. Myroshnychenko, J. Nelayah, G. Adamo, N. Geuquet, J. Rodríguez-Fernández, I. Pastoriza-Santos, K. F. MacDonald, L. Henrard, L. M. Liz-Marzán, N. I. Zheludev, M. Kociak, and F. J. García de Abajo. Plasmon spectroscopy and imaging of individual gold nanodecahedra: A combined optical microscopy, cathodoluminescence, and electron energy-loss spectroscopy study. *Nano Lett.*, 12:4172–4180, 2012.

[50] A. Asenjo-García and F. J. García de Abajo. Dichroism in the interaction between vortex electron beams, plasmons, and molecules. *Phys. Rev. Lett.*, 113:066102, 2014.

[51] A. Losquin, L. F. Zagonel, V. Myroshnychenko, B. Rodríguez-González, M. Tencé, L. Scarabelli, J. Förstner, L. M. Liz-Marzán, F. J. García de Abajo, O. Stéphan, and M. Kociak. Unveiling nanometer scale extinction and scattering phenomena through combined electron energy loss spectroscopy and cathodoluminescence measurements. *Nano Lett.*, 15:1229–1237, 2015.

[52] F. J. García de Abajo. Optical excitations in electron microscopy. *Rev. Mod. Phys.*, 82:209–275, 2010.

[53] F. J. García de Abajo. Multiple excitation of confined graphene plasmons by single free electrons. *ACS Nano*, 7:11409–11419, 2013.

[54] J. R. M. Saavedra and F. Javier García de Abajo. Phonon excitation by electron beams in nanographenes. *Phys. Rev. B*, (92):115449, 2015.

[55] C. Tegenkamp, H. Pfnür, T. Langer, J. Baringhaus, and H. W. Schumacher. Plasmon electron–hole resonance in epitaxial graphene. *J. Phys.: Condens. Matter*, 23:012001, 2011.

[56] R. R. Nair, P. Blake, A. N. Grigorenko, K. S. Novoselov, T. J. Booth, T. Stauber, N. M. R. Peres, and A. K. Geim. Fine structure constant defines visual transparency of graphene. *Science*, 320:1308, 2008.

[57] K. F. Mak, M. Y. Sfeir, Y. Wu, C. H. Lui, J. A. Misewich, and T. F. Heinz. Measurement of the optical conductivity of graphene. *Phys. Rev. Lett.*, 101:196405, 2008.

[58] D. K. Efetov and P. Kim. Controlling electron-phonon interactions in graphene at ultrahigh carrier densities. *Phys. Rev. Lett.*, 105:256805, 2010.

[59] C. F. Chen, C. H. Park, B. W. Boudouris, J. Horng, B. Geng, C. Girit, A. Zettl, M. F. Crommie, R. A. Segalman, S. G. Louie, and F. Wang. Controlling inelastic light scattering quantum pathways in graphene. *Nature*, 471:617–620, 2011.

[60] H. Liu, Y. Liu, and D. Zhua. Chemical doping of graphene. *J. Mater. Chem.*, 21:3335–3345, 2011.

[61] I. Khrapach, F. Withers, T. H. Bointon, D. K. Polyushkin, W. L. Barnes, S. Russo, M. F. Craciun, and F. Monica. Novel highly conductive and transparent graphene-based conductors. *Adv. Mater.*, 24:2844–2849, 2012.

[62] L. D. Landau, E. M. Lifshitz, and L. P. Pitaevskii. *Electrodynamics of Continuous Media*. Pergamon Press, Oxford, 1984.

[63] A. Vakil and N. Engheta. Transformation optics using graphene. *Science*, 332:1291–1294, 2011.

[64] L. Ju, B. Geng, J. Horng, C. Girit, M. Martin, Z. Hao, H. A. Bechtel, X. Liang, A. Zettl, Y. R. Shen, and F. Wang. Graphene plasmonics for tunable terahertz metamaterials. *Nat. Nanotech.*, 6:630–634, 2011.

[65] Z. Fei, G. O. Andreev, W. Bao, L. M. Zhang, A. S. McLeod, C. Wang, M. K. Stewart, Z. Zhao, G. Dominguez, M. Thiemens, M. M. Fogler, M. J. Tauber, A. H. Castro-Neto, C. N. Lau, F. Keilmann, and D. N. Basov. Infrared nanoscopy of dirac plasmons at the graphene–SiO_2 interface. *Nano Lett.*, 11:4701–4705, 2011.

[66] J. Chen, M. Badioli, P. Alonso-González, S. Thongrattanasiri, F. Huth, J. Osmond, M. Spasenović, A. Centeno, A. Pesquera, P. Godignon, A. Zurutuza Elorza, N. Camara, F. J. García de Abajo, R. Hillenbrand, and F. H. L. Koppens. Optical nano-imaging of gate-tunable graphene plasmons. *Nature*, 487:77–81, 2012.

[67] Z. Fei, A. S. Rodin, G. O. Andreev, W. Bao, A. S. McLeod, M. Wagner, L. M. Zhang, Z. Zhao, M. Thiemens, G. Dominguez, M. M. Fogler, A. H. Castro Neto, C. N. Lau, F. Keilmann, and D. N. Basov. Gate-tuning of graphene plasmons revealed by infrared nano-imaging. *Nature*, 487:82–85, 2012.

[68] H. Yan, X. Li, B. Chandra, G. Tulevski, Y. Wu, M. Freitag, W. Zhu, P. Avouris, and F. Xia. Tunable infrared plasmonic devices using graphene/insulator stacks. *Nat. Nanotech.*, 7:330–334, 2012.

[69] V. W. Brar, M. S. Jang, M. Sherrott, J. J. Lopez, and H. A. Atwater. Highly confined tunable mid-infrared plasmonics in graphene nanoresonators. *Nano Lett.*, 13:2541–2547, 2013.

[70] H. Yan, T. Low, W. Zhu, Y. Wu, M. Freitag, X. Li, F. Guinea, P. Avouris, and F. Xia. Damping pathways of mid-infrared plasmons in graphene nanostructures. *Nat. Photon.*, 7:394–399, 2013.

[71] Z. Fang, S. Thongrattanasiri, A. Schlather, Z. Liu, L. Ma, Y. Wang, P. M. Ajayan, P. Nordlander, N. J. Halas, and F. J. García de Abajo. Gated tunability and hybridization of localized plasmons in nanostructured graphene. *ACS Nano*, 7:2388–2395, 2013.

[72] A. S. Rodin, Z. Fei, A. S. McLeod, M. Wagner, A. H. Castro Neto, M. M. Fogler, and D. N. Basov. Plasmonic hot spots in triangular tapered graphene microcrystals, arXiv:1309.1909, 2013.

[73] M. S. Jang, V. W. Brar, M. C. Sherrott, J. J. Lopez, L. Kim, S. Kim, M. Choi, and H. A. Atwater. Tunable large resonant absorption in a mid-infrared graphene salisbury screen. *Phys. Rev. B*, 90:165409, 2014.

[74] A. Principi, M. Carrega, M. B. Lundeberg, A. Woessner, F. H. L. Koppens, G. Vignale, and M. Polini. Plasmon losses due to electron-phonon scattering: The case of graphene encapsulated in hexagonal boron nitride. *Phys. Rev. B*, 90:165408, 2014.

[75] S. A. Mikhailov. Non-linear electromagnetic response of graphene. *Europhys. Lett.*, 79:27002, 2007.

[76] S. A. Mikhailov. Electromagnetic response of electrons in graphene: Non-linear effects. *Physica E*, 40(7):2626–2629, 2008.

[77] E. Hendry, P. J. Hale, J. Moger, A. K. Savchenko, and S. A. Mikhailov. Coherent nonlinear optical response of graphene. *Phys. Rev. Lett.*, 105:097401, 2010.

[78] S. A. Mikhailov. Theory of the giant plasmon-enhanced second-harmonic generation in graphene and semiconductor two-dimensional electron systems. *Phys. Rev. B*, 84:045432, 2011.

[79] A. V. Gorbach, A. Marini, and D. V. Skryabin. Graphene-clad tapered fiber: effective nonlinearity and propagation losses. *Opt. Lett.*, 38(24):5244–5247, 2013.

[80] J. D. Cox and F. J. García de Abajo. Electrically tunable nonlinear plasmonics in graphene nanoislands. *Nat. Commun.*, 5:5725, 2014.

[81] M. T. Manzoni, I. Silveiro, F. J. García de Abajo, and D. E. Chang. Second-order quantum nonlinear optical processes in single graphene nanostructures and arrays. *New J. Phys.*, 17(8):083031, 2015.

[82] S. Y. Shin, N. D. Kim, J. G. Kim, K. S. Kim, D. Y. Noh, K. S. Kim, and J. W. Chung. Control of the π plasmon in a single layer graphene by charge doping. *Appl. Phys. Lett.*, 99:082110, 2011.

[83] H. Yan, Z. Li, X. Li, W. Zhu, P. Avouris, and F. Xia. Infrared spectroscopy of tunable dirac terahertz magneto-plasmons in graphene. *Nano Lett.*, 12:3766–3771, 2012.

[84] L. Brey and H. A. Fertig. Elementary electronic excitations in graphene nanoribbons. *Phys. Rev. B*, 75:125434, 2007.

[85] A. Y. Nikitin, F. Guinea, F. J. García-Vidal, and L. Martín-Moreno. Edge and waveguide terahertz surface plasmon modes in graphene microribbons. *Phys. Rev. B*, 84:161407(R), 2011.

[86] S. Thongrattanasiri, I. Silveiro, and F. J. García de Abajo. Plasmons in electrostatically doped graphene. *Appl. Phys. Lett.*, 100:201105, 2012.

[87] W. Wang and J. M. Kinaret. Plasmons in graphene nanoribbons: Interband transitions and nonlocal effects. *Phys. Rev. B*, 87:195424, 2013.

[88] S. Thongrattanasiri, F. H. L. Koppens, and F. J. García de Abajo. Complete optical absorption in periodically patterned graphene. *Phys. Rev. Lett.*, 108:047401, 2012.

[89] A. Manjavacas, S. Thongrattanasiri, and F. J. García de Abajo. Plasmons driven by single electrons in graphene nanoislands. *Nanophotonics*, 2:139–151, 2013.

[90] I. Silveiro and F. J. García de Abajo. Plasmons in inhomogeneously doped neutral and charged graphene nanodisks. *Appl. Phys. Lett.*, 104:131103, 2014.

[91] R. Yu, V. Pruneri, and F. J. García de Abajo. Resonant visible light modulation with graphene. *ACS Photonics*, 2:550–558, 2015.

[92] J. Shen, Y. Zhu, X. Yang, and C. Li. Graphene quantum dots: emergent nanolights for bioimaging, sensors, catalysis and photovoltaic devices. *Chem. Commun.*, 48:3686–3699, 2012.

[93] A. Marini, I. Silveiro, and F. J. García de Abajo. Molecular sensing with tunable graphene plasmons. *ACS Photonics*, 2(7):876–882, 2015.

[94] S. A. Mikhailov and K. Ziegler. New electromagnetic mode in graphene. *Phys. Rev. Lett.*, 99:016803, 2007.

[95] J. J. Sakurai and J. Napolitano. *Modern Quantum Mechanics (2nd Edition).* Addison-Wesley, 2010.

[96] J. Sabio, J. Nilsson, and A. H. Castro Neto. f-sum rule and unconventional spectral weight transfer in graphene. *Phys. Rev. B*, 78:075410, 2008.

[97] U. Hohenester and A. Trügler. MNPBEM - A Matlab toolbox for the simulation of plasmonic nanoparticles. *Comput. Phys. Commun.*, 183:370, 2012.

[98] L. A. Blanco and F. J. García de Abajo. Spontaneous light emission in complex nanostructures. *Phys. Rev. B*, 69:205414, 2004.

[99] S. Thongrattanasiri and F. J. García de Abajo. Optical field enhancement by strong plasmon interaction in graphene nanostructures. *Phys. Rev. Lett.*, 110:187401, 2013.

[100] A. Principi, G. Vignale, M. Carrega, and M. Polini. Impact of disorder on dirac plasmon losses. *Phys. Rev. B*, 88:121405(R), 2013.

[101] I. Silveiro, J. M. Plaza Ortega, and F. J. García de Abajo. Quantum nonlocal effects in individual and interacting graphene nanoribbons. *Light, Science and Applic.*, 4, 2015.

[102] K. J. Tielrooij, S. A. Jensen J. C. W. Song and, A. Centeno, A. Pesquera, A. Zurutuza Elorza, M. Bonn, L. S. Levitov, and F. H. L. Koppens. Photoexcitation cascade and multiple hot-carrier generation in graphene. *Nat. Phys.*, 9:248–252, 2013.

[103] I. Silveiro, A. Manjavacas, S. Thongrattanasiri, and F. J. García de Abajo. Plasmonic energy transfer in periodically doped graphene. *New J. Phys.*, 15:033042, 2013.

[104] F. J. García de Abajo. Colloquium: Light scattering by particle and hole arrays. *Rev. Mod. Phys.*, 79:1267–1290, 2007.

[105] H. C. van de Hulst. *Light Scattering by Small Particles*. Dover, New York, 1981.

[106] J. Wu, W. Pisula, and K. Müllen. Graphenes as potential material for electronics. *Chem. Rev.*, 107:718–747, 2007.

[107] X. Li, X. Wang, L. Zhang, S. Lee, and H. Dai. Chemically derived, ultrasmooth graphene nanoribbon semiconductors. *Science*, 319:1229–1232, 2008.

[108] J. Cai, P. Ruffieux, R. Jaafar, M. Bieri, T. Braun, S. Blankenburg, M. Muoth, A. P. Seitsonen, M. Saleh, X. Feng, K. Müllen, and R. Fasel. Atomically precise bottom-up fabrication of graphene nanoribbons. *Nature*, 466:470–473, 2010.

[109] B. Li, K. Tahara, J. Adisoejoso, W. Vanderlinden, K. S. Mali, S. De Gendt, Y. Tobe, and S. De Feyter. Self-assembled air-stable supramolecular porous networks on graphene. *ACS Nano*, 7(12):10764–10772, 2013.

[110] I. Silveiro, J. M. Plaza Ortega, and F. J. García de Abajo. Plasmon wave function of graphene nanoribbons. *New J. Phys.*, 17(8):083013, 2015.

[111] J. D. Jackson. *Classical Electrodynamics*. Wiley, New York, 1999.

[112] E. Hecht. *Optics (4th Edition)*. Addison-Wesley, San Francisco, 2002.

[113] R. L. Fante and M. T. McCormack. Reflection properties of the salisbury screen. *IEEE Trans. Antennas Propag.*, 36:1443–1454, 1988.

[114] N. Engheta. Thin absorbing screens using metamaterial surfaces. In *Proc. IEEE International Symposium on Antennas and Propagation*, volume 2, pages 392–395. IEEE, 2002.

[115] H. A. Wheeler. Transmission-line properties of parallel wide strips by a conformal-mapping approximation. *IEEE Trans. Microwave Theory Tech.*, 12:280–289, 1964.

[116] H. A. Wheeler. Transmission-line properties of a strip on a dielectric sheet on a plane. *IEEE Trans. Microwave Theory Tech.*, 25:631–647, 1977.

[117] P. G. Silvestrov and K. B. Efetov. Charge accumulation at the boundaries of a graphene strip induced by a gate voltage: Electrostatic approach. *Phys. Rev. B*, 77:155436, 2008.

[118] F. T. Vasko and I. V. Zozoulenko. Conductivity of a graphene strip: Width and gate-voltage dependencies. *Appl. Phys. Lett.*, 97:092115, 2010.

[119] E. G. Mishchenko, A. V. Shytov, and P. G. Silvestrov. Guided plasmons in graphene *p-n* junctions. *Phys. Rev. Lett.*, 104:156806, 2010.

[120] I. S. Gradshteyn and I. M. Ryzhik. *Table of Integrals, Series, and Products*. Academic Press, London, 1980.

[121] B. U. Felderhof. Derivation of the Love equation for the charge density of a circular plate condenser, arXiv:1309.3662v1, 2013.

[122] A. Otto. Excitation of nonradiative surface plasma waves in silver by the method of frustrated total reflection. *Z. Physik*, 216(4):398–410, 1968.

[123] E. Kretschmann and H. Raether. Radiative decay of non-radiative surface plasmons excited by light. *Z. Naturforsch. A*, 23:2135–2136, 1968.

[124] W. Zhou, J. Lee, J. Nanda, S. T. Pantelides, S. J. Pennycook, and J. C. Idrobo. Atomically localized plasmon enhancement in monolayer graphene. *Nat. Nanotech.*, 7:161–165, 2012.

[125] Y. V. Bludov, M. I. Vasilevskiy, and N. M. R. Peres. Mechanism for graphene-based optoelectronic switches by tuning surface plasmon-polaritons in monolayer graphene. *Europhys. Lett.*, 92(6):68001, 2010.

[126] N. M. R. Peres, A. Ferreira, Y. V. Bludov, and M. I. Vasilevskiy. Light scattering by a medium with a spatially modulated optical conductivity: The case of graphene. *J. Phys.: Condens. Matter*, 24:245303, 2012.

[127] A. Nikitin, F. Guinea, F. J. García-Vidal, and L. Martín-Moreno. Surface plasmon enhanced absorption and suppressed transmission in periodic arrays of graphene ribbons. *Phys. Rev. B*, 85:081405, 2012.

[128] A. Ferreira and N. M. R. Peres. Complete light absorption in graphene-metamaterial corrugated structures. *Phys. Rev. B*, 86:205401, 2012.

[129] Y. V. Bludov, N. M. R. Peres, and M. I. Vasilevskiy. Graphene-based polaritonic crystal. *Phys. Rev. B*, 85:245409, 2012.

[130] X. M. Bendaña, F. J. García de Abajo, and A. Polman. Confined collective excitations of self-standing and supported planar periodic particle arrays. *Opt. Express*, 17:18826–18835, 2009.

[131] E. M. Purcell. Spontaneous emission probabilities at radio frequencies. *Phys. Rev.*, 69:681, 1946.

[132] M. Frimmer, Y. Chen, and A. F. Koenderink. Scanning emitter lifetime imaging microscopy for spontaneous emission control. *Phys. Rev. Lett.*, 107:123602, 2011.

[133] D. P. Fussell, R. C. McPhedran, and C. Martijn de Sterke. Three-dimensional Green's tensor, local density of states, and spontaneous emission in finite two-dimensional photonic crystals composed of cylinders. *Phys. Rev. E*, 70:066608, 2004.

[134] F. J. García de Abajo and M. Kociak. Probing the photonic local density of states with electron energy loss spectroscopy. *Phys. Rev. Lett.*, 100:106804, 2008.

[135] D. L. Andrews. *Photonics, Nanophotonic Structures and Materials.* Wiley-Science Wise Co-Publication (Volume 2), New York, 2015.

[136] C. David and F. J. García de Abajo. Surface plasmon dependence on the electron density profile at metal surfaces. *ACS Nano*, 8:9558–9566, 2014.

[137] R. W. Boyd. *Nonlinear Optics.* Academic Press, New York, 2nd edition, 2003.

[138] J. J. Dean and H. M. van Driel. Graphene and few-layer graphite probed by second-harmonic generation: Theory and experiment. *Phys. Rev. B*, 82:125411, 2010.

[139] R. Wu, Y. Zhang, S. Yan, F. Bian, W. Wang, X. Bai, X. Lu, J. Zhao, and E. Wang. Purely coherent nonlinear optical response in solution dispersions of graphene sheets. *Nano Lett.*, 11:5159–5164, 2011.

[140] H. Zhang, S. Virally, Q. Bao, L. K. Ping, S. Massar, N. Godbout, and P. Kockaert. Z-scan measurement of the nonlinear refractive index of graphene. *Opt. Lett.*, 37:1856–1858, 2012.

[141] T. Gu, N. Petrone, J. F. McMillan, A. van der Zande, M. Yu, G. Q. Lo, D. L. Kwong, J. Hone, and C. W. Wong. Regenerative oscillation and four-wave mixing in graphene optoelectronics. *Nat. Photon.*, 6:554–559, 2012.

[142] N. Kumar, J. Kumar, C. Gerstenkorn, R. Wang, H.-Y. Chiu, A. L. Smirl, and H. Zhao. Third harmonic generation in graphene and few-layer graphite films. *Phys. Rev. B*, 87:121406(R), 2013.

[143] S.-Y. Hong, J. I. Dadap, N. Petrone, P.-C. Yeh, J. Hone, and R. M. Osgood, Jr. Optical third-harmonic generation in graphene. *Phys. Rev. X*, 3:021014, 2013.

[144] N. M. R. Peres, Y. V. Bludov, J. E. Santos, A.-P. Jauho, and M. I. Vasilevskiy. Optical bistability of graphene in the terahertz range. *Phys. Rev. B*, 90:125425, 2014.

[145] J. L. Cheng, N. Vermeulen, and J. E. Sipe. Third order optical nonlinearity of graphene. *New J. Phys.*, 16:053104, 2014.

[146] S. A. Mikhailov. Quantum theory of the third-order nonlinear electrodynamic effects of graphene, arXiv:1506.00534, 2015.

[147] M. Gullans, D. E. Chang, F. H. L. Koppens, F. J. García de Abajo, and M. D. Lukin. Single-photon nonlinear optics with graphene plasmons. *Phys. Rev. Lett.*, 111:247401, 2013.

[148] A. V. Gorbach. Nonlinear graphene plasmonics: Amplitude equation for surface plasmons. *Phys. Rev. A*, 87:013830, 2013.

[149] X. Yao, M. Tokman, and A. Belyanin. Efficient nonlinear generation of THz plasmons in graphene and topological insulators. *Phys. Rev. Lett.*, 112:055501, 2014.

[150] D. A. Smirnova, R. E. Noskov, L. A. Smirnov, and Y. S. Kivshar. Dissipative plasmon solitons in graphene nanodisk arrays. *Phys. Rev. B*, 91:075409, 2015.

[151] M. Jablan and D. E. Chang. Multiplasmon absorption in graphene. *Phys. Rev. Lett.*, 114:236801, 2015.

[152] S. A. Mikhailov and K. Ziegler. Nonlinear electromagnetic response of graphene: frequency multiplication and the self-consistent-field effects. *J. Phys.: Condens. Matter*, 20:384204, 2008.

[153] J. D. Cox, I. Silveiro, and F. J. García de Abajo. Quantum effects in the nonlinear response of the graphene plasmons. Submitted, September 2015.

[154] J. Kerr. On rotation of the plane of polarization by reflection from the pole of a magnet. *Phil. Mag. Series 5*, 3(19):321–343, 1877.

[155] K. Ataka, S. T. Stripp, and J. Heberle. Surface-enhanced infrared absorption spectroscopy (SEIRAS) to probe monolayers of membrane proteins. *Biochimica et Biophysica Acta (BBA) - Biomembranes*, 1828(10):2283–2293, 2013.

[156] M. Moskovits. Surface-enhanced spectroscopy. *Rev. Mod. Phys.*, 57:783–826, 1985.

[157] M. Moskovits. Surface-enhanced Raman spectroscopy: a brief retrospective. *J. Raman Spectrosc.*, 36:485–496, 2005.

[158] K. Kneipp, Y. Wang, H. Kneipp, L. T. Perelman, I. Itzkan, R. R. Dasari, and M. S. Feld. Single molecule detection using surface-enhanced Raman scattering (SERS). *Phys. Rev. Lett.*, 78:1667–1670, 1997.

[159] S. Nie and S. R. Emory. Probing single molecules and single nanoparticles by surface-enhanced raman scattering. *Science*, 275:1102–1106, 1997.

[160] L. Rodríguez-Lorenzo, R. A. Álvarez-Puebla, I. Pastoriza-Santos, S. Mazzucco, O. Stéphan, M. Kociak, L. M. Liz-Marzán, and F. J. García de Abajo. Zeptomol detection through controlled ultrasensitive surface-enhanced Raman scattering. *J. Am. Chem. Soc.*, 131:4616–4618, 2009.

[161] Z. Fang, Y. Wang, A. Schlather, Z. Liu, P. M. Ajayan, F. J. García de Abajo, P. Nordlander, X. Zhu, and N. J. Halas. Active tunable absorption enhancement with graphene nanodisk arrays. *Nano Lett.*, 14:299–304, 2014.

[162] Y. Francescato, V. Giannini, J. Yang, M. Huang, and S. A. Maier. Graphene sandwiches as a platform for broadband molecular spectroscopy. *ACS Photonics*, 1:437–443, 2014.

[163] A. Hartstein, J. R. Kirtley, and J. C. Tsang. Enhancement of the infrared absorption from molecular monolayers with thin metal overlayers. *Phys. Rev. Lett.*, 45:201–204, 1980.

[164] A. Hatta, T. Ohshima, and W. Suëtaka. Observation of the enhanced infrared absorption of p-nitrobenzoate on Ag island films with an ATR technique. *Appl. Phys. A-Mater. Sci. Process.*, 29(2):71–75, 1982.

[165] A. Hatta, Y. Suzuki, and W. Suëtaka. Infrared absorption enhancement of monolayer species on thin evaporated Ag films by use of a Kretschmann configuration: Evidence for two types of enhanced surface electric fields. *Appl. Phys. A-Mater. Sci. Process.*, 35(3):135–140, 1984.

[166] http://depts.washington.edu/naivpl/content/spectral-databases-and-tools.

[167] M. Fleischmann, P. J. Hendra, and A. J. McQuillan. Raman spectra of pyridine adsorbed at a silver electrode. *Chem. Phys. Lett.*, 26(2):163–166, 1974.

[168] C. V. Raman and K. S. Krishnan. A new type of secondary radiation. *Nature*, 121:501–502, 1928.

[169] D. P. Mason, D. K. Gramotnev, and K. S. Kim. Plasmon nanofocusing in a dielectric hemisphere covered in tapered metal film. *Opt. Express*, 20:12866–12876, 2012.

[170] R. M. Eisberg and R. Resnick. *Quantum physics of atoms, molecules, solids, nuclei, and particles (2nd ed.)*. Wiley, New York, 1985.

[171] M. Born and R. Oppenheimer. Zur Quantentheorie der Molekeln. *Ann. Phys.*, 389:457–484, 1927.

[172] C. F. Bohren and D. R. Huffman. *Absorption and Scattering of Light by Small Particles*. Wiley-Interscience, New York, 1983.